Modeling and Measurements of the Bidirectional Reflectance of Microrough Silicon Surfaces

A Thesis
Presented to
The Academic Faculty

By

Qunzhi Zhu

In Partial Fulfillment
Of the Requirements for the Degree
Doctor of Philosophy in the
School of Mechanical Engineering

Georgia Institute of Technology
July 2004

Modeling and Measurements of the Bidirectional Reflectance
of Microrough Silicon Surfaces

Approved by:

Dr. Zhuomin Zhang, Advisor

Dr. J. Robert Mahan

Dr. Andrei G. Fedorov

Dr. Dennis W. Hess

Dr. Andrew F. Peterson

Date Approved July 9, 2004

ACKNOWLEDGEMENT

First, I would like to take this opportunity to thank my advisor, Dr. Zhuomin Zhang, for his guidance, support, and encouragement during this project. I appreciate his help in overcoming the culture difference and his advice on achieving a successful career. I also thank Professor J. Robert Mahan, Professor Andrei G. Fedorov, Professor Dennis W. Hess, and Professor Andrew F. Peterson for serving on my thesis reading committee and providing helpful suggestions and support on this project.

I gratefully acknowledge the help provided by Dr. Zhang's research group. I thank Dr. Yu-Jiun Shen for the hands-on experiences in the instrumentation, Drs. Donghai Chen and Yihui Zhou for helpful advice. I appreciate Ceji Fu for valuable discussion and sincere friendship. I enjoyed the collaborations with Yu-Bin Chen and Hyunjin Lee. I also thank Keunhan Park, Bong Jae Lee, Vinh Khuu, and Dan McCormick for reviewing my papers and helping me improve my English.

I thank Mr. Eric Lambers of Department of Material Science and Engineering at University of Florida and Mr. Joel Pikarsky of MIRC at Georgia Institute of Technology for showing me the wonderful world of the atomic force microscopy and Mr. Al Ogden of Department of Electrical and Computer Engineering at University of Florida for preparing coatings on some wafers.

Finally, I am indebted to my family, especially my parents, who have supported and encouraged me through all these years. I also thank my brother and my sister for their support.

This work has been supported by the National Science Foundation.

TABLE OF CONTENTS

LIST OF TABLES

LIST OF FIGURES

LIST OF SYMBOLS

C_I	=	instrument constant
D	=	distance from beam center to detector
d	=	sampling interval, or local thickness of film
E	=	y-component of electric field, or spectral emissive power
F	=	normal derivative of electric field
f	=	surface roughness wavelength
f_r	=	bidirectional reflectance distribution function
G	=	Green function, or geometrical attenuation factor
g	=	optical roughness
H	=	y-component of magnetic field
h	=	thickness of film
i	=	$\sqrt{-1}$
$\mathbf{k}$	=	wave vector
k	=	wave number
L	=	radiance, or normal derivative of H
l	=	length of a truncated surface
M	=	number of rows in an array
N	=	number of columns in an array, or number of surface nodes
n	=	refractive index, or normal vector, or index of surface nodes
p	=	probability density function
R_a	=	arithmetic average roughness

r = Fresnel reflection coefficient

S = shadowing function

U = uncertainty

V = output of a detector

Greek symbols

α = inclination angle of a microfacet, or position of a rotary stage

β = phase shift, or position of a rotary stage

δ = infinitesimal number, or Kronecker delta function

ε = relative permittivity

ϕ = azimuthal angle

γ = position of a rotary stage

η = criterion for validity

κ = extinction coefficient

λ = wavelength in vacuum, or refers to spectral value

θ = polar angle, or reflection angle, or observation angle

θ_{hc} = half-cone angle

ρ = reflectivity

Σ = interface

σ = root-mean-square roughness

τ = autocorrelation length

ω = solid angle

ξ	=	profile of interface, $\xi(x)$
ψ	=	local incidence angle
ζ	=	slope in x- or y-directions

Subscript

d-h	=	directional-hemispherical
f	=	film
h	=	refers to hemispherical criterion
i	=	incidence
m, *n*	=	indexes of an array, or indexes of surface nodes
obs	=	observation
r	=	reflection
s	=	substrate, or refers to specular criterion

SUMMARY

Bidirectional reflectance is a fundamental radiative property of rough surfaces. Knowledge of the bidirectional reflectance is crucial to the emissivity modeling and heat transfer analysis. This thesis concentrates on the modeling and measurements of the bidirectional reflectance for microrough silicon surfaces and on the validity of a hybrid method in the modeling of the bidirectional reflectance for thin-film coated rough surfaces.

The surface topography and the bidirectional reflectance distribution function (BRDF) of the rough side of several silicon wafers have been extensively characterized using an atomic force microscope and a laser scatterometer, respectively. The slope distribution calculated from the surface topographic data deviates from the Gaussian distribution. Both nearly isotropic and strongly anisotropic features are observed in the two-dimensional (2-D) slope distributions and in the measured BRDF for more than one sample. The 2-D slope distribution is used in a geometric-optics based model to predict the BRDF, which agrees reasonably well with the measured values. The side peaks in the slope distribution and the subsidiary peaks in the BRDF for two anisotropic samples are attributed to the formation of {311} planes during chemical etching. The correlation between the 2-D slope distribution and the BRDF has been developed.

A boundary integral method is applied to simulate the bidirectional reflectance of thin-film coatings on rough substrates. The roughness of the substrate is one dimensional for simplification. The result is compared to that from a hybrid method which uses the geometric optics approximation to model the roughness effect and the thin-film optics to

consider the interference due to the coating. The effects of the film thickness and the substrate roughness on the validity of the hybrid method have been investigated. The validity regime of the hybrid method is established for silicon dioxide films on silicon substrates in the visible wavelength range.

The proposed method to characterize the microfacet orientation and to predict the BRDF may be applied to other anisotropic or non-Gaussian rough surfaces. The measured BRDF may be used to model the apparent emissivity of silicon wafers to improve the temperature measurement accuracy in semiconductor manufacturing processes. The developed validity regime for the hybrid method can be beneficial to future research related to the modeling for thin-film coated rough surfaces.

CHAPTER 1

INTRODUCTION

The bidirectional reflectance distribution function (BRDF) is a fundamental property of rough surfaces, and knowledge of the BRDF is crucial to the emissivity modeling and heat transfer analysis (Siegel and Howell, 2002). The study of the BRDF is also important to optical engineering (Bennett and Mattsson, 1999) and object rendering (He et al., 1991). The BRDF of a surface can be predicted by solving the Maxwell equations if the surface roughness is fully characterized. Since the rigorous electromagnetic-wave solution generally requires a huge memory and a high-speed CPU, this approach is practically applicable to one-dimensional (1-D) rough surfaces only, though in some cases, solutions for two-dimensional (2-D) rough surfaces have been obtained (Saillard and Sentenac, 2001). Thus, it is common to use approximation methods, such as the Rayleigh-Rice perturbation theory, the Kirchhoff approximation, and the geometric optics approximation (Beckmann and Spizzichino, 1987; Tang et al., 1997). These approximations are only applicable within certain ranges of roughness and wavelength.

The Rayleigh-Rice perturbation theory can be used for relatively smooth surfaces. The Kirchhoff approximation is applicable when the surface profile is slightly undulating (i.e., without sharp crests and deep valleys). The geometric optics approximation is appropriate to surfaces whose root-mean-square (rms) roughness and autocorrelation length are greater than the wavelength of the incident radiation. Recent research has found that the geometric optics approximation can also be used for rough surfaces whose

rms roughness and autocorrelation length are comparable to the incidence wavelength (Tang et al., 1997). The geometric optics approximation can be easily incorporated into a statistical and Monte-Carlo method (Tang and Buckius, 2001; Zhou and Zhang, 2003). There exists good agreement between the simulation results employing the geometric optics approximation and the rigorous electromagnetic-wave solution (Tang and Buckius, 1998). However, the simulation based on the geometric optics approximation requires much less computational resources and takes much less time than that based on the rigorous solution (Tang and Buckius, 1998).

Since the BRDF is intrinsically dependent on the surface statistics, several analytical expressions are available to approximately correlate the surface statistics to the BRDF (Torrance and Sparrow, 1967; Bennett and Mattsson, 1999; Caron et al., 2003). The slope distribution function is a key input in the analytical models based on the geometric optics approximation. Before the invention of the atomic force microscope (AFM), the surface profile was usually measured with a mechanical profiler that scans the surface line-by-line. Therefore, the estimated 1-D slope distribution function may miss important information of the surface isotropy. Although some mechanical profilers can measure rough surfaces with a vertical resolution of a few nanometers, the lateral resolution is usually on the order of a micrometer due to the large radius of the stylus probe (Bennett and Mattsson, 1999; Thomas, 1999). On the other hand, the radius of curvature of an AFM probe tip is in the range of 20 - 60 nm; thus, the AFM can provide detailed information of the topography of a small area on the microrough surfaces with a vertical resolution of sub-nanometers and a lateral resolution around 10 nm (Wiesendanger, 1994). Consequently, it is possible to evaluate the area statistics from the

AFM topography measurement. Although attention has been paid to compare the surface statistics determined from the topography measurements to those obtained from the light scattering experiments (Cao et al., 1991; Bawolek et al., 1993; Stover et al., 1998; Nee et al., 2000), little has been done to correlate the area statistics evaluated from the AFM topographic data to the measured BRDF for relatively rough surfaces.

In general, surface roughness is assumed to satisfy the Gaussian statistics in the derivation of the BRDF model and for the surface generation in the Monte Carlo simulation (Beckmann and Spizzichino, 1987; Tang et al., 1998). Furthermore, the surface statistics of the 2-D rough surface are mostly assumed to be isotropic so that the autocorrelation function is independent of the direction. However, the Gaussian distribution may miss important features of natural surfaces because this function does not allow any abrupt event in the rapidly decreasing tails (Guérin, 2002). Very few papers have been devoted to the BRDF of non-Gaussian and anisotropic 2-D rough surfaces. Shen et al. (2001) found that the BRDF models could not predict the subsidiary peak in the measured BRDF of the rough side of a silicon wafer, although reasonable agreement existed between the measurement results and the model predictions within a large angular region around the specular direction. This disagreement could be caused by the Gaussian distribution applied in the BRDF model. Therefore, it is important to examine the actual surface statistics of the rough side of silicon wafers so that a reasonable explanation may be provided for the occurrence of the subsidiary peak.

Besides the surface roughness, thin-film coatings on the rough side of silicon wafers can also greatly change the BRDF. Researchers have applied a hybrid method in the modeling of thin-film coatings on rough substrates (Tang et al, 1999a). In the hybrid

method, thin-film optics is applied to model the interference effect due to the coating, and the ray-tracing algorithm based on the geometric optics approximation is used to model the scattering due to the surface roughness. The hybrid method is computationally effective since its formulation is very similar to that for a rough surface without thin-film coatings. Some agreement has been observed between the predictions using the hybrid method and the measurement results (Tang et al, 1999a). However, there is a dilemma between the two theories in the hybrid method. The geometric optics approximation is applicable to rough surfaces while thin-film optics is appropriate for a layer of coating with perfectly smooth interfaces. Therefore, it is very important to study the validity of the hybrid method so that the advantages of the hybrid method may be exploited in the BRDF modeling of thin-film coated rough surfaces.

The motivations of this thesis are to model the BRDF of the rough side of silicon wafers from the actual surface statistics and to investigate the validity of the hybrid method. The topographic data measured with an AFM are analyzed to obtain the surface statistics. The measured surface statistics may be linked to the key parameters in the wafer manufacturing processes. The predicted BRDF from the measured surface statistics is compared with the measured BRDF to find the correlation between the surface statistics and the BRDF. The established correlation will help the application of the light scattering measurement in the surface roughness characterization. A reasonable explanation for the subsidiary peak observed for the silicon wafer may be provided. Furthermore, for the modeling of thin-film coated rough surfaces, the rigorous electromagnetic-wave solution is performed to study whether the hybrid method is valid.

The comparisons of simulation results from different methods will show the capability and the limitation of the hybrid method.

The organization of this thesis is as follows. Chapter 2 provides a review of the silicon wafer manufacturing, roughness characterization instruments, and theoretical and experimental studies on the BRDF. Chapter 3 presents the roughness measurement and the statistical analysis on the topographic data. The 1-D slope distribution and the 2-D slope distribution are investigated in detail. Chapter 4 describes the three-axis automated scatterometer (TAAS) developed by Shen (2002) and the systematical characterization and further improvements on the TAAS. Chapter 5 applies a geometric optics model to predict the BRDF from the 1-D and the 2-D slope distribution functions. The predicted results are compared with the experimental findings. The correlations between the slope distribution and the BRDF are explained. The instrument effects and the inverse procedure are discussed. Chapter 6 compares the numerical simulation results using the rigorous electromagnetic-wave solution and the hybrid method. The effect of film thickness on the validity of the hybrid method is discussed. A validity regime is presented for a layer of silicon dioxide on a silicon substrate in the visible wavelength region. Finally, Chapter 7 summarizes the conclusions and the suggested future work.

CHAPTER 2

LITERATURE REVIEW

2.1 Silicon Wafer Manufacturing and Rapid Thermal Processing

Silicon is the primary crystalline material in semiconductor manufacturing industry. A smooth silicon wafer can be produced by the following procedure. First, polysilicon is produced from sand by means of a complex reduction and purification process. High purity polycrystalline silicon is melted in a crucible. A seed of single crystal silicon is dipped into the melt and pulled out from the melt gradually. The liquid rises with the seed due to surface tension and cools into a single crystalline ingot. Ends of the ingot are cropped, and the ingot is ground to a uniform diameter with a flat indicating the crystal orientation. Then the ingot is sliced into many silicon wafers. The sliced wafer is mechanically lapped to reduce surface roughness due to the saw cut. The lapped wafer is etched by a chemical solution to remove any remaining microcracks and surface damages. The etched wafer is polished to a mirror surface. Normally only one side of the silicon wafer is polished while the other side remains rough. Finally, the wafer is cleaned by deionized water and dried.

It is common to deposit other materials on a silicon wafer for various applications. For example, the rough silicon wafer can have polysilicon coatings for protection and insulation. Some coatings on the rough side are beneficial to attract defects within the silicon wafer during annealing.

Many steps in semiconductor manufacturing require thermal processing, such as the growth of films, annealing and so on (Timans, et al., 2000). For example, ion

implantation is a good method to tune the conductivity of silicon because of its inherent doping controls. The doped wafer has to be thermally annealed to restore the crystal structure and reduce the stress due to the implanting of heteroatoms (Timans, et al., 2000). The general trend of thermal processing is to reduce the process temperature and duration time as much as possible in order to restrict the motion of atoms through diffusion (Timans, et al., 2000). Traditionally, the annealing process is performed within a batch furnace. Wafers in the batch furnace cannot be heated up uniformly because their edges heat up faster than their centers (Fan and Qiu, 1998). Furthermore, the temperature difference of the wall can affect the quality of the whole batch. Rapid thermal processing (RTP) is a promising way to replace the traditional batch furnace method since it provides flexibility to the temperature control. A RTP furnace can heat one individual wafer to a specified temperature in a short period of time mainly through radiation heat transfer. It can make all the points on the wafer experience the same temperature-time cycle as defined in the process recipe (Timans, et al., 2000).

In many RTP furnaces, the temperature of the silicon wafer is monitored by a radiation thermometer viewing the rough side of the wafer. However, the determination of the spectral emissivity of a rough surface is very difficult. Some research has been devoted to the modeling of the spectral hemispherical emissivity for a rough surface (Demont et al., 1982, Vandenabeele and Maex, 1992; Xu and Sturm, 1995; Bhushan et al., 1998; Zhou and Zhang, 2003). Besides the surface roughness, the thin-film coating can significantly change the emissivity. Bidirectional reflectance of coated surfaces can be very different from that of the substrate (Yeh, 1988; Sorrell and Gyurcsik, 1993). Furthermore, since the rough side of the wafer and the lower chamber of the RTP furnace

compose an enclosure, the apparent emissivity should be used to determine the temperature of the wafer (DeWitt el al., 1997; Zhang, 2000). In order to model the effective emissivity of the wafer, a thorough understanding of the bidirectional reflectance of the wafer surface is necessary.

2.2 Roughness Measurement

Real surfaces all show some extent of roughness. Roughness can be imagined as asperities (microfacets) on the surface from a microscopic view. The summation of the altitudes of the asperities with respect to the mean plane is zero. The lateral and vertical scales of the asperities can be very large, as peaks and valleys in a mountain, or can be very small, such as a small particle on a mirror. In this thesis, the roughness refers to the microroughness. The lateral and vertical dimensions of asperities on a microrough surface are in the order of micrometers.

The pattern of light scattering can be greatly changed by surface roughness. If a surface is very smooth, like a mirror, most of the incidence light is reflected to the specular direction. If a surface is rough, the scattered radiation usually exists in the whole hemisphere above the surface. The surface profile of a deterministic rough surface can be described by a function. One of the specific groups of the deterministic surface is the periodic surface. The scattered radiation on a periodic surface can exist only in a finite number of directions instead of the whole hemisphere due to diffraction. However, in general, the precise definition equation of the surface profile is unknown or of little interest, the shape of the rough surface is described by a random function of space coordinates (Saillard and Sentenac, 2001). Only the random rough surface is studied in

this thesis. Since light scattering is strongly dependent on the surface roughness, it is crucial to study the statistics of real surfaces.

We can roughly sense the surface roughness using the thumbnail and the eye. Both methods are completely subjective. Various types of instruments can be used to map the surface topography. Some instruments are following the tactile example of the nail, i.e., using a stylus probe. Some are mimicking the eye, i.e., using an optical method. The detailed information about the roughness instrumentation can be found in references (Whitehouse, 1997; Bennett and Mattsson, 1999; Thomas, 1999). A short review is provided in the following for some commonly used instruments in the microelectronics industry and optical engineering.

2.2.1 *Mechanical Profiler*

As a stylus is dragged over a rough surface, it moves up and down when it rides over peaks and valleys on the surface. The deviation of the stylus from a reference (a skid) can be transformed to an electrical signal and the surface profile can be determined from the signal. The vertical resolution of the stylus profiler is around 1 nm. The lateral resolution is limited by the radius of the tip. The radius of curvature of a tip can be 2 μm, 5 μm, and 10 μm according to the ISO standard (Thomas, 1999). The smallest radius of curvature of the tip can reach 0.2 μm (Bennett and Mattsson, 1999). Consequently, the shortest surface roughness wavelength that can be measured by the mechanical profiler is around 0.2 μm. One issue for the mechanical profiler is the load of the stylus. The force exerted by the stylus may be greater than 1 μN so that it may scratch or even damage the scanned surface. Another issue is that most mechanical profilers can only perform the

line scan, although a very limited number of models can perform the area scan. If area profiling is required, the scan time will be very long since the stylus has to raster the whole area.

2.2.2 *Scanning Probe Microscope*

The atomic force microscope (AFM) and the scanning tunneling microscope (STM) belong to the family of the scanning probe microscope (SPM) (Wiesendanger, 1994). The name of the SPM comes from the probe, like a stylus in phonograph, rastering a sample. The birth of the SPM gives a marvelous way for scientists and engineers to view the fine feature in atomic scale.

The first member of the SPM family is the STM. Although the STM can map the surface feature in marvelous vertical and lateral resolutions, the underlying physics determine that the STM can work only for conductive surfaces. Binning et al. (1996) introduced the first atomic force microscope. Figure 2.1 shows the principle of an AFM. When a sharp tip is very close to a sample, there is a repulsive force between the tip and the sample. This force can cause the bending of a cantilever where the tip is attached. In the first AFM, a technique similar to the STM was used to detect the deflection of the cantilever. In the current AFMs, an optical method is popular to detect the bending of the cantilever because it induces little noise into the microscope. Generally, the tip and the cantilever are made of silicon, silicon dioxide, or silicon nitride. The radius of the tip can be as small as 10 nm so that the AFM can map the fine features with an excellent lateral resolution. The vertical resolution of the AFM can achieve 0.1 nm. Because the tip has to raster scan a selected area, the scan rate of the AFM is usually slow.

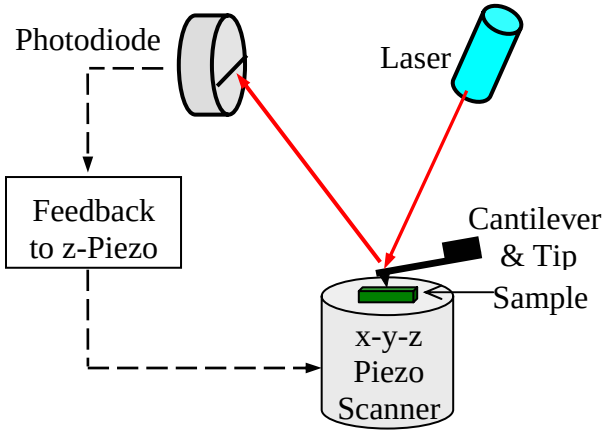

Figure 2.1 Schematic drawing of an AFM.

2.2.3 *Optical Interferometric Microscope*

The optical interferometric microscope (OIM) exploits the wave behavior of light. The main part of the OIM is an interferometer. Light from a source is split into two parts by a beamsplitter in the interferometer. A part of the light is reflected back by the rough surface, and the other part is reflected by a reference surface. Because two lights are from the same coherent source and the optical paths are different, they can generate an interferogram, which represents the topography of the surface. The interferogram is pictured by a charged couple device (CCD) camera. Sophisticated hardware and software are necessary to extract the surface height information from the interferogram.

The most popular interferometric techniques are the phase shift interferometry (PSI) and the scanning white light interferometry (SWLI) (Wyant et al., 1986). The light source in the PSI is a monochromatic source, and the PSI is applicable for slightly rough surfaces. The vertical resolution of the PSI is in the sub-nanometer range. If the surface is moderately rough (the height difference between the adjacent peak and valley is greater than a quarter of the selected wavelength), the PSI cannot result in a correct topographic

image for the surface. For relatively rough surfaces, the SWLI is a better way for roughness measurement. In the SWLI, the light source is a wide-band source instead of a monochromatic source. The basic principle of the SWLI is that the maximum intensity for white-light fringes occurs when the optical path difference is zero. When the optical path difference is varied, an intensity envelope is recorded for each point on the surface. The height information is deduced from the maximum in the intensity envelope. The vertical resolution of the SWLI is about 1-2 nm, larger than that of the PSI. The OIM has a large field of view and the image can be obtained in a few seconds. Since the interferogram is dependent on the phase or the intensity of the reflected light, the surface condition may deteriorate the measurement result if the reflectivity is not uniform over the scan area. Furthermore, the OIM may not be applicable to surfaces with steep asperities since the reflected light may be not collected by the optical system.

2.2.4 *Other Probe Techniques*

The instruments mentioned in Sec. 2.2.1-2.2.3 can provide the topographic data for the measured surface. Some other instruments do not provide the topographic data, but provide the statistical information of the roughness (Stover, 1995; Bennett and Mattsson, 1999). Total integrated scattering (TIS) and angle-resolved scattering are two examples of techniques using the light scattering method. A reverse procedure is necessary to obtain the roughness parameters from the available models. A detailed discussion of the regime of surface roughness parameters measurable with the light scattering method can be found in Vorburger et al. (1993).

2.3 Theoretical Study of the Bidirectional Reflectance

When radiation is reflected by a rough surface, the reflected energy will be distributed in the hemisphere, and furthermore, the distribution of energy is generally dependent on the incoming direction. Therefore, it is necessary to use two directions to describe the reflection by a rough surface (Nicodemus, 1970; Barnes et al., 1998). Bidirectional reflectance is a fundamental radiative property of rough surfaces in thermal science (Brewster, 1992; Modest, 1993; Siegel and Howell, 2002). The study of the bidirectional reflectance is also important to other subjects. In optical engineering, the bidirectional reflectance is used as a tool to characterize the surface roughness. In object rendering, efficient bidirectional reflectance models are sought to achieve fast and vivid object rendering (Phong, 1975; He et al., 1991). The theories on the scattering from rough surfaces can be found in several books and review papers (Tang et al., 1999b; Saillard and Sentenac, 2001; Tsang et al., 2001; Warnick and Chew, 2001; Zhang et al., 2003).

For an ideally smooth surface, there is no scattering and all the radiation is reflected to the specular direction. For an ideally diffuse surface, the reflected radiation in any direction is the same. However, the scattering on a real random surface is neither the specular reflection nor the ideal diffuse reflection. Roughly speaking, the bidirectional reflection may be divided into three components, a specular spike at the specular direction, a specular lobe around the specular direction, and a diffuse term covering all the reflection angles. In order to quantitatively describe the energy distribution of the scattered radiation, it is necessary to define the bidirectional reflectance distribution function (BRDF). The geometry to illustrate the definition is shown in Figure 2.2. The *x*- and *y*-axes are located in the mean plane of the rough surface, and the *z*-axis is normal to

the mean plane. The BRDF, also called the bidirectional reflectance, is the ratio of the reflected radiance (or intensity in most heat transfer textbooks) to the incident irradiance (Nicodemus, 1970; Barnes et al., 1998; Siegel and Howell, 2002),

$$f_r(\theta_i, \phi_i; \theta_r, \phi_r) = \frac{L_r(\theta_i, \phi_i, \theta_r, \phi_r)}{L_i(\theta_i, \phi_i)\cos\theta_i d\omega_i} \ [\mathrm{sr}^{-1}] \tag{2.1}$$

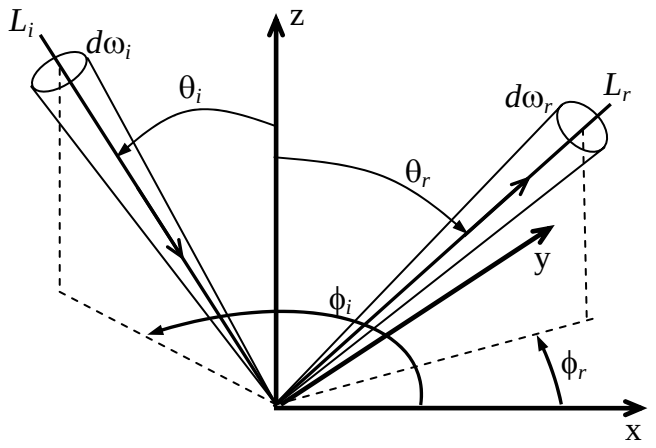

Figure 2.2 Geometry for the definition of BRDF.

In the above equation, (θ_i, ϕ_i) and (θ_r, ϕ_r) denote the incoming and scattering directions, respectively, L_i is the incoming radiance, $L_i \cos\theta_i \, d\omega_i$ represents the incident irradiance (power per unit projected area), the reflected radiance L_r is a function of both the incoming and scattered directions. Since radiance is a spectral property, BRDF is also a spectral property. The dependence on the wavelength of the incident radiation λ is not shown in Eq. (2.1) for the sake of simple notation. Both the theoretical analysis and the experimental measurement are mainly devoted to finding the variation of the reflected radiance (or reflected power) with the reflection angle (θ_r, ϕ_r) when the incidence is fixed at the direction of (θ_i, ϕ_i).

2.3.1 *Rigorous Electromagnetic-Wave Solution*

There are two main categories in the rigorous EM-wave solution: integral equation methods and differential equation methods. The boundary integral method is one example of the integral equation methods. Differential equation methods include the finite-difference time domain (FDTD) method, the volume finite-element method, and the differential method. The integral equation method can deal with homogeneous media surrounded by a boundary. The differential method can deal with inhomogeneous media as well (Saillard and Sentenac, 2001). The differential method requires volumetric meshes; therefore, the number of unknowns may be larger than that required by a surface mesh (Warnick and Chew, 2001).

The boundary integral method is the most common method of the numerical simulation of light scattering. This method is based on the extinction theorem (Wolf, 1973) and Green's theorem (Kreyszig, 1993). Maradudin et al. (1990) and Sánchez-Gil and Nieto-Vesperinas (1991) applied this method to study the scattering by one-dimensional dielectric rough surfaces. Assuming that light of *p*-polarization is incident on a one-dimensional rough surface from vacuum, with the magnetic field H in the y direction, the formulas governing the light scattering are

$$H_0(\mathbf{r}) = H_i(\mathbf{r}) + \frac{1}{4\pi}\int_{\Sigma}\left[H_0(\mathbf{r}')\frac{\partial G_0(\mathbf{r},\mathbf{r}')}{\partial n} - G_0(\mathbf{r},\mathbf{r}')\frac{\partial H_0(\mathbf{r})}{\partial n}\right] d\mathbf{r}' \qquad (2.2)$$

$$0 = -\frac{1}{4\pi}\int_{\Sigma}\left[H_s(\mathbf{r}')\frac{\partial G_s(\mathbf{r},\mathbf{r}')}{\partial n} - G_s(\mathbf{r},\mathbf{r}')\frac{\partial H_s(\mathbf{r}')}{\partial n}\right] d\mathbf{r}' \qquad (2.3)$$

where $\mathbf{r} = (x, z)$, $z = \xi(x)$ at the boundary Σ, G is the Green function, and n is the normal at the position $\mathbf{r}'$ on the boundary. In Eq. (2.2), $\mathbf{r}$ and $\mathbf{r}'$ are in vacuum, while in Eq. (2.3),

r is in vacuum and **r′** is in the medium. The subscripts 0 and *s* stand for vacuum and the medium, respectively. H_0 are H_s are linked by the boundary conditions:

$$H_0(\mathbf{r}) = H_s(\mathbf{r}) \tag{2.4a}$$

$$\frac{\partial H_0(\mathbf{r})}{\partial n} = \frac{1}{\varepsilon_s}\frac{\partial H_s(\mathbf{r})}{\partial n} \tag{2.4b}$$

The coupled equations (2.2) and (2.3) should be solved simultaneously. The intensity in far field can be calculated from the magnetic field *H* and its normal derivative $\partial H / \partial n$ at the boundary (Maradudin et al., 1990; Sánchez-Gil and Nieto-Vesperinas, 1991)

The boundary integral method has been extensively used to explain the backscattering on rough surfaces. Maradudin et al. (1990) found that there exists a critical refractive index for the occurrence of backscattering, and furthermore, the critical value becomes smaller with the increase of roughness. This method can also be applied to verify the simulation results using the Kirchhoff approximation (Chen and Fung, 1988; Thorsos, 1988; Sánchez-Gil and Nieto-Vesperinas, 1991) and the geometric optics approximation (Tang and Buckius, 1997).

A lot of work has been done on scattering from the one-dimensional rough surface using the rigorous numerical simulation. The simulation for the two-dimensional rough surfaces based on the rigorous approach is very computationally intensive, and only a few cases for perfect conductors and metals are available (Pak et al., 1995; Johnson et al., 1996). Because of the large number of unknowns in the formulation for two-dimensional surfaces, directly solving the matrix equation is not feasible. Consequently, an iterative method should be applied (Warnick and Chew, 2001). In general, the rigorous approach requires a large memory and a long computation time.

Therefore, several approximation methods have been developed to facilitate a fast simulation of light scattering by rough surfaces.

2.3.2 *Kirchhoff's Approximation*

In the rigorous electromagnetic-wave (EM-wave) approach, the electromagnetic field at the boundary is unknown. In the Kirchhoff approximation, the field at a certain point at the boundary is the same as that on a tangential plane passing through the point (Beckmann and Spizzichino, 1987). The total electric field $\boldsymbol{E}$ is the summation of the incidence field $\boldsymbol{E_i}$ and the reflected field, i.e.,

$$\mathbf{E} = (1+r)\mathbf{E}_i \tag{2.5}$$

where the local Fresnel reflection coefficient r is dependent on the slope at each point. The Kirchhoff approximation is also called the tangent plane approximation. In general, the Kirchhoff approximation is valid for a rough surface with a radius of curvature much larger than the wavelength of the incident radiation λ (Beckmann and Spizzichino, 1987). In other words, the Kirchhoff approximation is only applicable to gently undulating surfaces. Unlike the rigorous approach, there is no need to solve the coupled equations.

The applicable region of the Kirchhoff approximation has been established for perfectly conducting surfaces (Chen and Fung, 1988; Thorsos, 1988; Sánchez-Gil and Nieto-Vesperinas, 1991). It is commonly believed that the Kirchhoff approximation can still give the reliable result when the rms roughness σ and the autocorrelation length τ are less than or comparable to λ and the ratio of σ to τ is less than 0.3 (Tang and Buckius, 1998). Chen and Fung (1988) claimed that the Kirchhoff approximation is reliable at

small angles of incidence when the ratio of τ to λ is less than 0.3 and the ratio of σ to λ is less than 0.03.

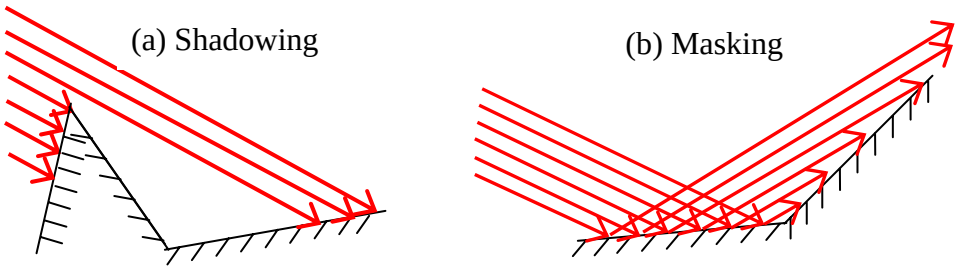

Figure 2.3 Shadowing (a) and Masking (b) effects.

Figure 2.3 shows the shadowing and masking effects. Some of surface asperities are not illuminated since the incident radiation is blocked. This is referred to shadowing effect. Similarly, when the radiation is reflected by surface asperities, it may be not able to leave the rough surface if the reflected radiation is directed to other surface asperities. This is referred to masking effect, or outgoing shadowing. The intercepted beam can bounce back and forth on the rough surface until it finally leaves the rough surface. This is referred to multiple scattering. The original Kirchhoff approximation takes into account only the single scattering (the first-order scattering). Bruce and Dainty (1991) incorporated multiple scattering into the Kirchhoff approximation to model light scattering by relatively rough surfaces. Sánchez-Gil and Nieto-Vesperinas (1991) demonstrated that the valid region of the Kirchhoff approximation can be even larger for dielectric surfaces than for metal surfaces since multiple scattering on dielectric surfaces is not as significant as that on metal surfaces.

2.3.3 *Geometric Optics Approximation*

In the geometric optics approximation, the rough surface is imaged as a combination of numerous microfacets which are randomly oriented on the mean plane (Torrance and Sparrow, 1967; Tang and Buckius, 1998 and 2001). The dimension of the microfacet is much larger than λ. The surface of the microfacet is assumed to be ideally smooth, and the reflection of the radiation on the microfacet obeys Snell's law. Figure 2.4 shows the angular relationships between the incident beam and the reflected beam when the specular reflection takes place on the surface of a microfacet *m*. The microfacet normal **n** bisects the incident beam and the reflected beam. The reflectivity of the microfacet is dependent on the local incidence angle ψ, which is defined by the incident beam and the microfacet normal. The orientation of the microfacet, i.e., the direction of **n**, can be defined by an inclination angle α and an azimuthal angle (not shown in Figure 2.4). The orientation of the microfacet can be presented by its slopes as well. The slopes are related to the incoming and scattering directions by

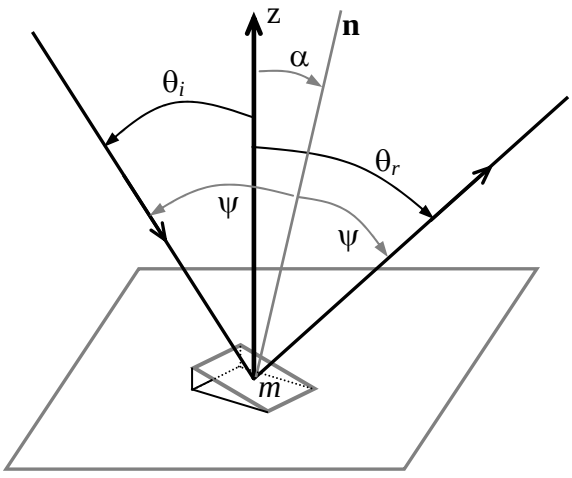

Figure 2.4 Illustration of the specular reflection on a microfacet.

$$\zeta_x = -\frac{\sin\theta_i \cos\phi_i + \sin\theta_r \cos\phi_r}{\cos\theta_i + \cos\theta_r} \tag{2.6a}$$

$$\zeta_y = -\frac{\sin\theta_i \sin\phi_i + \sin\theta_r \sin\phi_r}{\cos\theta_i + \cos\theta_r} \tag{2.6b}$$

The diffraction and interference are ignored in the geometric optics approximation. From a statistical point of view, the radiation reflected into a finite solid angle is proportional to the reflectivity of the microfacet and the probability to find the microfacets with corresponding slopes. The shadowing and masking effect may become significant at large incidence angles and large reflection angles. The effect due to multiple scattering may become significant for very rough surfaces, and it needs to be included in the modeling.

Generally speaking, the applicable roughness region of the geometric optics approximation is $\sigma > \lambda$ and $\tau > \lambda$. Tang et al. (1997) established a validity region for one-dimensional perfectly conducting rough surfaces. They found that the valid region can be extended to $\sigma\cos(\theta_i)/\lambda > 0.2$ and $\sigma/\tau < 2$ with reasonable accuracy. Although the validity region for two-dimensional rough surfaces has not been systematically investigated, Tang et al. (1997) believed that the validity region for one-dimensional rough surfaces may apply to two-dimensional rough surfaces. In the simulations using the ray-tracing algorithm based on the geometric optics approximation, the surface generation method (Tang et al., 1997; Tang and Buckius, 1998) is very common. In addition, the microfacet slope method has also been explored by Zhou et al. (2002) and Prokhorov and Hanssen (2003). The microfacet slope method requires less computation time than the surface generation method.

2.3.4 *BRDF Models*

Specular model describes the bidirectional reflection on an ideally smooth surface. The BRDF is zero everywhere except for at the specular direction (θ_i, ϕ_i +180°),

$$f_r(\theta_i,\phi_i,\theta_r,\phi_r)=\frac{\rho(n,\kappa,\theta_i)}{\cos\theta_r}\delta(\theta_r-\theta_i)\delta[\phi_r-(\phi_i+180°)] \tag{2.7}$$

where $\rho(n,\kappa,\theta_i)$ is the reflectivity of the smooth surface, and δ is the Kronecker delta function.

Diffuse model describes the bidirectional reflection from an ideally diffuse surface. The BRDF is independent of the reflection angle,

$$f_r(\theta_i,\phi_i,\theta_r,\phi_r)=\frac{\rho_{d-h}(n,\kappa,\theta_i)}{\pi} \tag{2.8}$$

where $\rho_{d-h}(n,\kappa,\theta_i)$ is the directional-hemisphere reflectance of the diffuse surface.

The surface power spectral density (PSD) function is popular to present the roughness statistics. In the "golden rule" derived based on the Rayleigh-Rice perturbation theory, the BRDF is related to the PSD function (Stover, 1995; Bennett and Mattsson, 1999),

$$f_r(\theta_i,\phi_i,\theta_r,\phi_r)=\frac{16\pi^2}{\lambda^4}Q\cos\theta_i\cos\theta_r\ \mathrm{PSD} \tag{2.9}$$

where Q is a factor considering the reflectance of the surface.

One model is derived based on the Kirchhoff approximation and Gaussian roughness statistics (Beckmann and Spizzichino, 1987). The specular component and the off-specular component of the BRDF for an illuminated surface with a rectangle area $l_x \times l_y$ are

$$f_{r,spe} = \frac{l_x l_y \cos\theta_i}{\lambda^2 \cos\theta_r} \exp(-g) \operatorname{sinc}^2\left[\frac{\pi l_x}{\lambda}(\sin\theta_i - \sin\theta_r \cos\phi_r)\right] \cdot \operatorname{sinc}^2\left(\frac{\pi l_y}{\lambda} \sin\theta_r \sin\phi_r\right) \tag{2.10a}$$

$$f_{r,off} = \frac{\pi \cos\theta_i \tau^2}{\lambda^2 \cos\theta_r} \left[\frac{1 + \cos\theta_i \cos\theta_r - \sin\theta_i \sin\theta_r \cos\phi_r}{\cos\theta_i (\cos\theta_i + \cos\theta_r)}\right]^2 \exp(-g) \cdot \sum_{m=1}^{\infty} \frac{g^m}{m! m} \exp\left[\left(-\frac{\pi^2 \tau^2}{m\lambda^2}(\sin^2\theta_i - 2\sin\theta_i \sin\theta_r \cos\phi_r + \sin^2\theta_r)\right)\right] \tag{2.10b}$$

where $\operatorname{sinc}(x) = \sin(x)/x$, and the optical smoothness is

$$g = [2\pi\sigma(\cos\theta_i + \cos\theta_r)/\lambda]^2 \tag{2.11}$$

Torrance and Sparrow (1967) assumed that the distribution function of the inclination angle α of the microfacets is Gaussian and derived a semi-empirical BRDF model,

$$f_r(\theta_i, \phi_i, \theta_r, \phi_r) = \frac{b \exp(-c^2\alpha^2)}{4\cos\theta_i \cos\theta_r} \rho(\psi) G + a \tag{2.12}$$

where constants *b* and *c* define the distribution function of the inclination angle. *G* is the geometrical attenuation factor to include the effect of shadowing. The diffuse term in the BRDF is represented by *a*. All constants have to be fitted by the experimental results.

Caron et al. (2003) derived the ratio of the scattered radiance to the incident power flux following the static-phase formulation (Tsang and Kong, 1980; Kong, 1990). For in-plane scattering,

$$f_r(\theta_i, \phi_i, \theta_r, \phi_r) = \frac{p(\zeta_x, \zeta_y)}{4\cos\theta_i \cos\theta_r \cos^4\alpha} \rho(\psi) \tag{2.13}$$

where *p* is the probability density function with respect to slopes (ζ_x , ζ_y) of microfacets. In the plane of incidence, $\phi_i - \phi_r = 0°$ or 180°, $\alpha = |\theta_r - \theta_i|/2$, and $\psi = (\theta_i + \theta_r)/2$. The *y*-

component of the slope has to be zero so that the reflected beam can fall to the plane of incidence.

Tang and Buckius (2001) developed a comprehensive statistical model based on the geometric optics approximation. This model includes contributions from both first-order scattering and multiple scattering. The BRDF for the first-order scattering (i.e., the radiation is reflected once by a microfacet before leaving the surface) can be presented as

$$f_r(\theta_i,\phi_i,\theta_r,\phi_r)=\frac{p(\zeta_x,\zeta_y)(1+\zeta_x\tan\theta_i)d\zeta_x d\zeta_y}{\cos\theta_r\sin\theta_r d\theta_r d\phi_r}\rho(\psi)S(\theta_i)S(\theta_r) \quad (2.14)$$

where $S(\theta_i)$ and $S(\theta_r)$ are the shadowing functions (Smith, 1967) for shadowing and masking effect, respectively.

The slope distribution is most commonly modeled as a Gaussian function (Torrance and Sparrow, 1967; Tang and Buckius, 2001; Caron et al., 2003). The two-dimensional probability density function (PDF) of slopes for an isotropic surface can be written as

$$p(\zeta_x,\zeta_y)=\frac{1}{2\pi\zeta_{\text{rms}}^2}\exp\left(-\frac{\zeta_x^2+\zeta_y^2}{2\zeta_{\text{rms}}^2}\right) \quad (2.15)$$

where ζ_{rms} stands for the rms slope, which is the same in all directions. A simple relation exists for rough surfaces that satisfy the Gaussian statistics (Beckmann and Spizzichino, 1987): $\zeta_{\text{rms}}=\sqrt{2}\sigma/\tau$.

Specular model and diffuse model are for ideal surfaces, and they have little use in modeling the BRDF for real surfaces. The "golden rule" is based on Rayleigh-Rice's perturbation theory, and therefore it is only applicable to a surface whose rms roughness is much smaller than λ. Equations (2.10), and (2.13) through (2.15) are derived either

from the Kirchhoff approximation or from the geometric optics approximation. Therefore, the validity region for these analytical models is constrained by the validity region of the corresponding approximation methods. Eqs. (2.13) through (2.15) are all based on the geometric optics approximation, the only difference in the derivations is whether the distribution function is related to the inclination angle or to the slopes. Therefore, it might be possible to unify these equations to one identical formulation.

2.3.5 *Modeling the Scattering from Coated Surfaces*

The study of scattering from thin-film coated surfaces is very important in optical, materials, and thermal engineering. Many optical components and semiconductor wafers are coated with thin films according to different applications. The BRDF and the emissivity of thin-film coated surfaces can be very different from those of the substrate. The theory on the reflection from a multilayer system with ideally smooth interfaces is well developed (Yeh, 1988). According to thin-film optics, the amplitude of the reflected wave from a three-layer system with ideally smooth interfaces is (Brewster, 1991; Siegel and Howell, 2002)

$$r_f = \frac{r_{0,f} + r_{f,s}\exp(-j2\beta)}{1 + r_{0,f} r_{f,s}\exp(-j2\beta)} \tag{2.16}$$

where $r_{0,f}$ and $r_{f,s}$ are the Fresnel reflection coefficients between air and film and between film and substrate, respectively. The phase shift of wave traveling through the thin film is

$$\beta = \frac{2\pi n_f h \cos(\theta)}{\lambda} \tag{2.17}$$

where n_f is the refractive index of the film, h is the film thickness, and θ is the refraction angle within the film.

On the contrary, the scattering of radiation by thin-film coatings on a rough surface is extremely difficult to analyze. A correction factor can be added to the Fresnel reflection coefficients to calculate the partially coherent reflectance and transmittance of a multilayer structure with rough interfaces (Filinski, 1972; Mitsas and Siapkas, 1995). The first-order vector perturbation theory (Elson, 1977; Bruno et al., 1995) and the Kirchhoff approximation (Lettieri et al., 1991; Icart and Arques, 2000; McKnight, 2001) can be applied to simulate the scattering from multilayer systems. However, these methods are only applicable to either very smooth surfaces or gently undulating surfaces (Elson, 1977; Beckmann and Spizzichino, 1987).

The geometric optics approximation is extensively used in analytical models and Monte Carlo simulation. Good agreement has been observed between the simulation results employing the geometric optics approximation and the rigorous electromagnetic-wave solution for a rough surface without thin-film coatings (Tang et al., 1998), and the simulation is very computationally effective. Since the simulation based on the rigorous electromagnetic-wave solution becomes formidable if there are thin-film coatings on a rough substrate, it is worthwhile to explore other alternative methods. Some previous works (Tang et al., 1999a) assumed that the reflection on the thin-film coating could be well described by thin-film optics considering interference effects whereas the roughness effect can be modeled using the geometric optics approximation through the ray-tracing method. After the reflectivity of the microfacet without thin-film coatings is replaced by that with thin-film coatings, the analytical models and the developed programs applying the Monte Carlo simulation can be used for modeling of the BRDF for coated rough surfaces. The reflectivity of each coated microfacet is determined from Eqs. (2.16) and

(2.17). Figure 2.5 shows the schematic of reflection from thin-film coatings on a smooth substrate and a rough substrate. Equation (2.16) is derived for a thin film on an ideally smooth plane; therefore, each wave reflected by the air-film interface and the one reflected by the film-substrate interface can be accounted for. However, the microfacet on the rough surface has a finite (usually very small) area although the surface of the microfacet is smooth. Because of the small area of a microfacet, an incident ray on the microfacet can emerge from the nearby microfacet after it travels in the film, first towards the substrate and then towards the air. Hereafter, this will be referred as the corner effect. Because of the corner effect, the application of Eq. (2.16) for the coated microfacet may not well describe the interference of a thin film on a rough substrate.

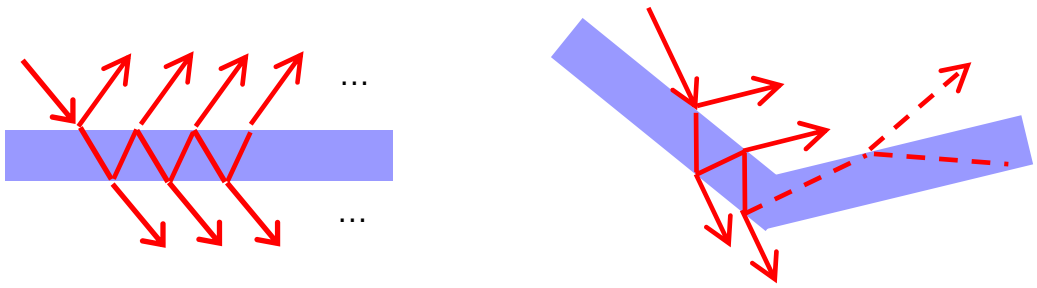

(a) a smooth substrate (b) a rough substrate

Figure 2.5 Schematic drawing of reflection from thin-film coatings on a smooth substrate (a) and a rough substrate (b).

Tang et al. (1999a) applied the surface generation method (SGM) to evaluate the BRDF for thin-film coated surfaces. Zhou and Zhang (2003) and Lee et al. (2004) used the microfacet slope method (MSM) to model the radiative properties of thin-film coated opaque or semi-transparent surfaces. Some agreement has been demonstrated between the modeling results and the experimental measurement (Tang et al., 1999a). It indicates

that the hybrid method may be applicable for some rough surfaces. Therefore, it is necessary to study the validity of the hybrid method so that the advantages of the hybrid method may be exploited in the BRDF modeling of thin-film coated rough surfaces.

2.4 Experimental Study of the Bidirectional Reflectance

2.4.1 *BRDF Instrumentation*

Experimental studies are necessary to verify the predicted results from various models and numerical simulations. The instrument used to measure the bidirectional reflectance is called a bidirectional reflectometer or scatterometer. Some scatterometers can also measure the bidirectional transmittance (Proctor and Barnes, 1996; Barnes et al., 1998). Different types of bidirectional reflectometers are available for research and industrial applications (Zipin, 1966; Anderson et al., 1988; Drolen, 1992; Feng et al., 1993; Roy et al., 1993; Zaworski et al., 1996a; White et al., 1998). Although the sophistication varies from instrument to instrument, the essential components of a scatterometer are the same: namely, an optical source, a goniometric table, and a detection and data acquisition system. The wavelengths of the measurements are usually in the visible and near-infrared regions due to the difficulty encountered for shorter or longer wavelengths. A grating monochromator or a coherent laser source can provide a narrow band optical radiation, which is nearly collimated. A spectrometer in the detector assembly could perform the same function as the monochromator (Feng et al., 1993).

There is a variety of designs of the goniometric table, which manipulates the movements of the detector, sample, and/or optical source. If only in-plane measurements (i.e., the reflected light is confined to the plane of incidence) are needed, two coaxial

rotary stages are sufficient to vary the incidence and reflection angles. Therefore, the scatterometer is relatively easy to construct (Zipin 1966; Roy et al., 1993). The Spectral Tri-function Automated Reference Reflectometer (STARR) at NIST is a high-accuracy reference instrument for the in-plane BRDF measurement in the visible and near-infrared regions (Proctor and Barnes, 1996; Barnes et al., 1998). A few designs have been realized for out-of-plane measurements (Anderson et al., 1988; Drolen, 1992; Feng et al., 1993; Zaworski et al., 1996a; White et al., 1998; Shen et al., 2003). Usually, a flexible hardware design for the goniometric table is desired so that it can move the source, sample, and detector to different combinations of incidence and viewing angles. In some systems, the source is stationary while the detector and the sample holder are movable (Anderson et al., 1988; Drolen, 1992; Zaworski et al., 1996a; Shen, 2002). The advantage of a fixed source is that virtually there is no limit on the size and weight of the source (Zaworski et al., 1996a). The circular-track design is another way to rotate the source and detector around the sample; however, the long-term stability and eccentricity requirements may be difficult to meet (White et al., 1998). In order to measure the scattering and its associated polarization states, an out-of-plane ellipsometry scatterometer has been developed by Germer and Asmail (1999). In this design, the sample can be rotated in both its vertical and horizontal axes.

2.4.2 *BRDF Measurements and Modeling*

Several researchers measured samples by applying different microscopic probe techniques and analyzed the PSD function for these surfaces. Polished silicon wafers and wafers with polysilicon coatings were measured, and the surface statistics were presented

in the form of the PSD function. Vatel et al. (1993) and Muller et al. (2001) studied the PSDs of polished silicon wafers and polysilicon coated wafers. Dumas et al. (1993) calculated the PSD function of optical-glass surfaces using the AFM topographic data and reported that the result was satisfactorily comparable to the optical scattering data over a large range of spatial frequencies. Jahanmir and Wyant (1992) measured various samples using an optical profilometer and a scanning probe microscope. They compared the rms roughness and the average roughness for those samples. Marx et al. (1998) measured silicon wafers with various ranges of roughness using different instruments including the AFM and the interferometric profilometer. However, they did not measure the roughness of wafers whose last processing stage was lapping. Most of the surfaces studied in the published literature have low levels of roughness. Rare research has been carried out to study the surface statistics of the backside of silicon wafers, whose rms roughnesses may be as large as several hundred nanometers.

The slope distribution function is a key input in the analytical models based on the geometric optics approximation (Torrance and Sparrow, 1967; Bennett and Mattsson, 1999; Caron et al., 2003). Before the invention of the atomic force microscope (AFM), the surface profile was usually measured with a mechanical profiler that scans the surface line-by-line. Therefore, the estimated one-dimensional slope distribution function may miss important information of the surface isotropy. On the other hand, the AFM can provide detailed information of the topography of a small area on the microrough surfaces with a vertical resolution of sub-nanometers and a lateral resolution around 10 nm (Wiesendanger, 1994). Consequently, it is possible to evaluate the area statistics from the AFM topography measurement. Although attention has been paid to compare the

surface statistics determined from the topography measurements to those obtained from the light scattering experiments (Cao et al., 1991; Bawolek et al., 1993; Stover et al., 1998; Nee et al., 2000), little has been done to correlate the area statistics evaluated from the AFM topographic data to the measured BRDF for relatively rough surfaces.

In general, surface roughness is assumed to satisfy the Gaussian statistics in the derivation of the BRDF model and for the surface generation in the Monte Carlo simulation (Beckmann and Spizzichino, 1987; Tang et al., 1999). Furthermore, the surface statistics of the two-dimensional rough surface are mostly assumed to be isotropic so that the autocorrelation function is independent of the direction. Very few papers have been devoted to the BRDF of non-Gaussian and anisotropic two-dimensional rough surfaces. Shen et al. (2001) found that the BRDF models could not predict the subsidiary peak in the measured BRDF of the rough side of a silicon wafer, although reasonable agreement existed between the measurement results and the model predictions within a large angular region around the specular direction. This disagreement could be caused by the Gaussian distribution applied in the BRDF model. Therefore, it is important to examine the actual surface statistics of the rough side of silicon wafers so that a reasonable explanation may be provided for the occurrence of the subsidiary peak.

The BRDFs of both metal and dielectric surfaces at various wavelengths and temperatures have been reported. Drolen (1992) investigated the wavelength effect and directional dependence of radiative properties for spacecraft thermal control materials. Ford et al. (1995) used a Fourier transform infrared spectrometer to measure BRDF in the near-infrared and infrared wavelength ranges. Their results cover a broad spectral range from 2.5 to 15 μm with a low angular resolution, which is due to the large solid angle of

the instrument. Roy et al. (1993) measured the directional reflectance of several dielectric materials at temperatures up to 1100°C.

The measured BRDF can be inputted into the Monte Carlo simulation to improve the accuracy of the modeling. Zaworski et al. (1996b) incorporated the measured BRDF data for paints in the simulation of the spatial distribution of light through a gap made of two painted plates. A number of techniques had to be introduced to interpolate or extrapolate the experimental data due to the resolution and limitation of the measured BRDF. Reasonable agreement was found between the measured BRDF and the predicted result. Zhou et al. (2002) studied the BRDF of a rough silicon wafer and the apparent emissivity of the wafer in a RTP furnace. They found that the predicted BRDFs show similar magnitudes and trends to the measured BRDF.

CHAPTER 3

SURFACE ROUGHNESS CHARACTERIZATION

In most of the published literature, the height distribution function and the slope distribution function of random rough surfaces are modeled as the Gaussian function. However, the Gaussian distribution may miss important features of natural surfaces because this function does not allow any abrupt event in the rapidly decreasing tails (Guérin, 2002). Another assumption for the two-dimensional rough surface is that the statistics are independent of the direction, i.e., the surface is isotropic. Nevertheless, the statistics of real surfaces can show some extent of anisotropy (Ward, 1992). Since light scattering is strongly dependent on the surface roughness statistics, it is crucial to understand the true statistics of a rough surface.

3.1 Roughness Parameters and Functions

Many parameters and functions are available to describe the surface roughness quantitatively. The following shows the definition of roughness parameters and functions that will be used in this thesis. Note that these definitions are applicable for the one-dimensional rough surface. Nevertheless, they may be still valid if the two-dimensional rough surface is considered as a combination of line sections.

The surface topography can be represented as the variation of height with displacement along the sampling direction, $z(x)$. The mean surface is determined by

$$\langle z \rangle = \lim_{l \to \infty} \frac{1}{l} \int_0^l z(x)\, dx \tag{3.1}$$

where l is the total sampling length. The arithmetic average roughness R_a is defined by

$$R_a = \lim_{l\to\infty} \frac{1}{l} \int_0^l \left| z(x) - \langle z \rangle \right| dx \tag{3.2}$$

The root-mean-square (rms) roughness σ is defined by

$$\sigma = \sqrt{\lim_{l\to\infty} \frac{1}{l} \int_0^l \left[z(x) - \langle z \rangle \right]^2 dx} \tag{3.3}$$

R_a and σ are the most commonly used roughness parameters. However, they only provide information on the roughness amplitude. The steepness of surface asperities on two surfaces may be very different although R_a or σ can be the same (Stover, 1995). The rms slope ζ_{rms} can tell the steepness of surface asperities. The definition of ζ_{rms} is

$$\zeta_{rms} = \sqrt{\lim_{l\to\infty} \frac{1}{l} \int_0^l \left[\zeta(x) - \langle \zeta \rangle \right]^2 dx} \tag{3.4}$$

where $\zeta(x)$ is the slope (dz/dx) and $\langle \zeta \rangle$ is the mean slope.

The height distribution function is applied to describe the fraction of surface heights from a given height to a small increment. The definition of the slope distribution is very similar to that of the height distribution function. The height distribution function is related to the bearing area ratio in machine science (Thomas, 1999). The two-dimensional slope distribution has been used to describe the orientation of objects on nano/micrometer scales (Inoue et al., 1996; Schleef et al., 1997; Hegeman et al., 1999).

The surface profile can be considered as a summation of many surface roughness components. Each component is the sine (or cosine) wave with regard to the space coordinate, and the period of the wave is defined as the spatial wavelength. The power spectral density (PSD) function can delineate both the vertical and the spatial extent of the surface roughness components. The definition of the PSD function is given as (Stover, 1995)

$$\mathrm{PSD} = \lim_{l\to\infty}\frac{1}{l}\left|\int_0^l z(x)\exp(-i2\pi x f_x)dx\right|^2 \tag{3.5}$$

where f_x is the reciprocal of the spatial wavelength. The autocorrelation function correlates the deviation from the mean value with a translated version by a distance τ (Stover, 1995),

$$\mathrm{ACF}(\tau) = \frac{1}{\sigma^2}\lim_{L\to\infty}\frac{1}{l}\int_0^l \left[z(x)-\langle z\rangle\right]\left[z(x+\tau)-\langle z\rangle\right]dx \tag{3.6}$$

The autocorrelation length is defined as the value of τ when ACF(τ) is equal to $1/e$. The PSD function and the autocorrelation function are a Fourier transform pair. The rms roughness can be determined from the PSD function,

$$\sigma^2 = 2\int_{f_{\min}}^{f_{\max}} \mathrm{PSD}(f_x)df_x \tag{3.7}$$

Since no instruments can capture surface roughness waves from zero frequency to infinite frequency, the integral has to be calculated from the minimum frequency $f_{\min} = 1/l$ to the maximum frequency $f_{\max} = 1/(2d)$, where d is the sampling interval.

3.2 Roughness Measurement and Data Analysis

Several silicon wafers have been studied in this thesis. The surface topography of the rough side of these wafers was characterized using the state-of-art techniques. We used the Digital Instruments NanoScope scanning probe microscope (Multimode and Dimension 3100). The measurements with the AFM were conducted in the contact mode. The optical interferometric microscope (OIM) was also used for complimentary measurements. We measured some samples with the Veeco WYKO optical profiler (NT 1000 and NT 3300). Measurements were taken in the vertically scanning mode.

The surface topographic data is mapped into a data array of size $M \times N$, in the two orthogonal directions, x and y, respectively. First, the mean surface is determined for the data array, and then the rms roughness can be easily calculated. The topographic data in the same row or column in the data array can be treated as one individual scan. The PSD function and the ACF function can be calculated along either the x-direction or the y-direction. The procedure described in the reference (Stover et al., 1998) is followed to calculate the PSD function from the profile data, with the exception that filters and window functions are not implemented in our calculations. There are either M or N line scans in one data array, depending on the direction. The calculated functions are averaged among these line scans.

The height distribution function is produced next. First, the maximum and minimum heights are determined from the topographic data. Then, a finite number of bins with equal interval are assigned and each data point is checked to find the corresponding bin. The number of data points within each bin is divided by the total number of data points to obtain the relative frequency. Finally, the relative frequency is normalized to the probability density function.

The slope distribution function can be produced similarly. Since both the AFM and the OIM measure the surface topography, surface slope has to be estimated from the heights of neighboring points. Figure 3.1 shows the schematic of the nodal network for the slope calculation. The one-dimensional slope can be calculated along different directions with respect to the row direction of the data array. For example, the slope along the x-direction can be calculated from the data in the same row,

$$\zeta(m,n) = z'(m,n) = \frac{z_{m+1,n} - z_{m,n}}{d} \tag{3.8}$$

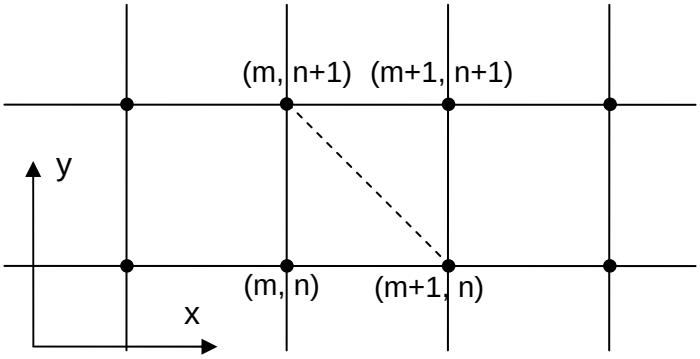

Figure 3.1 Schematic of the nodal network for slope calculation.

The slope can also be evaluated along the diagonal, for instance,

$$\zeta(m,n) = z'(m,n) = \frac{z_{m+1,n+1} - z_{m,n}}{\sqrt{2}d} \tag{3.9}$$

However, if one assumes that four neighboring nodes in the data array form a surface element, then the orientation of the surface element needs to be presented as the two-dimensional slopes in the *x* and *y* directions, $\zeta_x = dz/dx$, $\zeta_y = dz/dy$. The four-node facet may be thought of as two triangular surfaces with a common side (shown as the dashed line in Figure 3.1). The surface normals of the two triangular surfaces can be averaged to give the mean slope of the four-node element such that

$$\zeta_x(m,n) = \frac{z_{m+1,n} - z_{m,n}}{2d} + \frac{z_{m+1,n+1} - z_{m,n+1}}{2d} \tag{3.10a}$$

$$\zeta_y(m,n) = \frac{z_{m,n+1} - z_{m,n}}{2d} + \frac{z_{m+1,n+1} - z_{m+1,n}}{2d} \tag{3.10b}$$

3.3 Roughness Statistics of Silicon Wafers

In order to test the uniformity of surfaces and inspect the effect of the scan area on the measured roughness parameters, we picked up several spots on Samples 1 and 2 and

measured their surface topographies at different scan areas with the AFM and under different magnifications with the OIM. Sample 1 is a phosphorous-doped wafer (525 μm thick) and there is no coating on its backside. Sample 2 has a thermal oxide coating on the backside. The thickness of the coating is 140 nm and the thickness of the wafer is 725 μm.

The measurement results for Samples 1 and 2 are shown in Figure 3.2. The dashed line denotes the averaged rms roughness for the AFM measurements with the same scan area ($Md \times Nd$) and the solid line denotes the averaged rms roughness for the OIM measurements at the same magnification. In Figure 3.2a, from left to right, for each group of data with the same sampling interval, scan sizes for the AFM increase from 5 μm to 40 μm and magnifications for the OIM decrease from 100X to 10X. When the sampling interval is less than 200 nm (scan size 150 μm), the deviation of the rms roughness from the average value ranges from 50 nm to 100 nm. When the sampling interval exceeds 200 nm, the deviation reduces to only 30 nm. The degree of deviation relative to the sampling interval suggests that Sample 1 cannot be statistically analyzed as a uniform surface unless the scan size is greater than 150 μm. For the AFM measurements, the rms roughness σ increases prominently as the scan area is enlarged. Figure 3.2a illustrates that the rate of increase is significant when the scan size increases from 5 μm to 20 μm. Since the number of sampling points is fixed in these scans, the surface wavelength of the measurable roughness component becomes longer as the sampling interval increases. Consequently, the surface frequency of the measurable roughness component becomes lower. Therefore, it can be inferred that the high-frequency roughness components are smoother than the low-frequency roughness

components for this sample in the specific region. When the sampling size approaches 40 μm, the rms roughness is saturated to a limiting value. At the sampling interval of 80 nm, which is close to the maximum interval for the AFM and the minimum interval for the OIM in this measurement, the averaged σ is 460 nm and 610 nm for the AFM and the OIM measurements, respectively. Consequently the relative difference is about 30%.

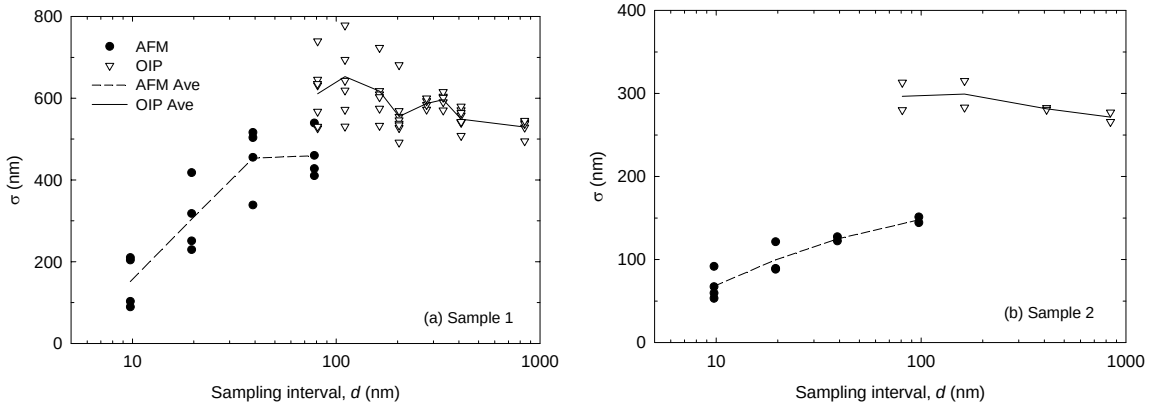

Figure 3.2 Comparison of σ measured with the AFM and the OIM:
(a) Sample 1; (b) Sample 2.
AFM: $M = N = 512$; OIM: $M = 736$, $N = 480$.

In Figure 3.2b, from left to right, scan sizes for the AFM increase from 5 μm to 50 μm, and magnifications for the OIM decrease from 100X to 10X. The deviation of the AFM measurement is less than 20 nm, and the one for the OIM measurement is less than 16 nm. Therefore, Sample 2 is more uniform compared to Sample 1. The averaged σ of the AFM measurement also increases with the scan size for Sample 2. Nevertheless, the rate of increase is smaller. From Figure 3.2b, it is clear that roughness measured with the OIM is much higher than that with AFM. If the sampling interval is set at 100 nm in the AFM, the averaged σ is 148 nm. If the sampling interval is set at 80 nm in the OIM, the

averaged σ is 297 nm. The latter is almost twice as much as the former. This deviation may be attributed to the influence of the reflection from the coating and the substrate on the topography measurement. Further studies may be needed to systematically investigate the dependence of the roughness parameters on the instruments.

The roughness statistics of Samples 3-6 have been systematically characterized. Table 3.1 lists the properties of these wafers. The surface roughness was measured using the AFM in scan areas of 40 × 40 μm^2 and 100 × 100 μm^2. Figure 3.3 shows the surface images of Samples 3-6. There is no obvious difference between the surface images for these samples. It can be seen that there are a lot of microfacets on these surfaces and that the lateral dimension of these microfacets is around a few micrometers.

Table 3.1 Wafer properties of studied samples.

Sample Number	3	4	5	6
Growth Method	FZ[a]	CZ[b]	FZ	CZ
Doping Type	N	P	N	P
Resistivity Range Ω·cm	1500 - 2700	10 - 40	7850 - 9750	4310 - 6970
Thickness, μm	525	500	330	525

a. floating-zone method
b. Czochralski method

Table 3.2 lists the roughness parameters calculated from the topographic data within an area of 100 × 100 μm^2. The listed values are the average values and the standard deviations of three measurements at different positions on each wafer. The rms roughnesses are between 0.51 μm and 0.61 μm, which are comparable to the wavelength

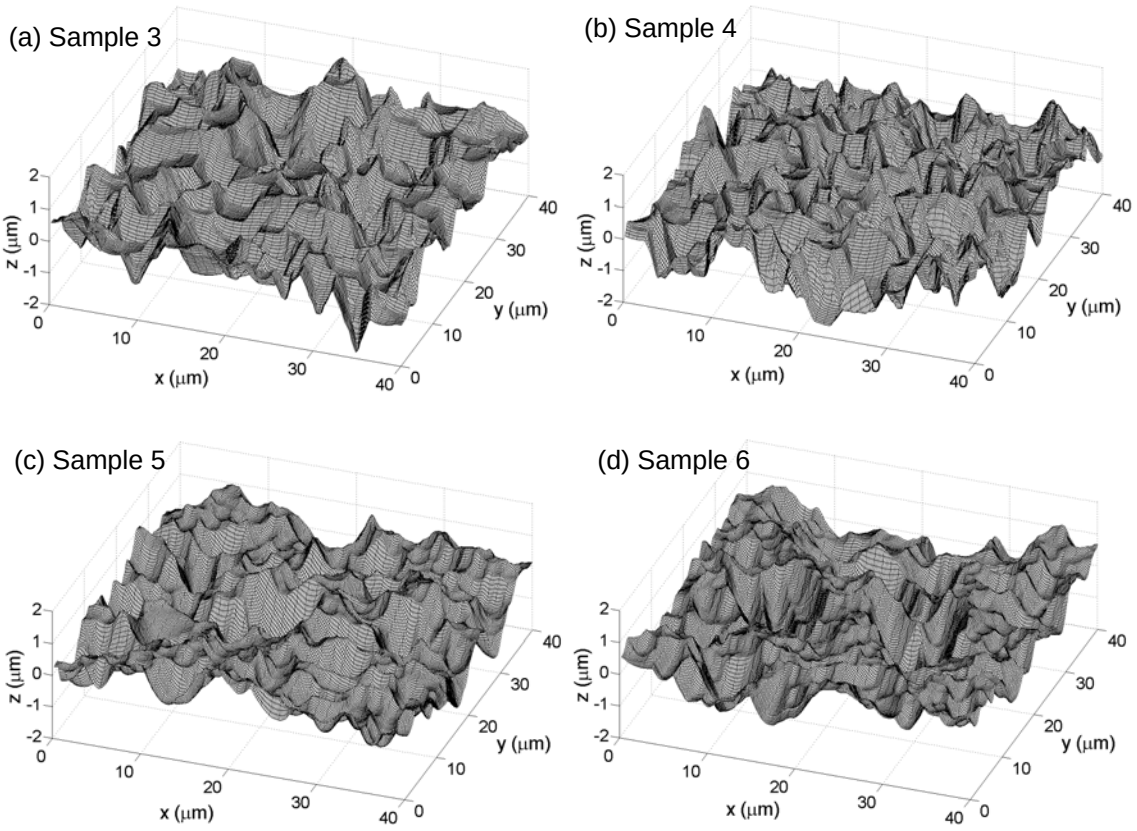

Figure 3.3 AFM surface images:
(a) Sample 3; (b) Sample 4; (c) Sample 5; (d) Sample 6.

of the incident laser beam. Sample 6 is slightly smoother than the rest. The differences in the rms roughnesses for Samples 3, 4, and 5 are within the standard deviation of the measured σ. The slope is calculated along different directions in the measured data array. The rms slope ζ_{rms} averaged along the row and column directions is very close to that averaged along the two diagonals. Therefore, it is insufficient to determine whether or not the surface is isotropic based on the rms slopes. Note that for a surface that follows the Gaussian statistics, $\zeta_{rms} = \sqrt{2}\sigma/\tau$, which is not the case for the measured samples. Among the measured samples, ζ_{rms} of Sample 6 is the smallest while ζ_{rms} of Sample 4 is the largest. The average inclination angle $\tan^{-1}(\zeta_{rms})$ is 15° for Sample 6 and 22° for Sample 4.

Table 3.2 Roughness parameters of studied samples.

Sample Number	3	4	5	6
σ, μm	0.578±0.030	0.608±0.039	0.611±0.021	0.508±0.027
ζ_{rms} (along row/column)	0.334±0.003	0.402±0.011	0.317±0.007	0.260±0.007
ζ_{rms} (along diagonals)	0.326±0.005	0.390±0.009	0.313±0.008	0.255±0.007
τ, μm (along row/column)	3.219±0.282	3.191±0.355	3.845±0.174	4.248±0.683

Figure 3.4 displays the power spectral density function (PSD) and the autocorrelation function (ACF) for Sample 3, calculated from two different scan sizes. The first data point in the PSD plot is not shown. When the surface frequency f_x is higher than 0.05 μm^{-1}, the PSD function calculated from a scan area of 40 × 40 μm^2 is larger than that from a scan area of 100 × 100 μm^2. However, the minimum f_x is 0.02 μm^{-1} for

the scan area of 100 × 100 μm^2. According to Eq. (3.7), the rms roughnesses are 0.579 μm and 0.566 μm, respectively. The relative difference between these values is only 3%. As shown in Figure 3.4b, the difference between the ACFs for different scan sizes is insignificant. The autocorrelation lengths are approximately 3.1 μm for the scan area of 40 × 40 μm^2 and 3.2 μm for the scan area of 100 × 100 μm^2, respectively.

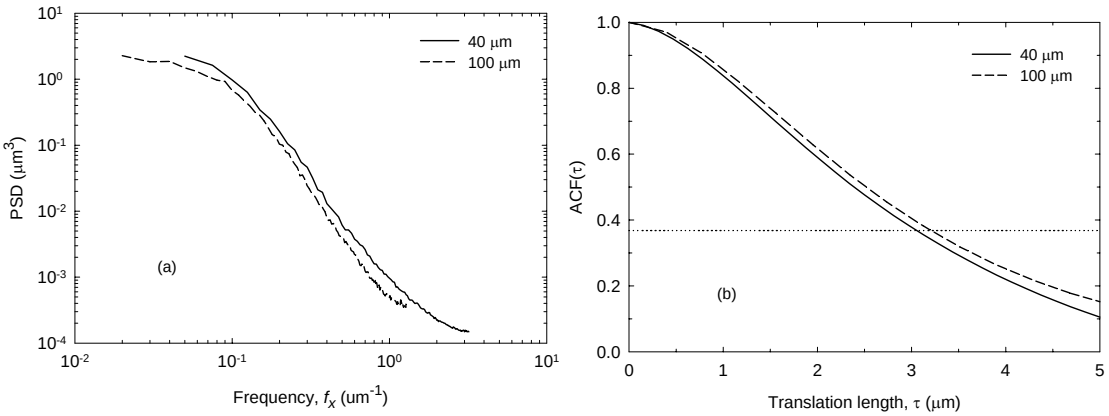

Figure 3.4 PSD (a) and ACF (b) functions for Sample 3.
The dotted line in (b) represents ACF = 1/e.

Figure 3.5 shows histograms of height distribution for Samples 3 and 5. The height distributions for Samples 4 and 6 show the same trend with those in Figure 3.5, and therefore, they are not shown to avoid the redundancy. The height of the mean surface is zero and the area under each curve, i.e., the cumulative probability, is equal to unity. The solid curve represents the height distribution (i.e., probability density) obtained from the topographic data while the dashed curve is the Gaussian function calculated with a standard deviation equal to the rms roughness σ for each sample. Some common deviations exist between the measured distribution and the Gaussian. The most

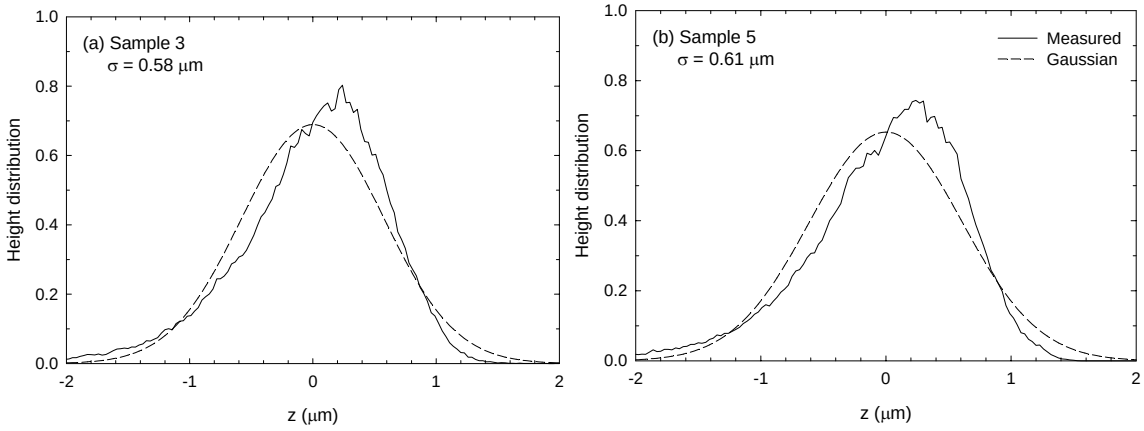

Figure 3.5 Height distribution functions: (a) Sample 3; (b) Sample 5.

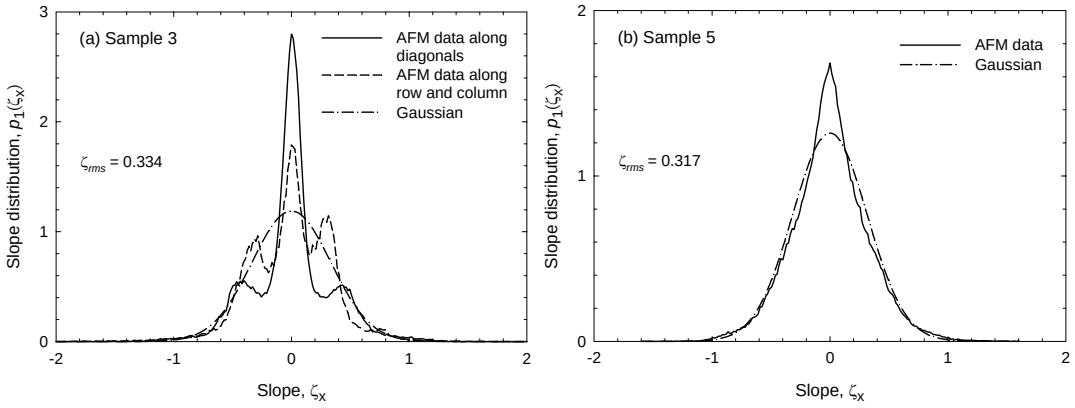

Figure 3.6 1-D slope distributions of Sample 3 (a) and Sample 5 (b).

probable height is shifted towards right from the standard Gaussian function that is symmetric at $z = 0$. The (experimentally obtained) probability density is higher than the Gaussian function for $z < -1.2$, suggesting that there are more deep valleys in the actual surfaces. A crossover occurs within $-1.2 < z < 1.0$, and then the probability density is lower than the Gaussian function until $z \approx 0$. Afterwards, the probability density continues to go up and reaches a maximum around $z = 0.2$ before it goes down and eventually falls below the Gaussian function. According to Bennett and Mattsson (1999), the measured surfaces are said to be negatively skewed with more deep valleys and less high peaks than a perfect Gaussian surface.

Figure 3.6 shows the one-dimensional (1-D) slope distributions for Samples 3 and 5. For Sample 3, the calculation shows that the slope distributions along the row and the column directions are very close to each other, as are the slope distributions along the two diagonals. However, there is significant difference between the former category and the latter category. The slope distributions averaged within each category are plotted in Figure 3.6a, where ζ_x is used in a broad sense to indicate the slope along the specified directions. The solid line represents the average slope distribution over the diagonals and the dashed line represents that over the row and column. The slope distributions show some extent of symmetry about $\zeta_x = 0$ and the mean slope is almost zero. The rms slope of the rough surface is approximately 0.334 for both categories. A Gaussian distribution with a standard deviation of 0.334 is shown as the dash-dot line. Although the height distribution of this rough surface is close to the Gaussian, the measured slope distributions deviate significantly from the Gaussian distribution. The peak at $\zeta_x = 0$ in the diagonal slope distribution (solid line) is much higher than that in the Gaussian.

Furthermore, instead of decreasing monotonically, there are two side peaks at $\zeta_x \approx \pm 0.47$ in the solid line, and the magnitude of these peaks is about one-fourth of that at $\zeta_x = 0$. The slope distribution calculated along the row and column (dashed line) has a lower peak than that calculated along the diagonals, and the side peaks appear at $\zeta_x \approx \pm 0.33$, closer to the center than those in the solid line. On the other hand, the slope distribution functions for Sample 5 are almost the same no matter whether the slope is calculated along the row and column, or along the diagonals. Therefore, they are not distinguished in Figure 3.6b. In addition, some deviation can be observed between the calculated slope distribution and the corresponding Gaussian function.

Figure 3.7 plots the two-dimensional (2-D) slope distributions for the measured surfaces in the ζ_x-ζ_y coordinate system. It can be observed that the slope distribution functions of Samples 3 and 4 are significantly different from those of Samples 5 and 6. The slope distributions for Samples 3 and 4 are clearly anisotropic; however, the slope distributions for Samples 5 and 6 are nearly isotropic. Because the height distribution of Samples 3 and 4 is close to the Gaussian, it is surprising to notice that there are side peaks in the slope distribution. As shown in Figure 3.7a and Figure 3.7b, there are four side peaks located at $|\zeta_x| \approx |\zeta_y| \approx 0.35$ besides the dominant peak located at the center ($\zeta_x = \zeta_y = 0$). The side peaks have similar magnitudes. The magnitude of the side peaks is about one-sixth that of the main peak in Figure 3.7a, and about one-fourth in Figure 3.7b. The side peaks are located symmetrically around the central peak, and the cross-sections passing through the planes of $\zeta_x \pm \zeta_y = 0$ can nearly bisect these side peaks. A ridge along $\zeta_x \approx 0.8$ and another one along $\zeta_y \approx -0.8$ can be observed for some samples. These ridges are independent of the rotation and measurement spot on the sample. Therefore, it is

believed that the ridges are artifacts associated with the geometry of the AFM tip, which is usually a reverse pyramid but may not necessarily be symmetric. If the microfacet has a very large inclination angle, the AFM tip may not touch the surface of the microfacet, and instead, the AFM may image the shape of the tip. Therefore, even though there exist microfacets with slopes $\zeta_x > 0.8$ or $\zeta_y < -0.8$, they will not contribute to the slope distribution. The effect of the ridges in the slope distribution on the predicted BRDF will be discussed in Chapter 5. The slope distribution functions shown in Figure 3.7c and Figure 3.7d are very similar, except that the value at the center is higher in the latter. There is only one dominant peak at the center in the slope distributions. The deviation in the cross-sections of the two-dimensional slope distribution at different azimuthal angles is insignificant.

The features shown in the slope distributions for Samples 3 and 4 can be related to the crystal structure of silicon. In the cross-section of the 2-D slope distributions passing through the planes of $\zeta_x \pm \zeta_y = 0$ and $\zeta_x + \zeta_y = 0$, the side peaks are located at $\zeta_{x'} \approx \pm 0.35\sqrt{2} = \pm 0.50$. If the slope of a microfacet is 0.50, then the corresponding inclination angle is 27°. This implies that there are a number of microfacets that are tilted around 27° with respect to the mean surface. By examining the crystalline structure of silicon, the side peaks should be associated with the {311} planes, since the angles between any of the four {311} planes and the (100) plane is 25.2° (Resnik et al., 2000). The projections of the surface normals of the {311} planes to the (100) plane is in the direction of <011> and the projections are orthogonal, corresponding well to the symmetric features shown in the cross-sections at $\zeta_x \pm \zeta_y = 0$. Therefore, the occurrence of the side peaks may be attributed to the last processing of the rough side of the silicon

wafers. If a smooth single-crystal surface is etched by chemicals, the formed facet should have defined orientations along the crystalline planes. The position of the formed facet can be random or well controlled (Zhao et al., 1996; Resnik et al., 2000). For the rough side of the silicon wafers, usually the wet chemical etching is applied to remove microscopic cracks and surface damages caused by the mechanical processes. Various chemicals such as hydrofluoric, nitric, and acetic acids, and sodium hydroxide are generally used. It is not clear how the slope distribution function would look like before the chemical etching. The "residual" roughness statistics due to the processes such as saw cutting and mechanical lapping/grounding might be random. The chemical etching might have modified some microfacets with a preference to the {311} plane, leaving randomly distributed microfacets with predominant orientations other than the (100) plane (corresponding to $\zeta_x = \zeta_y = 0$). On the other hand, the slope distribution functions for Samples 5 and 6 do not have side peaks. The reason may be attributed to the different processing conditions such as chemical solution, temperature, duration, and so on.

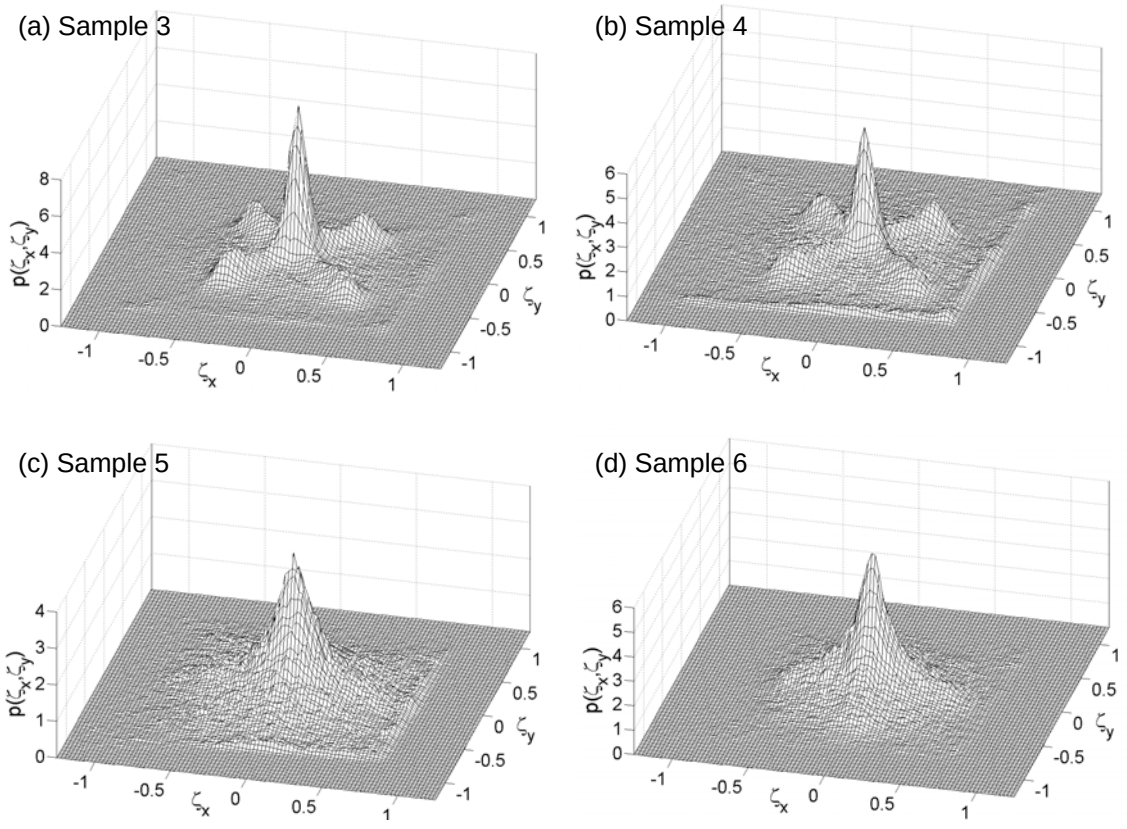

Figure 3.7 2-D slope distribution functions:
(a) Sample 3; (b) Sample 4; (c) Sample 5; (d) Sample 6.

CHAPTER 4

BIDIRECTIONAL REFLECTANCE MEASUREMENTS

4.1 Three Axis Automated Scatterometer

The three axis automated scatterometer (TAAS) was developed by Shen (2002) to measure the bidirectional reflectance distribution function (BRDF) of rough silicon wafers for accurate temperature measurement and control in rapid thermal processing (RTP) and for semiconductor surface metrology. In this thesis, the TAAS is fully characterized again for all the BRDF measurement results shown in the followings.

As shown by Eq. (2.1), the BRDF depends on four angles; therefore, in order to measure both in-plane and out-of-plane BRDFs, the instrument should have four degrees of axis. Nevertheless, if a rough surface is isotropic, the dependence on the two azimuthal angles can be replaced by the difference between them. Consequently, a three-axis scatterometer is sufficient to perform the out-of-plane measurement.

Figure 4.1 shows the experimental setup of the TAAS. The scatterometer consists of three major components: a goniometric table, a light source, and a detection and data acquisition system. The goniometric table and the detection subsystem are controlled by a computer while the light source is controlled manually. Figure 4.2 is a schematic drawing of the rotary stages. Stage 1 (Huber 410) and stage 3 (Huber 420) are coaxial. Their axes are intentionally displaced in Figure 4.2 to emphasize that the rotations of stages 1 and 3 are independent. The point O, where the axis of stage 1 and that of stage2 (Huber 420) meet, is the center point of the scatterometer. The characteristics of the goniometric table can be found in Shen et al. (2003).

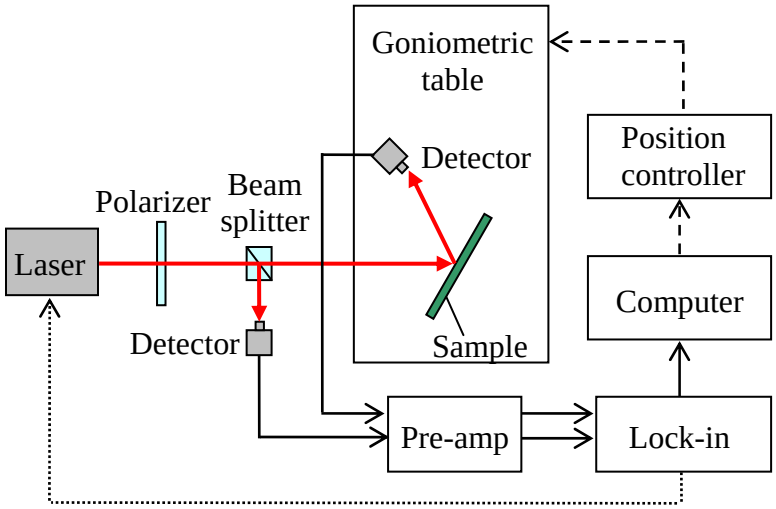

Figure 4.1 Experimental setup of the TAAS.

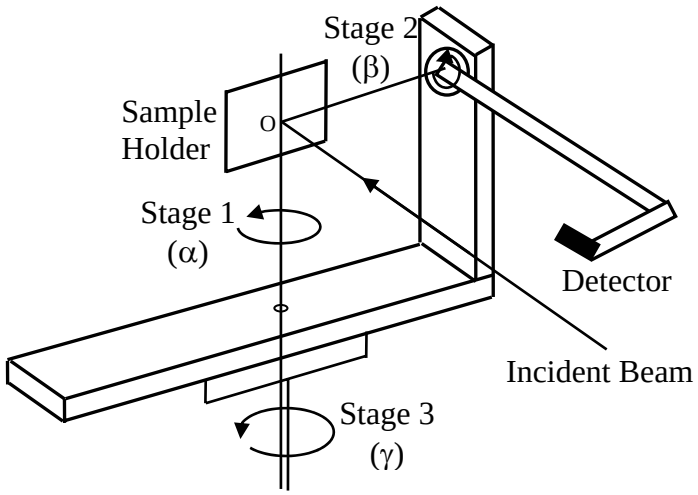

Figure 4.2 Schematic drawing of the rotary stages in the TAAS.
The rotation angles about their axes are denoted by α, β, and γ, respectively.

The light source is stationary in the TAAS; hence, stage 1 varies the incidence polar angle of the sample, which is mounted in a vertically-standing sample holder. The movement of the detector is completed by only two rotary stages (stages 2 and 3), with arm components and balance blocks without complicated parts. The detector can move in the hemisphere above the horizontal plane and in a portion of the hemisphere below the horizontal plane. In order to avoid the collision between the rotary arm and the base of the goniometric table, the position of detector A is limited in the upper hemisphere. A coordinate transformation between the sample system (Figure 2.1) and the stage system (Figure 4.2) is necessary to set the positions of three rotary stages from the incidence and viewing angles, or vice versa (Shen et al., 2003). Due to the thickness of the sample holder frame, an incidence angle up to 88° from the sample normal can be achieved. The polar angle of the reflection ranges from 0° to 88°, and the azimuthal angle ranges from 0° to 180° as long as the detector tube does not block the incident beam. In the plane of incidence the occultation of the light source by the detector tube is approximately ±3°. Due to the sufficient height between the center point O and stage 1, a sample holder for 12-inch wafers can be connected to stage 1. A dial and an *x*-*y* translation stage has been added to the sample holder so that the TAAS can measure an anisotropic surface and scan a surface with difference features (Chen et al., 2004; Zhu and Zhang, 2004).

A compact fiber-coupled diode laser system is used to provide a coherent light source. The maximum output power coming out the fiber is approximately 5 mW. The laser diode controller (Thorlabs LDC500) with a modulation function is operated in the constant-power mode. A thermoelectric temperature controller (Thorlabs LEC2000) provides temperature stabilization, which is crucial to the wavelength stability and the

lifetime of the laser. A 24-hour drift test shows that the root-mean-square fluctuation of the output power is within 0.2%. In this thesis, two diode lasers with wavelengths at 635 nm and 785 nm are used in the BRDF measurement. The spectral width of these lasers is less than 2 nm. The diode lasers can be conveniently interchanged by decoupling the fiber from the collimation lens tube, which is fixed after the alignment is completed. Only nominal effort is needed to realign the source. This gives great convenience especially for aligning the infrared laser. Additional wavelengths can be added using different diode lasers. A monochromator is in process of being built for the broadband spectral measurements. The collimation lens gives a Gaussian beam profile with the $1/e^2$ beam diameter of 5 mm. The beam divergence is less than 0.22 mrad ($\approx 0.0126°$), which meets the ASTM requirement of collimated or slightly converging light source (ASTM, 1997). An aperture next to the collimation lens can vary the beam diameter from 2 to 5 mm. A linear polarizer is used to change the polarization state of the incident beam. The BRDF measurement results are performed for *p*- and *s*-polarizations separately.

Silicon photodiode detectors are selected to cover the spectral ranges 350 - 1100 nm. Two highly linear photodiode detectors of the same type are used. Detector A, contained in a rigid tube mounted in the rotating arm, measures the radiant power reflected by the sample. Detector B monitors the incident power through a cubic beam splitter next to the polarizer. The advantage of using two detectors is to simultaneously measure the incident and the scattered powers so that a slight drift of the laser output power does not affect the measurement result. A precision aperture of 8 mm diameter is set in front of detector A, and the distance D between the beam spot and the detector is 522.5 mm. Consequently, the solid angle $\Delta\omega_r$ of the scatterometer is 1.84×10^{-4} sr and

the half-cone angle θ_{hc} is approximately 0.45°. Two transimpedance preamplifiers with a large dynamic ranging from 10 to 10^9 Ω are used to maintain a near zero bias across the photodiodes. A lock-in amplifier (EG&G 7265DSP) sends an oscillating signal to the laser diode controller so that output signals of two detectors are automatically phase-locked to the internal reference of the lock-in amplifier, thereby eliminates the effect of background radiation in the results. A computer with the LabVIEW environment performs the data acquisition and the automatic rotary-stage control. Since the output signal of the detector is proportional to the received power, the measurement equation is derived as

$$f_r(\theta_i, \phi_i, \theta_r, \phi_r) = \frac{V_A}{C_I V_B} \frac{1}{\cos\theta_r \Delta\omega_r} \tag{4.1}$$

where V_A and V_B are the voltages of the transimpedance amplifiers connected to the movable detector and the reference detector, respectively, and C_I is the instrument constant that depends on the beamsplitter ratio and the detector responsivities. The value of C_I can vary for different polarizations and wavelengths of the sources.

4.2 Characterization of TAAS

The measurement uncertainty is estimated from the law of propagation of uncertainty (Taylor and Kuyatt, 1994; Taylor, 1997)

$$\frac{U_{f_r}}{f_r} = \sqrt{\left(\frac{U_{V_A}}{V_A}\right)^2 + \left(\frac{U_{V_B}}{V_B}\right)^2 + \left(\frac{U_{C_I}}{C_I}\right)^2 + \left(\frac{U_{\Delta\omega_r}}{\Delta\omega_r}\right)^2 + \left(\frac{U_{\theta_r}\sin\theta_r}{\cos\theta_r}\right)^2} \tag{4.2}$$

Table 4.1 lists the uncertainties for each component and the combined uncertainty. The systematic uncertainties of the detectors and amplifiers cancel out when the ratio of

outputs from the two detectors is divided by the instrument constant C_I. The standard deviation of C_I for 60 measurements is 0.03%, due to electronic noise in the data acquisition subsystem. The uncertainty in the solid angle is estimated to be 0.4%. The uncertainty in the reflection angle is less than 0.2°, and therefore, the relative uncertainty related to the reflection angle is 0.4% at θ_r = 45° and 2% at θ_r = 80°, respectively. Hence, the combined uncertainty of the measurement is estimated to be 0.5% at θ_r = 45° and 2% at θ_r = 80°. The main contribution of the uncertainly comes from the uncertainty in the reflection angle; therefore, the alignment is very important to reduce the uncertainty in the measurements. The effect of stray light on the uncertainty is not considered in the uncertainty analysis. Stray light and misalignment may introduce additional uncertainties.

Table 4.1 Components in the combined uncertainty.

Name	Expected value	Uncertainty	Relative uncertainty, %
Distance, D	522.5 mm	1 mm	0.19
Aperture diameter	8 mm	2.54 μm	0.03
Solid angle, $\Delta\omega$	1.84×10^{-4} sr		0.39
Instrument constant, C_I	0.666	0.0002	0.03
$U_{\theta_r} \sin\theta_r / \cos\theta_r$		$U_{\theta_r} = 0.2°$	0.35 at θ_r = 45°
			1.98 at θ_r = 80°
Combined uncertainty			0.5 at θ_r = 45°
			2.0 at θ_r = 80°

The procedure for the alignment is summarized next. A ruler with both horizontal and vertical scales is applied to assist the adjustment. First, the laser beam is adjusted to

be parallel to the optical table. The ruler is positioned right before the laser source, which is located in one end of the optical table. The position of the beam spot on the ruler is recorded. Then the ruler is moved to the other end of the table. With the help of the gridline on the optical table, the ruler can be secured in the same horizontal position as it is before the laser source. If the laser is in the horizontal plane and parallel to the gridline on the optical table, the laser should hit on the same position in the ruler. By adjusting the direction of the laser beam with a kinematic mount, the laser beam can be aligned with an error less than 1 mm along horizontal and vertical axes. Second, the beam must pass through the center point of the system. A pinhole is mounted coaxially with stage 1. The rotary arm is rotated by 180° so that detector A faces the laser beam. The laser beam should hit the center of detector A after it passes through the pinhole. The horizontal and vertical positions of the laser beam can be changed by an *x*-*y* stage with micrometers. The pinhole can be lifted vertically if necessary. The last step of the alignment is completed when the front surface of the sample is normal to the laser beam and meanwhile passes the axis of stage 1.

The polarizer can be calibrated by two methods. In the first method, a calibrated polarizer and a polarization-maintaining fiber are used. The polarization axis can be found when the output of the laser passing through two polarizers in series achieves the maximum or minimum value. The second method explores the Brewster angle for *p*-polarization. The smooth side of a silicon wafer is put in the sample holder. The refractive index of pure silicon is used to calculate the Brewster angle since a very low level of doping has little influence in the refractive index. The incidence angle is set to

the Brewster angle, and the movable detector is rotated to the specular direction. The axis for *p*-polarization can be determined when the output of the detector is minimal.

After the alignment of the scatterometer and the calibration of the polarizer are completed, the instrument constant C_I is measured as the ratio of the outputs of detectors A and B. Detector A is rotated to face the laser beam and any samples in the sample holder should be extracted. C_I is calibrated for both *p*- and *s*-polarizations at the condition that two detectors both are underfilled by the laser beams. Once the instrument constant is obtained, the LabVIEW routine takes over and starts the measurement according to the assigned combinations of incident and receiving angles.

The reflectivity of the smooth side of a silicon wafer was measured by the TAAS at the wavelengths of 635 nm and 785 nm. Figure 4.3 shows the comparisons of the measured reflectivity with the calculated reflectivity using Fresnel's equations. For the prediction, $n = 3.878$ and $\kappa = 0.019$ at $\lambda = 635$ nm and $n = 3.705$ and $\kappa = 0.007$ at $\lambda = 785$ nm are taken from the handbook (Edwards, 1985). The average differences are 1% and 0.5% at $\lambda = 635$ nm for *p*- and *s*-polarizations, respectively. The average differences are 3% and 1% at $\lambda = 785$ nm for *p*- and *s*-polarizations, respectively. The relative difference around the Brewster angle is not included in the average difference because the magnitude of the reflectivity is very small. The larger value of the average difference for *p*-polarization at $\lambda = 785$ is attributed to the imperfection of the polarizer and to the misalignment of the optical axes for both polarizations. The deviation of the optical constants of the sample from the handbook values may also contribute to the deviation. Overall, the relative difference is in the same level as that from the uncertainty analysis.

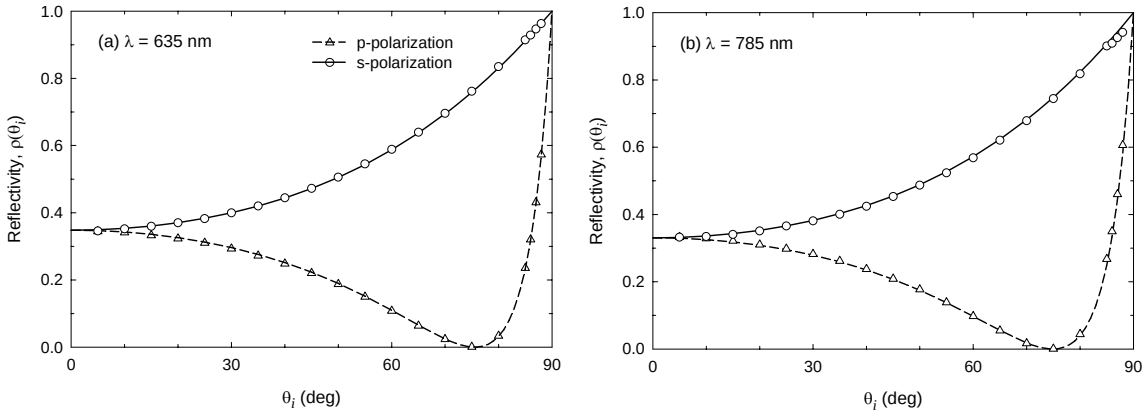

Figure 4.3 Reflectivity of the smooth side of a silicon wafer:
(a) λ = 635 nm; (b) λ = 785 nm.

The TAAS has been characterized by a reference spectral tri-function automated reference reflectometer (STARR) at NIST (Barnes et al., 1998). One silicon wafer in the same batch as Sample 3 was measured using the TAAS and the STARR at the same wavelength, and the average difference between the two instruments for all three incidence angles is approximately 5% including those at the specular direction (Shen et al., 2003). The difference may have been caused by stray light effects since this sample scatters the incident radiation diffusely. Other factors such as the differences in the light sources and the detectors may also affect the comparison of measurement results.

A wafer in the same batch as Sample 5 was repeatedly measured by the TAAS. The measurements were performed right after the RCA cleaning process, after one week, after two weeks, and after three weeks. During that period of time, no realignment was required. Before each measurement, pressurized air was blasted over the wafer to remove any particulates which might rest on the surface. Figure 4.4 displays the average value and the standard deviation for the measured values. Because the term $\cos\theta_r$ in the measurement equation is very small when θ_r gets close to 90°, $f_r\cos\theta_r$ is used as the

vertical axis in the following. The relative standard deviations are around 2% for the measurement at $\theta_i = 0°$, and 1% for the measurement at $\theta_i = 30°$. Therefore, the stability of the TAAS is very good over a period of time of three weeks. It can be inferred that the measurement is very repeatable as long as the surface is free of particulates and contaminants.

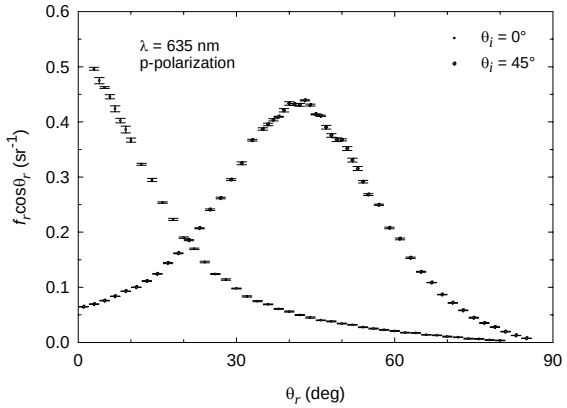

Figure 4.4 Repeatability of measured BRDFs.

CHAPTER 5

BRDF MODELING AND MEASUREMENT FOR SILICON WAFERS

5.1 Unification of Slope Models

Several geometric optics based BRDF models have been reviewed in Chapter 2. Here, a comparison is made to check the consistency and to help develop an appropriate expression for the present study. Some BRDF models may include the contribution from the first-order scattering and the high-order scattering while the other models may only consider the first-order scattering. Therefore, only the contribution due to the first-order scattering is considered in the unification. The shadowing effect is excluded at this moment. If the diffuse term and the geometrical attenuation factor are ignored, the model developed by Torrance and Sparrow (1967) can be written as

$$f_r(\theta_i,\phi_i,\theta_r,\phi_r)=\frac{b\exp(-c^2\alpha^2)}{4\cos\theta_i\cos\theta_r}\rho(n,\kappa,\psi) \tag{5.1}$$

Constants b and c are related to the Gaussian distribution of the inclination angle α and may be determined by fitting the measurement results (Shen et al., 2001).

The in-plane BRDF model based on Kong (1990) and Caron et al. (2003) can be written as follows,

$$f_r(\theta_i,\phi_i,\theta_r,\phi_r)=\frac{p(\zeta_x,\zeta_y)}{4\cos\theta_i\cos\theta_r\cos^4\alpha}\rho(n,\kappa,\psi) \tag{5.2}$$

where $p(\zeta_x, \zeta_y)$ is the joint probability density function of the two-dimensional (2-D) slope distribution. Notice that in writing Eq. (5.2), it is assumed that $\phi_i = 0°$ and $\phi_r = 0°$ or 180°; thus, according to Eq. (2.6) the y-slope ζ_y has to be zero for the in-plane scattering.

When ϕ_i is not zero, Eq. (5.2) can be used after the rotation of the *x-y* coordinate with respect to the *z*-axis.

Tang and Buckius (2001) developed a comprehensive statistical model that deals separately with the first order scattering and the higher order scattering. The BRDF model for the first-order scattering not including the shadowing function is

$$f_r(\theta_i,\phi_i,\theta_r,\phi_r) = \frac{p(\zeta_x,\zeta_y)(1+\zeta_x\tan\theta_i)d\zeta_x d\zeta_y}{\cos\theta_r \sin\theta_r d\theta_r d\phi_r}\rho(n,\kappa,\psi) \tag{5.3}$$

There are two common terms in Eqs. (5.1) - (5.3). One term is related to the slope distribution, and the other is the reflectivity of the microfacet. However, other factors in the formulations are very different although both Eq. (5.2) and Eq. (5.3) incorporate the 2-D slope distribution. In the following, effort will be devoted to the unification of these models for the in-plane BRDF.

The relation between the specular reflection on the microfacet and the orientation of the microfacet is given in Eq. (2.6). The derivatives of ζ_x, ζ_y with respect to θ_r, ϕ_r are

$$\begin{aligned} d\zeta_x &= \frac{-\cos\theta_r\cos\phi_r(\cos\theta_i+\cos\theta_r)+(\sin\theta_i-\sin\theta_r\cos\phi_r)\sin\theta_r}{(\cos\theta_i+\cos\theta_r)^2}d\theta_r \\ &\quad + \frac{\sin\theta_r\sin\phi_r}{(\cos\theta_i+\cos\theta_r)}d\phi_r \\ d\zeta_y &= -\frac{\cos\theta_r(\cos\theta_i+\cos\theta_r)+\sin\theta_r\sin\theta_r}{(\cos\theta_i+\cos\theta_r)^2}\sin\phi_r d\theta_r \\ &\quad - \frac{\sin\theta_r\cos\phi_r}{(\cos\theta_i+\cos\theta_r)}d\phi_r \end{aligned} \tag{5.4}$$

In the plane of incidence ($\phi_r = 0°$), $\sin\phi_r = 0$ and $\cos\phi_r = 0$. The above equatoins can be simplified as

$$d\zeta_x = -\frac{1+\cos(\theta_i+\theta_r)}{(\cos\theta_i+\cos\theta_r)^2}d\theta_r = -\frac{1}{2\cos^2 a}d\theta_r$$

$$d\zeta_y = -\frac{\sin\theta_r}{(\cos\theta_i + \cos\theta_r)} d\phi_r = -\frac{\sin\theta_r}{2\cos a \cos\psi} d\phi_r \tag{5.5}$$

Therefore, the term $d\zeta_x d\zeta_y / d\theta_r d\phi_r$ cancels out for the in-plane scattering,

$$\frac{d\zeta_x d\zeta_y}{\sin\theta_r d\theta_r d\phi_r} = \frac{1}{4\cos\psi\cos^3 a} \tag{5.6}$$

Furthermore,

$$1 + \zeta_x \tan\theta_i = \frac{\cos\psi}{\cos\alpha\cos\theta_i} \tag{5.7}$$

After Eqs. (5.6) and (5.7) are substituted into Eq. (5.3), Eq. (5.3) is shown to be identical to Eq. (5.2).

The distribution with regard to the inclination angle in Eq. (5.1) is not normalized. Nevertheless, the original Torrance-Sparrow model has been improved, and one variant is (Priest and Germer, 2000)

$$f = \frac{1}{2\pi\zeta_{\text{rms}}^2} \frac{1}{4\cos\theta_i \cos\theta_r \cos^4 a} \exp\left(-\frac{\tan^2 a}{2\zeta_{\text{rms}}^2}\right) \rho(n, \kappa, \psi) \tag{5.8}$$

Assume the 2-D slope distribution is Gaussian and isotropic,

$$p(\zeta_x, \zeta_y) = \frac{1}{2\pi\zeta_{\text{rms}}^2} \exp\left(-\frac{\zeta_x^2 + \zeta_y^2}{2\zeta_{\text{rms}}^2}\right) \tag{5.9}$$

For the in-plane scattering, $\zeta_x = \tan\alpha$ and $\zeta_y = 0$; therefore, Eq. (5.8) can also be reformed to an identical formulation as Eq. (5.2). Consequently, it can be concluded that, when multiple scattering is negligible, the BRDF models obtained by different researchers are essentially the same for the in-plane scattering. Therefore, the expression given in Eq. (5.2) is adapted by adding the shadowing functions to address the shadowing and masking effects. The modified BRDF model is given as

$$f_r(\theta_i,\phi_i,\theta_r,\phi_r)=\frac{p(\zeta_x,\zeta_y)}{4\cos\theta_i\cos\theta_r\cos^4\alpha}\rho(n,\kappa,\psi)S(\theta_i)S(\theta_r) \qquad (5.10)$$

Equation (5.10) will be used in this thesis to predict the BRDF from the measured slope distribution $p(\zeta_x,\zeta_y)$.

For light coming from the incidence direction (θ_i, ϕ_i), the reflected intensity at a certain direction (θ_r, ϕ_r) includes contributions from both *p*- and *s*-polarizations. Nevertheless, in the plane of incidence the polarization state will be maintained, and no depolarization will take place. For example, if the polarization of the electric field of the incidence is perpendicular to the plane of incidence (*s*-polarized), the reflected light will also be *s*-polarized. Only microfacets whose surface normal is parallel to the plane of incidence can contribute to the in-plane scattering. The slope along the direction perpendicular to the plane of incidence must equal zero.

The joint probability density function $p(\zeta_x, \zeta_y)$ in Eq. (5.10) is a function of both ζ_x and ζ_y. If the events concerning ζ_x and ζ_y are independent, $p(\zeta_x, \zeta_y) = p_1(\zeta_x) \times p_2(\zeta_y)$, where $p_1(\zeta_x)$ and $p_2(\zeta_y)$ are the marginal probability density functions, which are the one-dimensional (1-D) slope distribution functions along two orthogonal directions (Flury, 1997). To use the 1-D slope distribution, it is assumed that the two functions $p_1(\zeta_x)$ and $p_2(\zeta_y)$ are the same. Since ζ_y has to be zero for the in-plane scattering, the joint probability density function $p(\zeta_x, \zeta_y)$ can be written as $p_1(\zeta_x) \times p_1(0)$. The in-plane BRDF model using the 1-D slope distribution is

$$f_r(\theta_i,\theta_r)=\frac{p_1(\zeta_x)p_1(0)}{4\cos\theta_i\cos\theta_r\cos^4\alpha}\rho(n,\kappa,\psi)S(\theta_i)S(\theta_r) \qquad (5.11)$$

The assumption of independence of ζ_x and ζ_y may be problematic for some surfaces. Therefore, the 2-D slope distribution function will also be applied in the BRDF modeling. Take $\phi_i = 0°$ as an example: the plane of incidence is the $x-z$ plane and the probability of microfacets that contribute to the in-plane scattering is $p(\zeta_x,0)$ with ζ_y = 0. When $\phi_i \neq 0°$, the coordinates (x, y) can be rotated by ϕ_i to (x', y') so that the $x'-z$ plane represents the plane of incidence. The following equations transform the slope distribution from the (ζ_x, ζ_y) coordinates to the $(\zeta_{x'}, \zeta_{y'})$ coordinates:

$$\zeta_{x'} = \zeta_x \cos\phi_i + \zeta_y \sin\phi_i \tag{5.12a}$$

$$\zeta_{y'} = \zeta_y \cos\phi_i - \zeta_x \sin\phi_i \tag{5.12b}$$

After the transformation, $p(\zeta_x,\zeta_y)$ becomes $p(\zeta_{x'},\zeta_{y'})$. $\zeta_{y'}$ is equal to zero when the in-plane BRDF at the incidence azimuthal angle ϕ_i is evaluated. One can consider the probability of surface microfacets that contribute to the in-plane scattering as a cross-section of the 2-D slope distribution with respect to $\zeta_{x'}$. A new function is defined as $p(\zeta_{x'}) = p(\zeta_{x'},\zeta_{y'})$. The in-plane BRDF can be calculated from

$$f_r(\theta_i,\theta_r) = \frac{p(\zeta_{x'})S(\theta_i)S(\theta_r)}{4\cos\theta_i\cos\theta_r\cos^4\alpha}\rho(n,\kappa,\psi) \tag{5.13}$$

The dependence of f_r on the azimuthal angle ϕ_i is implicitly included in $p(\zeta_{x'})$.

5.2 Predicting BRDF Using the 1-D Slope Distribution

The BRDF of silicon wafers is measured at the wavelengths of 635 and 785 nm. The penetration depth is from 3 μm to 9 μm, much smaller than the thickness of the wafer. Therefore, the silicon wafer can be considered as an opaque surface. As shown in

Figure 3.3, the lateral size of the microfacet is about a few micrometers. The data listed in Table 3.2 also show that rms roughness is comparable to the incidence wavelength and the autocorrelation length is a few times larger than the wavelength. Therefore, the geometric optics approximation can be applied. The thickness of the native oxide on the surface is around 1 nm (Tsunoda et al., 2003) so that the influence of the oxide layer on the scattering can be ignored. The silicon wafer is handed free of particles and contaminants. Consequently, light scattering on the wafer surface can be assumed to be caused by surface roughness only.

The ratio of σ/τ ranges from 0.12 to 0.19 for Samples 3-6. For a perfect conducting surface with $\sigma/\tau = 0.2$ at $\theta_i = 30°$, it has been shown that the reflected energy due to multiple scattering is only 2% (Tang and Buckius, 1998). Therefore, the neglecting of multiple scattering in Eq. (5.10) will not cause significant error for the studied surface at most angles. For convenience, an observation angle θ_{obs} is defined as $\theta_{obs} = \theta_r$ when $\phi_r = \phi_i + 180°$, and $\theta_{obs} = -\theta_r$ when $\phi_r = \phi_i$.

Figure 5.1 compares the predicted BRDFs using the 1-D slope distribution with the BRDFs measured at $\lambda = 635$ nm for $\theta_i = 15°$ and 45°. The 1-D slope distribution, shown as the solid line in Figure 3.6a, is calculated along the diagonals from the AFM topographic data over an area of 40×40 μm^2 (Zhu and Zhang, 2004a). The peak in $f_r \cos\theta_r$ is located at the specular reflection direction. The predicted and measured BRDFs at $\theta_i = 15°$ agree well for both *p*- and *s*-polarizations, except for the region around the specular direction, at which the predicted value is 28% lower. At $\theta_i = 45°$, however, the predicted BRDF in the specular direction ($\theta_r = 45°$) is 7% higher than the measured. The discrepancy at the specular direction might be due to the interference effect, not included

in the geometric optics framework. The magnitude of the specular peak is given by $f_r \cos\theta_r \propto p_1^2(0)\rho(n,\kappa,\psi)/\cos\theta_i$, which is only a function of the reflectivity that is dependent on the polarization and the local incidence angle. This explains the high specular peaks at $\theta_i = 45°$ for *s*-polarization as seen in Figure 5.1b.

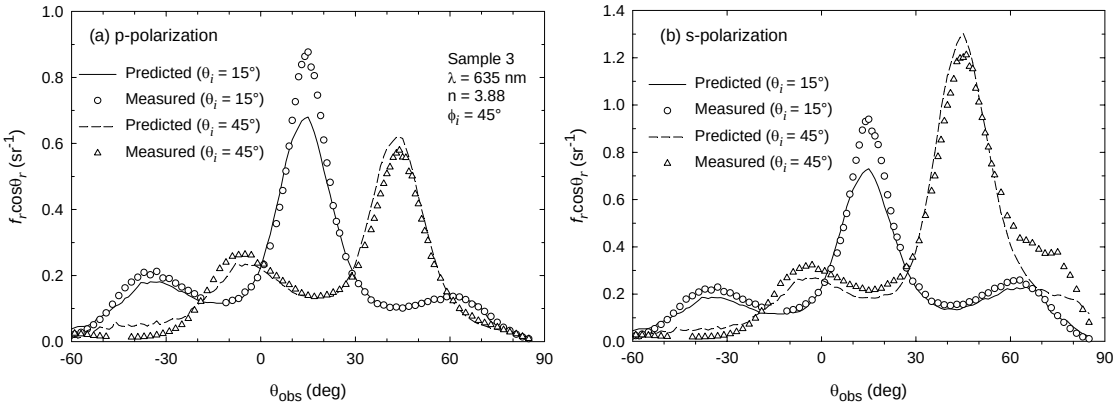

Figure 5.1 Comparisons of measured BRDFs and predicted values using 1-D slope along the diagonals: (a) *p*-polarization; (b) *s*-polarization.

In the BRDF curve at $\theta_i = 15°$, subsidiary peaks can be seen on both sides of the specular direction at $\theta_{obs} \approx -35°$ and 62°. These peaks are not sharp but with a plateau region. The excellent agreement between the measured and predicted BRDFs at the subsidiary peaks suggests that the occurrence of the subsidiary peak in the BRDF is related to the distribution of the microfacet orientation. The side peaks in the slope distribution is at $\zeta \approx 0.47$, which corresponds to $\alpha \approx 25°$. When the incident beam hits a microfacet with an inclination angle $\alpha = 25°$ (in the plane of incidence), the scattering angle will be at $\theta_{obs} = \theta_i \pm 2\alpha$. For $\theta_i = 15°$, the corresponding reflection angles are $\theta_{obs} = -35°$ and 65°, which are close to the angular positions at –35° and 62 in the measured

BRDF. For θ_i = 45°, one of the predicted subsidiary peak is observed at θ_{obs} = –5° in Figure 5.1. The other subsidiary peak at θ_{obs} = 95° is not physical. Nevertheless, it might be expected that $f_r\cos\theta_r$ would increase toward 90° due to the side peak in the slope distribution. However, the situation is more complicated when θ_{obs} is close to 90° since $f_r\cos\theta_r$ is also dependent on the reflectivity of the microfacet. For *p*-polarization, the reflectivity ρ decreases to almost zero at the Brewster angle (Siegel and Howell, 2002), which is approximately 75° for silicon at λ = 635 nm. The local incidence angle ψ is close to 70° when θ_{obs} = 90°. Therefore, both the predicted and measured values of $f_r\cos\theta_r$ decrease monotonically from the specular direction towards 90° as shown in Figure 5.1a.

On the other hand, the reflectivity for *s*-polarization increases with the angle of incidence. However, the masking effect will reduce the scattered radiation towards 90°. Both the predicted and measured values of $f_r\cos\theta_r$ exhibit a shoulder between θ_{obs} = 60° and 90°; however, their magnitudes are quite different. The measured values are much higher than the predicted. Repeated measurements gave the same BRDF when a significant stray light was intentionally introduced or carefully removed during the experiment. Hence, the observed feature is the actual behavior of the surface rather than an instrument artifact. The discrepancy for *s*-polarization may be attributed to multiple scattering, which can be significant at large reflection angles, and the breakdown of Smith's shadowing function at large reflection angles, since the surface statistics is not Gaussian. The local incidence angle ψ, which reflects the incidence at θ_i = 45° to the observation direction of θ_{obs} = 75°, is 60°, and the corresponding reflectivity for the microfacet at *s*-polarization is 0.59. Therefore, the incidence on the microfacet has a high

probability to be reflected and hits other microfacets positioned on the rough surface. This part of incidence can be redirected to directions other than 60° when it leaves the surface. Consequently, the angular distribution can be greatly changed when the local incidence angle ψ is large. The corresponding reflectivity of the microfacet for *p*-polarization is 0.11, much smaller than that for *s*-polarization. Therefore, multiple scattering is not significant in the case of *p*-polarization. Because the multiple scattering is not included in Eq. (5.10), the prediction agrees reasonably with the measurement result within the region of $\theta_{obs} > 60°$ for *p*-polarization; but it is much lower than the measurement results for *s*-polarization.

Although the predicted BRDF using the slope distribution along the diagonals is in good agreement with the measurement at $\phi_i = 45°$, the same cannot be said when the predicted BRDF using the slope distribution along the row and column is compared with the measurement result at $\phi_i = 0°$. This is clearly demonstrated in Figure 5.2, in which the predicted and measured BRDFs at $\phi_i = 0°$ are plotted with $\lambda = 635$ nm and $\theta_i = 0°$. The solid line represents the predicted BRDF using the 1-D slope distribution and has three prominent peaks. On the contrary, the measurement data, represented by the triangular marks, show only one but much higher specular peak. In this case, the BRDF at the specular direction cannot be measured due to the beam blocking. The measured BRDF at $\phi_i = 90°$ is very similar to that measured at $\phi_i = 0°$. It is clear that the 1-D slope distribution calculated along the row and column does not correlate with the measured BRDF along the same directions. Nevertheless, the 2-D slope distribution can be used to obtain a much better matching with the measurement results. This will be discussed in the next session.

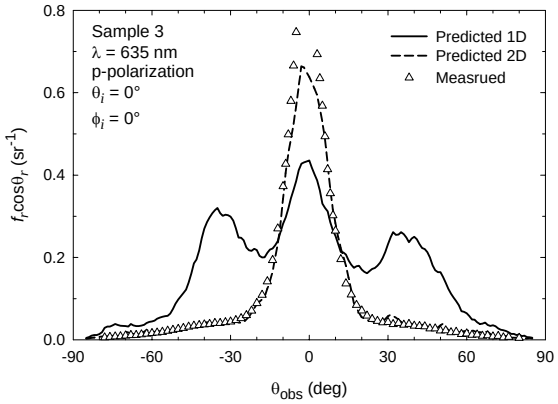

Figure 5.2 Comparisons of measured BRDFs and predicted values using 1-D slope along the row and column.

5.3 Predicting BRDF Using the 2-D Slope Distribution

According to Eq. (5.13), the cross-sections of the 2-D slope distribution are related to the in-plane BRDFs at different azimuthal angles. The cross-section $p(\zeta_x, 0)$ is substituted into Eq. (5.13) to predict the in-plane BRDF at $\phi_i = 0°$ for Sample 3, and this result is represented by the dashed line in Figure 5.2. The prediction agrees well with the measured result except near the specular region. There is no subsidiary peak in the measured BRDF and in the predicted BRDF using the cross-section of the 2-D slope distribution. Hence, the side peaks presented in the slope distribution along the row and column do not correlate with the in-plane BRDF at $\phi_i = 0°$. This can be understood by examining the cross-section of $p(\zeta_x, 0)$ (see Figure 3.7a), which shows no side peak in the *x*-*z* plane with an $\alpha = 18°$ ($\zeta_x = 0.33$, $\zeta_y = 0$). These side peaks in the 1-D slope distribution along the row (or column) are the artifact resulting from the microfacets, whose normal is in the $\zeta_x \pm \zeta_y = 0$ plane with $\alpha = 25°$, as they are projected to the *x*-*z* plane. On the contrary, the predicted BRDF using the cross-section of $\zeta_x \pm \zeta_y = 0$ is very

close to that using the 1-D slope distribution along the diagonals. The reason is that the way in which the 1-D slope is calculated happens to result in the correct distribution, since the normal of most microfacets that contribute to the side peaks is close to the plane $x \pm y = 0$. Therefore, care must be taken in using the 1-D slope distribution to predict the BRDF for anisotropic surfaces.

Further measurements are performed for Sample 3 at several azimuthal angles, and the results are compared to the predicted BRDFs using the corresponding cross-sections of the 2-D slope distribution. The 2-D slope distribution is calculated from the AFM topographic data over an area of $100 \times 100\ \mu m^2$. The comparisons are shown in Figures 5.3 and 5.4. The solid line is the averaged result at $\phi_i = 0°$ and $\phi_i = 90°$. The dashed line is the averaged result at $\phi_i = 45°$ and $\phi_i = 135°$. The dash-dot line is the result at $\phi_i = 30°$. The variation of the predicted BRDF with the azimuthal angle agrees well with that in the measured BRDF. It should be noted that the sampling area to calculate the slope distribution is only $100 \times 100\ \mu m^2$, whereas in the light scattering measurement the beam spot on the sample is near 5 mm in diameter, which might better represent the average behavior of the surface.

Figure 5.3 compares the results at $\theta_i = 0°$ for Sample 3. The BRDF within $|\theta_{obs}| < 3°$ cannot be measured since the detector will block the laser beam in the retroreflection direction. This sample shows a narrow isotropic specular peak around the specular direction within $|\theta_{obs}| < 10°$. The separation of measured BRDFs beyond this region is significant, and two prominent subsidiary peaks can be observed in the curves for $\phi_i = 45°$, corresponding well to the slope distribution in Figure 3.7a. The difference in the BRDFs at different azimuthal angles can be explained by the features in the slope

distribution. There are two prominent side peaks in the cross-section linked to the in-plane BRDF for ϕ_i = 45°. In other words, the probability to find microfacets with the inclination angle of 27° is significant. When a normal incidence hits on these microfacets, the reflected light will be directed to the direction of $|\theta_{obs}|$ = 54°. Consequently, the intensity and thus the BRDF at this direction will be high. Therefore, there are subsidiary peaks in the BRDF curve. The cross-section linked to the in-plane BRDF for ϕ_i = 0° is monotonic. Therefore, there are no subsidiary peaks in the BRDF curve for ϕ_i = 0°. When the plane of incidence is in the position of ϕ_i = 30°, the incidence can see part of the side peaks in the slope distribution. Therefore, the BRDF curve for ϕ_i = 30° is between the curves for ϕ_i = 0° and ϕ_i = 45°.

As shown in Figure 5.3, the subsidiary peaks occurs at $|\theta_{obs}|$ = 50° in the measurement results for ϕ_i = 45°. It can be inferred from the positions of the subsidiary peaks in the measured BRDFs that there are a lot of microfacets with an inclination angle of 25°, which agrees well with the angle between the {311} plane and the (100) plane. However, the angular position for the subsidiary peaks in the prediction is approximately 54°, shifted by a few degrees towards the large observation angle, and the calculated slope distribution shows the angle linked to the side peaks is 27°. The reason for this shift of the side peaks may be related to noise and the convolution of the tip with the surface topography in the AFM measurement. Generally speaking, the agreement between the measured and predicted BRDFs is reasonable in both trend and magnitude. In the region of $|\theta_{obs}| < 10°$, the predicted values are less than the measured values. The relative difference at θ_{obs} = 5° is 8% and 10% for *p*-polarization and *s*-polarization, respectively.

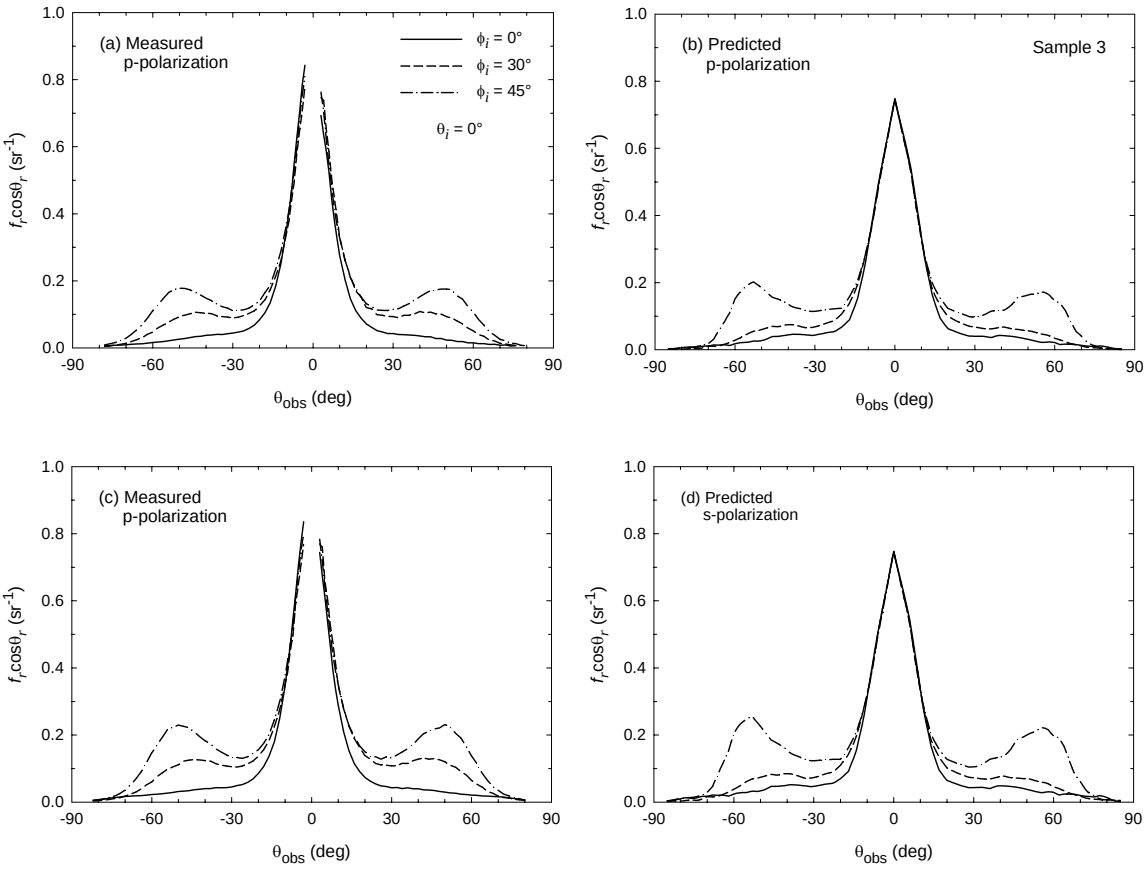

Figure 5.3 Comparison of measured and predicted BRDFs at $\theta_i = 0°$ for Sample 3: (a) and (b): *p*-polarization; (c) and (d): *s*-polarization.

The measured and predicted values at the subsidiary peak are 0.177 and 0.187 for *p*-polarization, respectively. The latter is only 6% higher than the former. Within the anisotropic region where the separation of the BRDFs occurs, the curves for the measurement results at $\phi_i = 30°$ is midway between the curves for $\phi_i = 0°$ and $\phi_i = 45°$. However, in the predicted results the values at $\phi_i = 30°$ is closer to those at $\phi_i = 0°$ than those at $\phi_i = 45°$.

Figure 5.4 presents the comparison of results at $\theta_i = 45°$ for Sample 3. When the incidence is at 45°, the BRDF data within the angular region $-48° < \theta_{obs} < -42°$ cannot be measured because the detector is close to the retroreflection direction. This comparison shows that the predicted results are in good agreement with the measured results. The specular value at $\theta_{obs} = 45°$ is about 22% higher according to the prediction than according to the measurement. There is no separation in the BRDFs at different azimuthal angles within the region $35° < \theta_{obs} < 55°$. The separation of BRDFs in the measured results beyond this region is well repeated in the predicted results. One subsidiary peak can be observed at $\theta_{obs} = -5°$ in the measured BRDF at $\phi_i = 45°$. The same argument to explain the occurrence of the subsidiary peak at $|\theta_{obs}| = 50°$ with the incidence normal to the surface can be applied. If the microfacets are tilted by 27° to the left, the incidence at $\theta_i = 45°$ will be reflected to the direction of $\theta_{obs} = -9°$. One subsidiary peak can be observed at $\theta_{obs} = -8°$ in the predicted BRDF. The predicted value is 22% higher than the measured. It may be anticipated that there exist another subsidiary peak on the right side of the specular peak if the microfacets are tilted 27° to the right. However, since the reflection angle is greater than 90°, this peak is not plausible. Similar conclusions can be drawn for *s*-polarization. Nevertheless, the difference between the

measured BRDFs and the predicted BRDF is obvious at $\theta_{obs} > 60°$ for *s*-polarization, but insignificant for *p*-polarization. The reason may be attributed to the effect of multiple scattering and the breakdown of Smith's shadowing functions.

Another smaller subsidiary peak occurs around $\theta_{obs} = -60°$ in the results with $\phi_i = 45°$. This suggests that there are other side peaks in the slope distribution besides those at $|\zeta_x| \approx |\zeta_y| \approx 0.35$. The microfacets which can direct the incidence at $\theta_i = 45°$ to the direction of $\theta_{obs} = -60°$ should have an inclination angle of 52.5°. Note that the {111} planes are very common if the silicon surface is treated by anisotropic etching. The inclination angle α of a microfacet with a surface in {111} plane is 54.7°. Therefore, it can be inferred that there are some microfacets whose surfaces are close to the {111} planes because of the chemical etching. These microfacets can introduce four side peaks at the positions $|\zeta_x| = 0.92$ and $|\zeta_y| = 0.92$ in the slope distribution. If one looks at the slope distribution of Sample 3 carefully, there are some obscure bumps around $\zeta_x \approx -0.92$ and $\zeta_y \approx 0.92$. However, peaks in other positions are either influenced or totally blocked by the ridges along $\zeta_x \approx 0.8$ and $\zeta_y \approx -0.8$. Since the inclination angle of {111} planes is large, the interaction between the tip and the microfacets may influence the AFM topography measurement significantly. Therefore, the position and magnitude of these bumps in the slope distribution may be not accurate enough. In the predicted BRDF from the slope distribution, the second subsidiary peak is centered on $\theta_{obs} = -58°$. It may be concluded that, the angle-resolved light scattering can have advantages over the AFM topography measurement for the characterization of microfacets with large slopes since the light scattering method is noncontact.

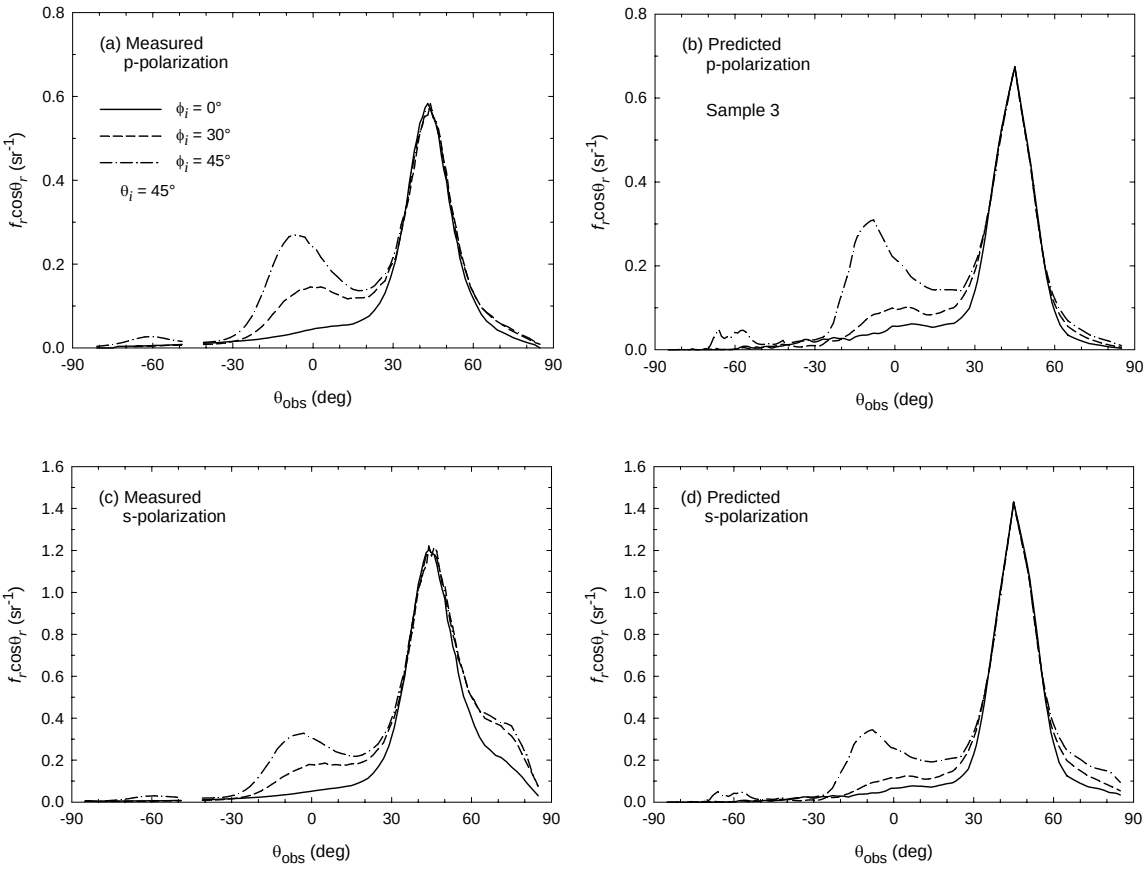

Figure 5.4 Comparison of measured and predicted BRDFs at $\theta_i = 45°$ for Sample 3: (a) and (b): *p*-polarization; (c) and (d): *s*-polarization.

Subsidiary peaks were also observed by Shen et al. (2001) for a different silicon wafer with σ = 0.94 μm and λ = 0.95 μm. The difference between the specular direction and the angular direction where the subsidiary peak occurs is about 50°, which corresponds to an inclination angle α = 25°. This angle is also the angle observed for Sample 3, indicating that the unique peaks in the slope distribution may also exist in other silicon wafers. In order to investigate whether the feature in the slope distribution is a general property, and furthermore, whether a good agreement between the predicted and the measured BRDFs can also be observed, a comprehensive study on the 2-D slope distribution and the BRDF is performed for Samples 4-6 (Zhu and Zhang, 2004b). The predicted BRDFs for Sample 4-6 are based on the slope distribution (See Figure 3.7) calculated from the AFM topography measurement over an area of 100 × 100 μm^2.

Figure 5.5 and Figure 5.6 present the comparisons for Sample 4. Sample 4 shows very similar features as Sample 3, although their properties, such as growth method and doping type, are different. Figure 5.5 shows the comparison for θ_i = 0°. The BRDFs are independent of ϕ_i in the region $|\theta_{obs}| < 10°$. Subsidiary peaks occurs at the angular position $|\theta_{obs}| = 50°$ in the measured BRDF curve for ϕ_i = 45°. Nevertheless, in the predicted BRDF for ϕ_i = 45° the subsidiary peaks shift a few degrees towards the angular position $|\theta_{obs}| = 54°$. In general, the BRDFs of Sample 4 is lower than those of Sample 3 at the same ϕ_i and θ_{obs}. For *p*-polarization, the measured value at θ_{obs} = 5° is 0.372 for Sample 4 and 0.672 for Sample 3. This is due to a higher central peak in the slope distribution of Sample 3. Figure 5.6 presents the comparison of measurement results and predictions for θ_i = 45°. Although the predicted value is much higher than the measured value at a narrow angular region around the specular direction, the agreement between

the measured and predicted BRDFs is reasonably good except for the specular region, excluding the difference at the large observation angle for *s*-polarization discussed previously.

Two prominent subsidiary peaks occur in the results for $\phi_i = 45°$. In the measured result for *p*-polarization, the first subsidiary peak is at $\theta_{obs} = -7°$, with a value of 0.220. The corresponding peak in the prediction is at $\theta_{obs} = -11°$, with a value of 0.232. The second subsidiary peak occurs around $\theta_{obs} = -60°$ in the measured BRDF curve. The corresponding peak is insignificant for Sample 3; however, for Sample 4 the second subsidiary peak becomes more prominent. Since the second subsidiary peak is related to the microfacets with large slopes, this suggests that the probability of microfacets with {111} planes is higher for Sample 4. In the prediction for Sample 4, the second subsidiary peak is centered on $\theta_{obs} = -58°$, displaced by a few degrees from the direction of $\theta_{obs} = -60°$. The magnitude of the peak is lower in the prediction than in the measurement. This may indicate that influence of the tip convolution in the surface topography measurement is important since the inclination angle of {111} is over 50°. In addition, according to Eq. (5.13) a small probability may result in a prominent BRDF value because the term of $\cos^4\alpha$ is also small. For example, the inclination angle for {111} planes is 54.7°, resulting in $\cos^4\alpha = 0.11$. Therefore, the obscure feature in the microfacet orientation may be amplified by the light scattering method. In Figure 5.6, a bump can be observed around $\theta_{obs} = -30°$ in the predicted BRDF for $\phi_i = 0°$. Similarly, as shown in Figure 5.5, a bump also show up around $\theta_{obs} = -75°$ in the predicted BRDF for the same ϕ_i. In both cases, the angular differences between the specular peak and the

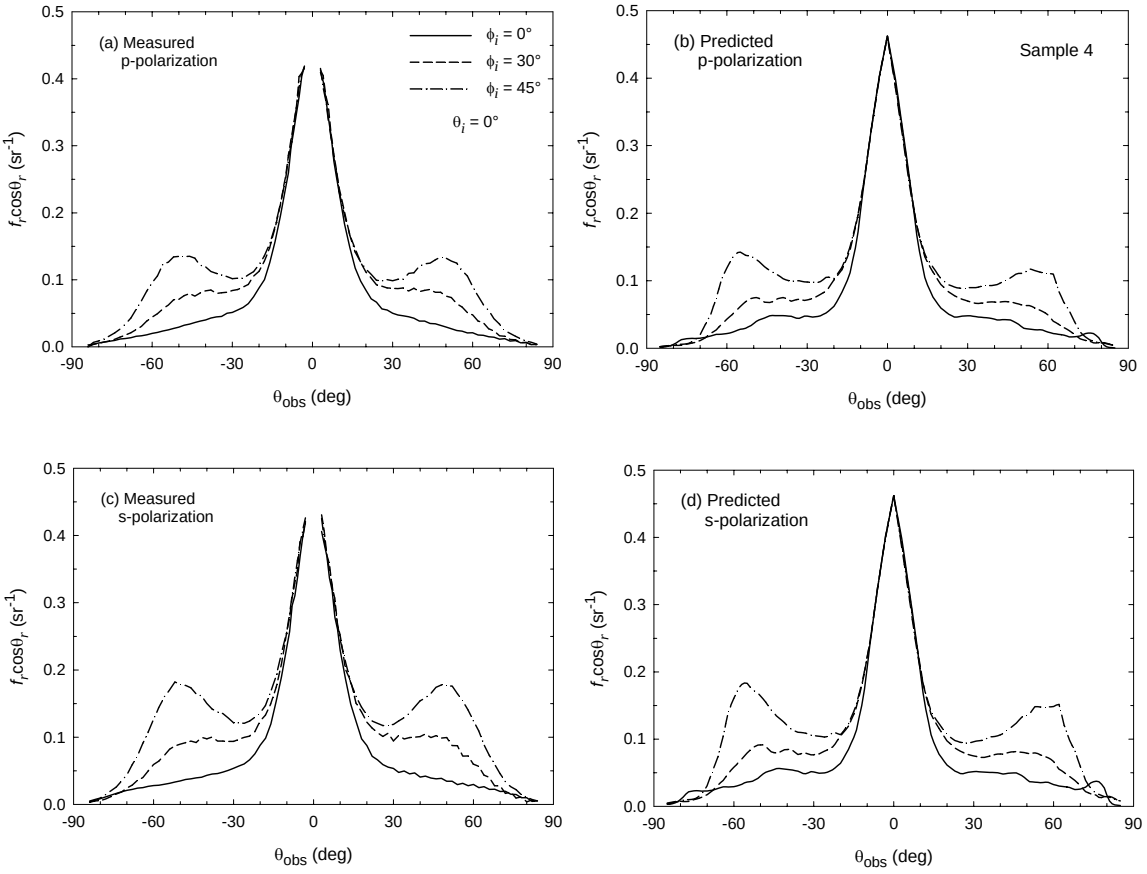

Figure 5.5 Comparison of measured and predicted BRDFs at $\theta_i = 0°$ for Sample 4: (a) and (b): *p*-polarization; (c) and (d): *s*-polarization.

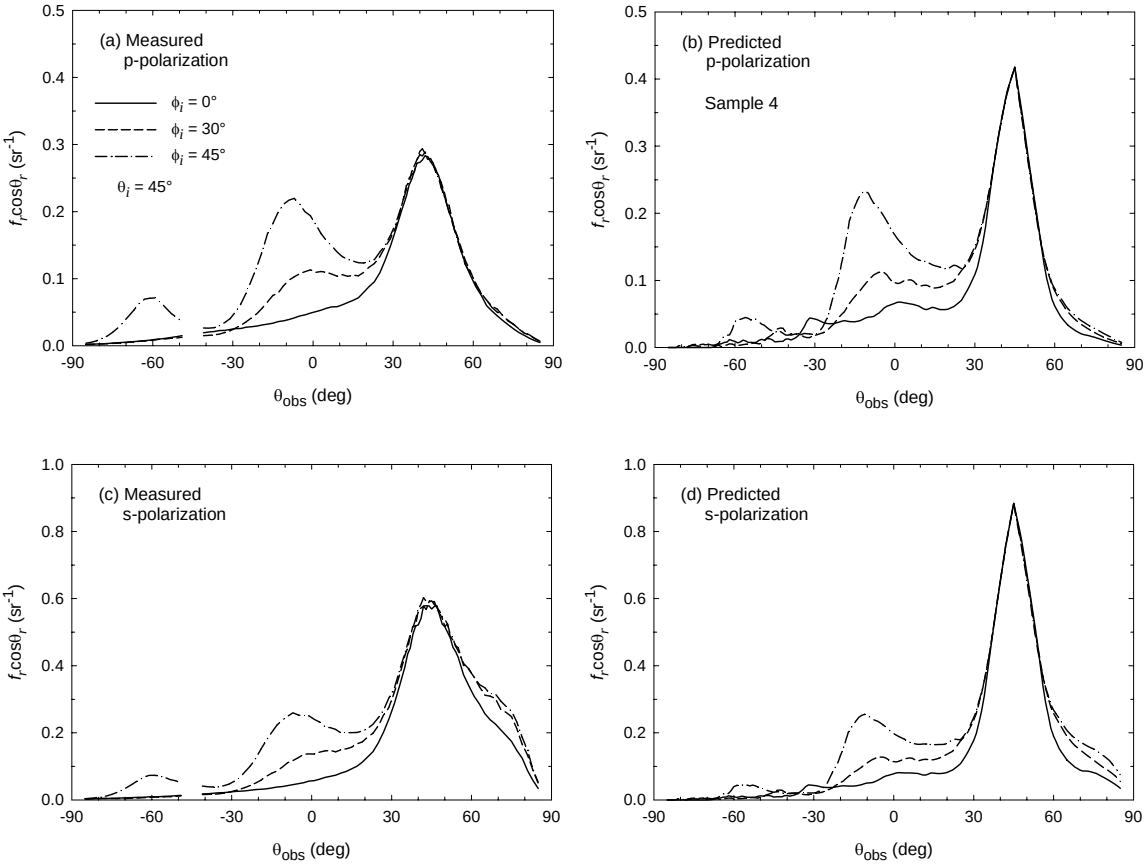

Figure 5.6 Comparison of measured and predicted BRDFs at $\theta_i = 45°$ for Sample 4: (a) and (b): *p*-polarization; (c) and (d): *s*-polarization.

bump are 75°. Therefore, these features are linked to the ridge in the slope distribution at $\zeta_x \approx 0.8$. However, no bumps can be seen in the measured BRDFs. It confirms that the ridges in the slope distribution are artifacts in the topography measurement.

Figure 5.7 compares the measured and predicted BRDFs at $\theta_i = 0°$ for Sample 5. The measured BRDF curve is very symmetric about the specular direction of $\theta_r = 0°$. The BRDF is not dependent on the incidence azimuthal angle in the angular region $|\theta_{obs}| < 24°$ because the slope distribution is nearly isotropic in this region. In addition, a slight separation between the measured BRDF curves can be observed when the observation angle $\theta_{obs} > 24°$. Symmetry of the predicted BRDF curve is also good. The predicted BRDFs agree well with the measured BRDFs. The difference between the maximum and minimum in both groups is close to 0.018 at $\theta_{obs} = 50°$ for *p*-polarization. The measured and predicted BRDFs both show that the value at $\phi_i = 0°$ is the largest in the region $24° < |\theta_{obs}| < 65°$. In addition, it is clearly shown in the measurement results for *s*-polarization that the BRDF at $\phi_i = 45°$ is the highest after $\theta_{obs} > 66°$. This suggests that there are more microfacets with inclination angles larger than 33° along the diagonals than along the row and column directions. Although the measured BRDF within the narrow specular region is not available, the measured BRDF will be higher than the predicted BRDF if the current tendency is also maintained in the specular region. The relative differences are 19% at $\theta_{obs} = 10°$ and 12% at $\theta_{obs} = 20°$ for *p*-polarization.

Figure 5.8 compares the measured and predicted BRDFs at $\theta_i = 45°$ for Sample 5. The measured and predicted BRDFs depends weakly on ϕ_i when $\theta_{obs} > 20°$. The BRDF curve for $\phi_i = 0°$ is the highest in the region $-22° < \theta_{obs} < 20°$ for both *p*- and *s*-

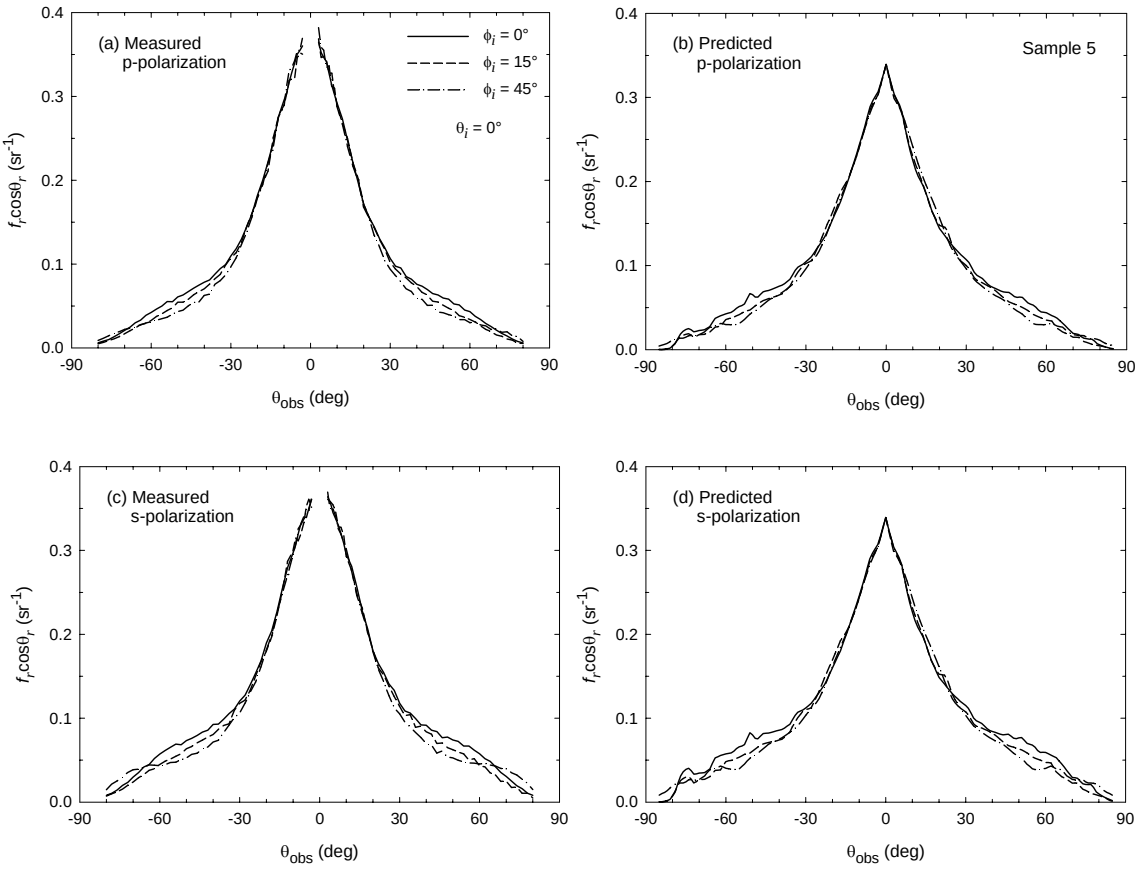

Figure 5.7 Comparison of measured and predicted BRDFs at $\theta_i = 0°$ for Sample 5: (a) and (b): *p*-polarization; (c) and (d): *s*-polarization.

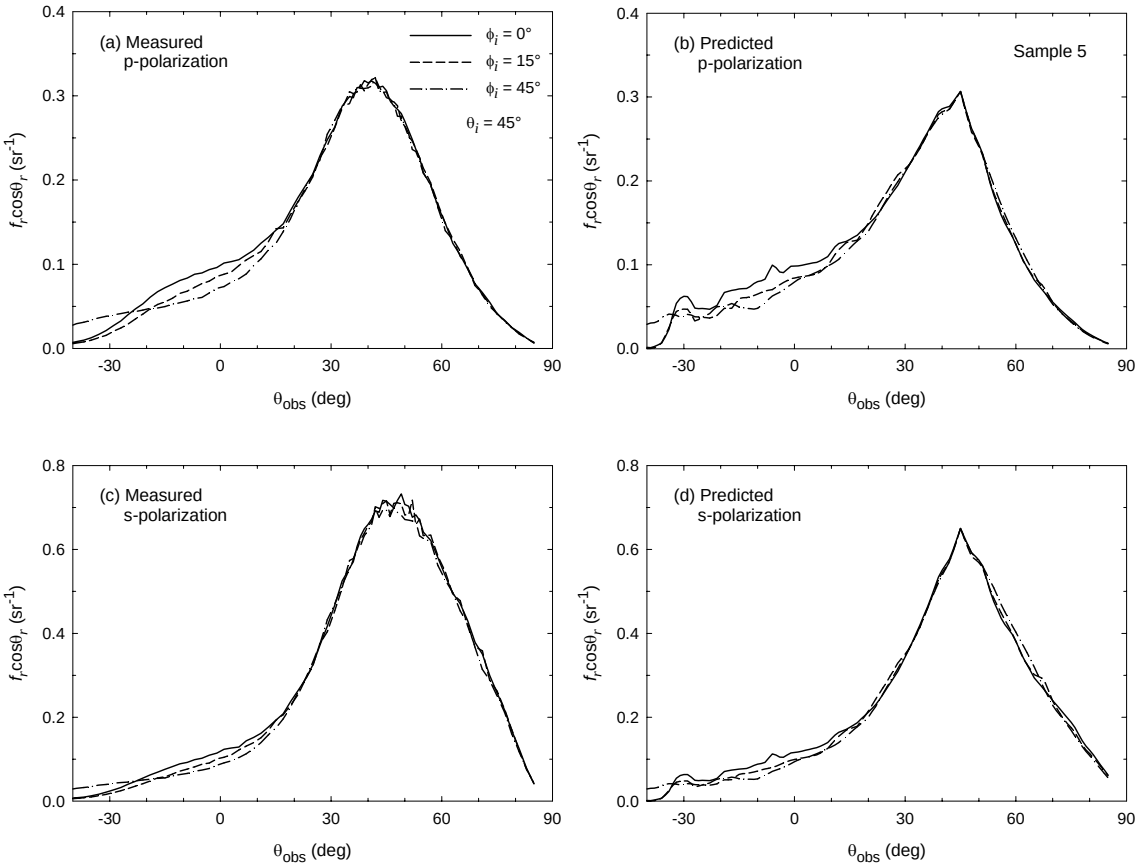

Figure 5.8 Comparison of measured and predicted BRDFs at $\theta_i = 45°$ for Sample 5: (a) and (b): *p*-polarization; (c) and (d): *s*-polarization.

polarizations. When $\theta_{obs} < -22°$, however, the BRDF at $\phi_i = 45°$ is the highest. This is in agreement with the crossover discussed in Figure 5.7 because both transitions happen at an angle around 66° from the specular direction. The agreement between the measured and predicted BRDFs is good in most observation angles. For example, the predicted value at $\theta_{obs} = 45°$ is 0.307 for *p*-polarization, only 1% higher than the measured value. The predicted value at $\theta_{obs} = 45°$ is 0.597 for *s*-polarization, 8% lower than the measured value. However, the shape of the specular peak does not agree very well. The peak in the measured curve has a smooth and flat top despite some small oscillations. However, the peak in the predicted curve is much sharper and narrower. One reason for this disagreement may be attributed to the limitation of the geometric optics model. Although interference effect is not included in the geometric optics modeling, it may influence the angle-resolved light scattering around the specular direction. Another reason is that the slope distribution from the topography measurement might not have been accurate enough. Besides the disagreement at the specular peak, the predicted value is lower than the measured value at large observation angles. The relative differences at $\theta_{obs} = 75°$ are 20% and 31% for *p*-polarization and *s*-polarization, respectively. It may also be related to the difficult in achieving an accurate slope distribution function.

Figure 5.9 and Figure 5.10 present the comparison of the measured and predicted BRDFs for Sample 6. The agreement in the comparison for Sample 6 is very similar to that for Sample 5. The BRDF is independent of ϕ_i within the region of $|\theta_{obs}| < 20°$. However, separation between the BRDFs at different incidence azimuthal angles is more obvious in Sample 6 than in Sample 5. This separation is attributed to the slight anisotropy in the slope distribution when $|\zeta_{x'}| > 0.18$. The agreement between the

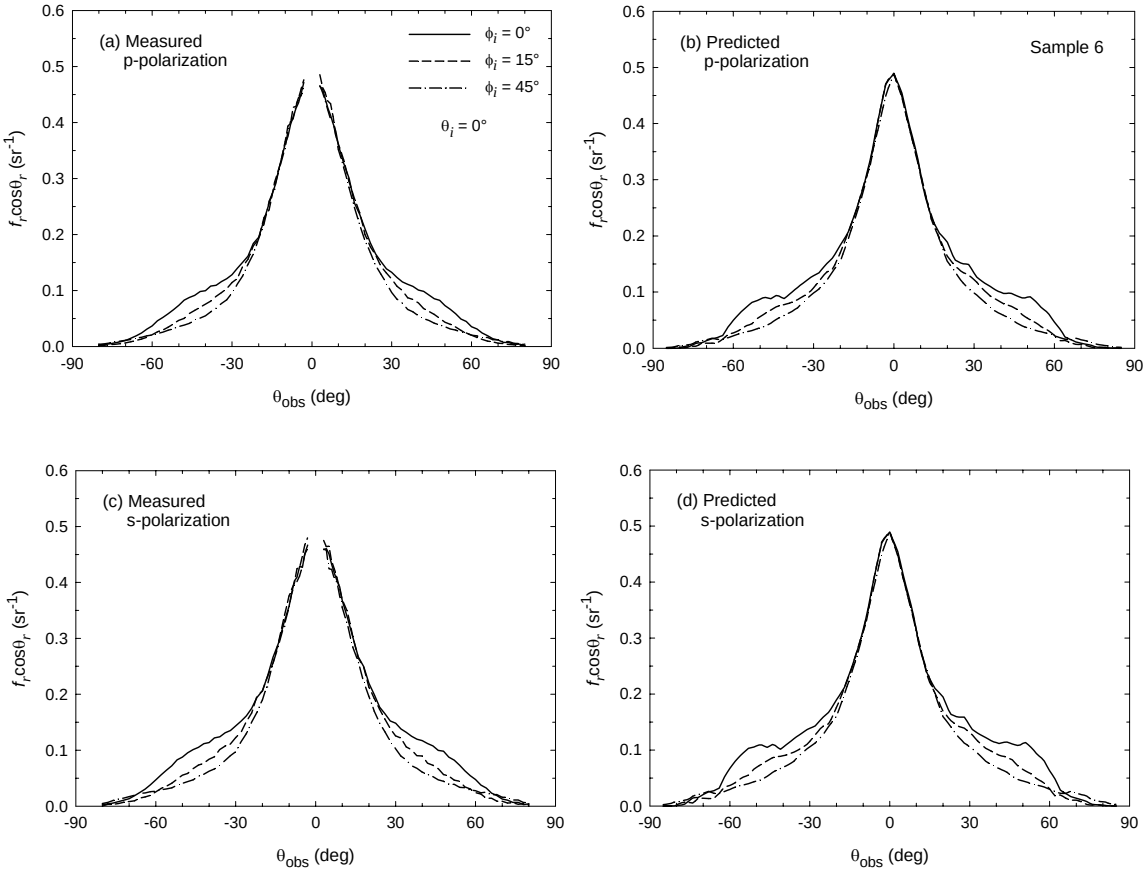

Figure 5.9 Comparison of measured and predicted BRDFs at $\theta_i = 0°$ for Sample 6: (a) and (b): *p*-polarization; (c) and (d): *s*-polarization.

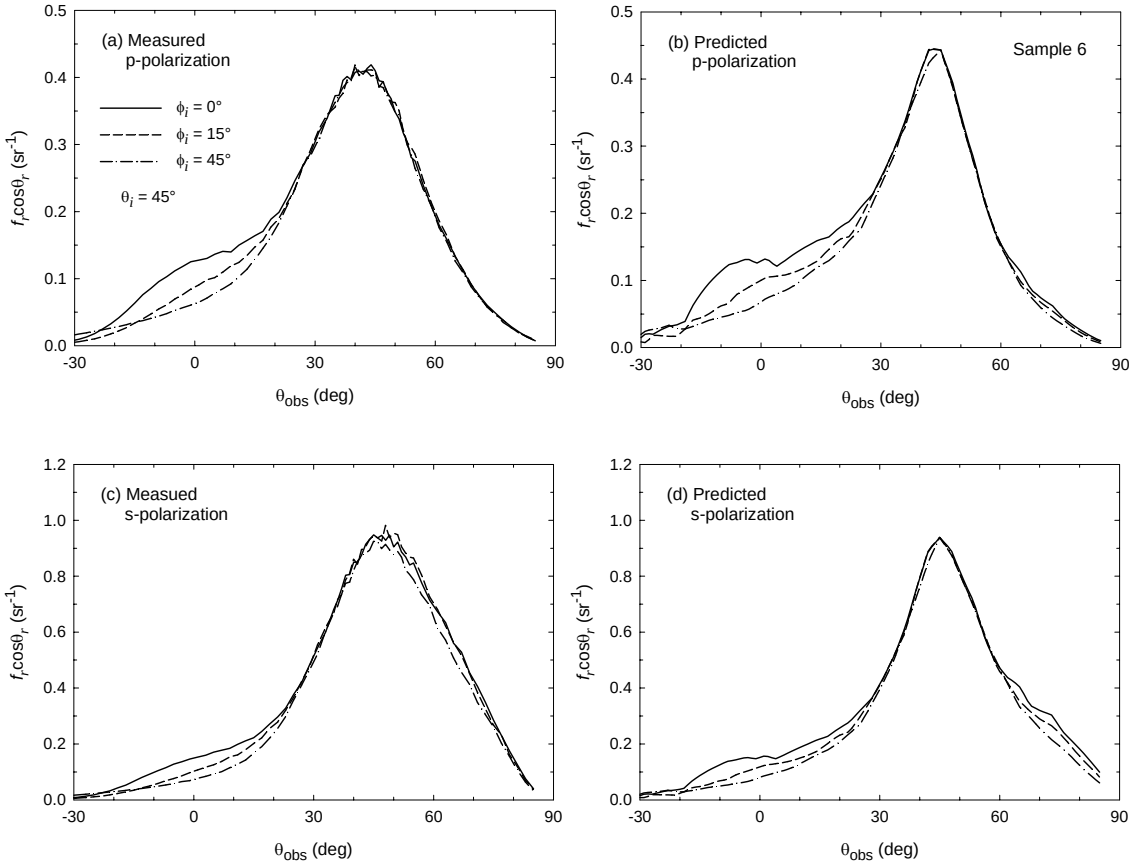

Figure 5.10 Comparison of measured and predicted BRDFs at θ_i = 45° for Sample 6: (a) and (b): *p*-polarization; (c) and (d): *s*-polarization.

measured and predicted BRDFs is very good. The predicted value at $\theta_{obs} = 10°$ is 0.31 for *p*-polarization, about 14% lower than the measured value. The separation in the measured BRDFs is well resolved in the predicted BRDFs, except that the separation is more significant in the predicted BRDFs. For example, at $\theta_{obs} = 50°$ for *p*-polarization, the difference in the measured results is 0.038 while the difference in the predicted results is 0.055. Similar conclusions can be drawn for *s*-polarization. As shown in Figure 5.10, the prediction is also in good agreement with the measurement results for $\theta_i = 45°$. Both the prediction and measurement shows that the BRDF for $\phi_i = 0°$ is the highest in the region $-20° < \theta_{obs} < 25°$. At the specular direction, the predicted value is slightly higher than the measured value. The relative differences are 9% and 1% for *p*-polarization and *s*-polarization, respectively. The peak around the specular direction in the prediction is narrower than in the measurement result.

The measured results shown in Figures 5.1-5.10 are obtained at the wavelength of 635 nm. The BRDF of some samples is also measured at the wavelength of 785 nm. Figure 5.11 compares the measured and the predicted BRDFs at $\lambda = 785$ nm and $\theta_i = 30°$ for Sample 3. The predicted BRDFs show a reasonable agreement with the measured BRDFs. The separation of the BRDFs with the incidence azimuthal angles can be clearly observed. Subsidiary peaks can be seen around $\theta_{obs} = -20°$ in the predicted and measured BRDFs with $\phi_i = 45$. As discussed previously, there is a significant deviation between the measured and the predicted BRDFs at large positive observation angles for *s*-polarization. In addition, there is a shoulder around $\theta_{obs} = 78°$ in the predicted BRDF curve with $\phi_i = 45°$. This shoulder is also caused by the side peaks in the slope distribution. In the measured BRDF curve with $\phi_i = 45°$, there is a subsidiary peak around $\theta_{obs} = 68°$.

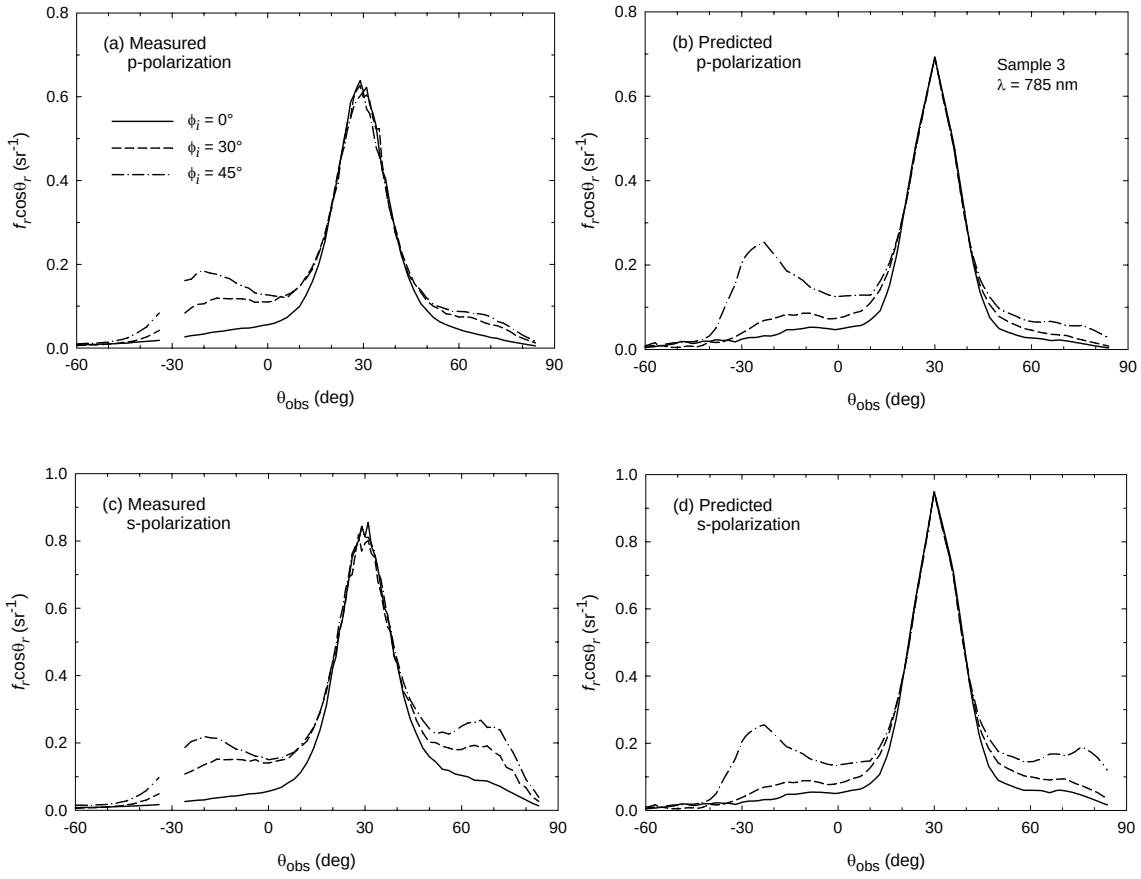

Figure 5.11 BRDFs at near-infrared incidence at $\theta_i = 30°$ for Sample 3:
(a) and (b): *p*-polarization; (c) and (d): *s*-polarization.

To study the effect of wavelength on the BRDF modeling, the BRDFs at $\theta_i = 30°$ and $\phi_i = 45°$ are shown in Figure 5.12 for both $\lambda = 635$ nm and $\lambda = 785$ nm. At $\lambda = 635$ nm, the predicted and measure BRDF peaks are close to each other, while at $\lambda = 785$ nm, the predicted BRDF peak is 13% higher than the measured. According to the geometric optics model, the effect of wavelength is introduced through the reflectivity that depends on the optical constants. The reflectivity for a smooth surface is slightly higher at $\lambda = 635$ nm when the local incidence angle ψ is less than 70°. According to Eq. (5.13), the BRDF in the specular direction should be about 5% higher at $\lambda = 635$ nm than at $\lambda = 785$ nm due to the difference in the refractive index. However, for both polarizations the measured BRDF at $\lambda = 635$ nm around the specular direction is more than 18% higher than that at 785 nm. This suggests that the effect of wavelength requires further investigation and that models based on wave optics may be required to take into account the diffraction effect.

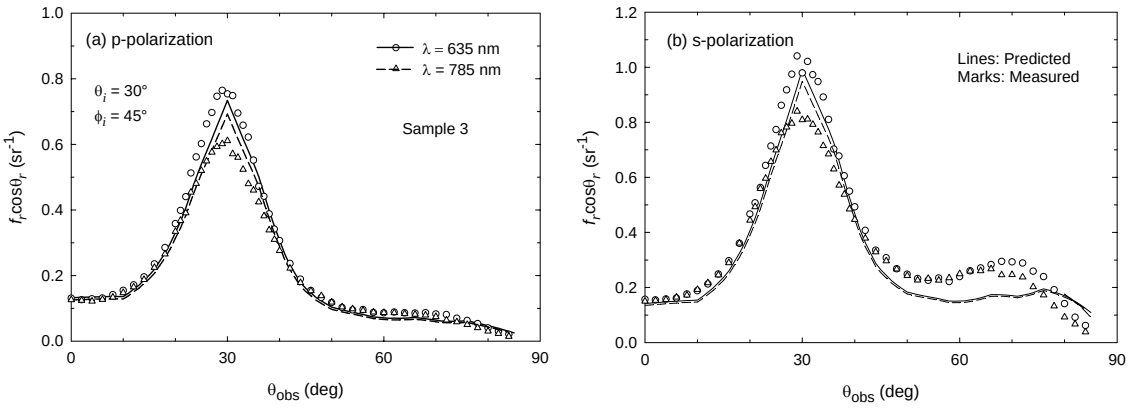

Figure 5.12 Effect of wavelength on BRDF modeling:
(a) *p*-polarization; (b) *s*-polarization.

5.4 Surface Uniformity and Batch Repeatability

The consistency of the BRDF measurements over different positions on one wafer and the repeatability of the BRDF measurements for different wafers in one batch were examined. Four spots in a square of 3×3 cm^2 around the center of the wafer were chosen, and BRDFs for each spot were measured. Figure 5.13 shows the average BRDF and the standard deviation for Samples 3 and 6. The average relative standard deviation for Sample 3 is around 3%. In most of the observation angles, the relative standard deviation is less than 5%. Similar conclusions can be drawn for Sample 6. Therefore, it is clear that the surface is very uniform when a spot size of 3-5 mm diameter is studied. The BRDF measurement result has little dependence on the relative location of the spot on the whole surface.

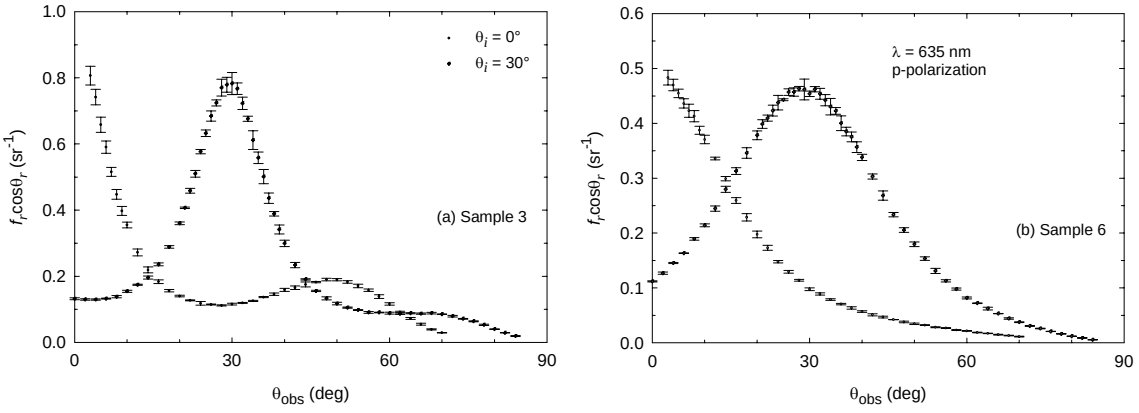

Figure 5.13 Surface uniformity test for Sample 3 (a) and Sample 6 (b).

In order to test whether the silicon wafers manufactured in one batch have good repeatability, two wafers were chosen in the batch and the BRDF measurements were performed for each wafer. Figure 5.14 presents the comparison of BRDF measurement

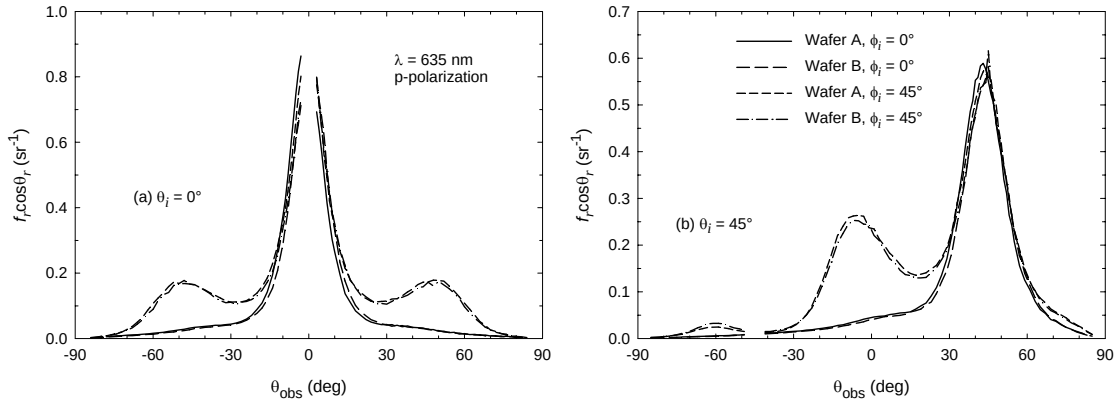

Figure 5.14 Repeatability test for wafers in the same batch as Sample 3: (a) $\theta_i = 0°$; (b) $\theta_i = 45°$.

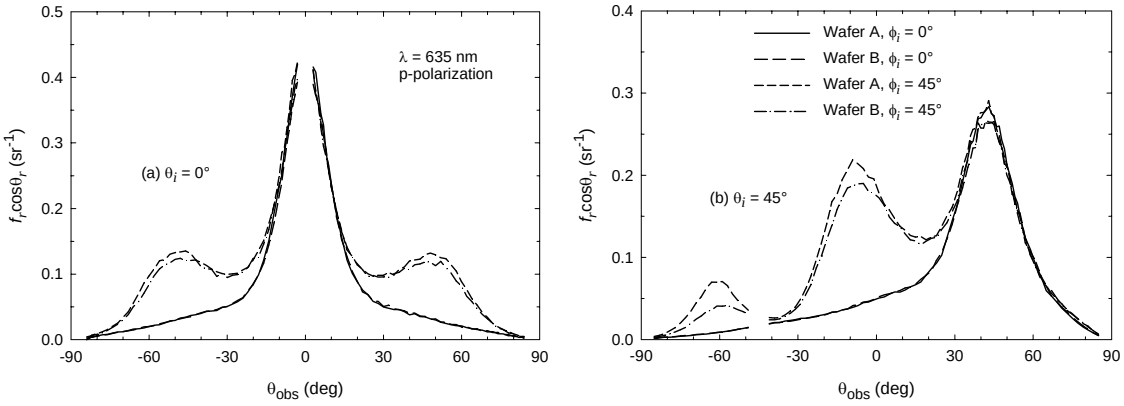

Figure 5.15 Repeatability test for wafers in the same batch as Sample 4: (a) $\theta_i = 0°$; (b) $\theta_i = 45°$.

results for two wafers in the same batch as Sample 3. The measurement results show good agreement at different incidence polar angles and azimuthal angles. A slight deviation can be seen in the subsidiary peaks. Figure 5.15 presents the comparison for two wafers in the same batch as Sample 4. As shown in Figure 5.15a, the agreement between the measurement results is very good at $\theta_i = 0°$. The BRDFs of both wafers show side peaks, except that the wafer A has a slightly higher BRDF at the side peak. The measurement results at $\theta_i = 45°$ are shown in Figure 5.15b. Reasonable agreement can be observed in the BRDFs. Two side peaks occur in the measured BRDF for both wafers. The positions of the side peaks are in the same angular direction. However, the magnitude of the side peak is higher for wafer A than wafer B, consistent with the results shown in Figure 5.15a. Generally speaking, Figure 5.14 and Figure 5.15 demonstrate that wafers in both batches have good repeatability. Therefore, the measured BRDF for one sample may be considered as a representative for all the wafers in the same batch. The side peaks in the measured BRDF is related to the process parameters for these batches.

5.5 Instrument Effects and Reverse Procedure

In the first stage of this thesis, the surface topography of Sample 3 was measured with a scan area of $40 \times 40\ \mu m^2$ with an AFM about two year ago. Figure 5.16 shows the predicted BRDFs from the 2-D slope distribution calculated from that topography measurement (Zhu and Zhang, 2004a). The experimental results are represented by the marks in the figure. The predicted BRDF showed a good agreement with the measured BRDF. First, the magnitudes of the specular peak are very close. Second, the positions and magnitudes of subsidiary peaks agree well with those in the measurement results.

The angular difference between the specular position and the subsidiary peak is 50°, indicating that the subsidiary peak is related to an inclination angle of 25°. However, the results shown in Figures 5.3 and 5.4 imply that the subsidiary peak in the predicted BRDF is linked to an inclination angle of 27°. Therefore, it is necessary to study the reason for the discrepancy.

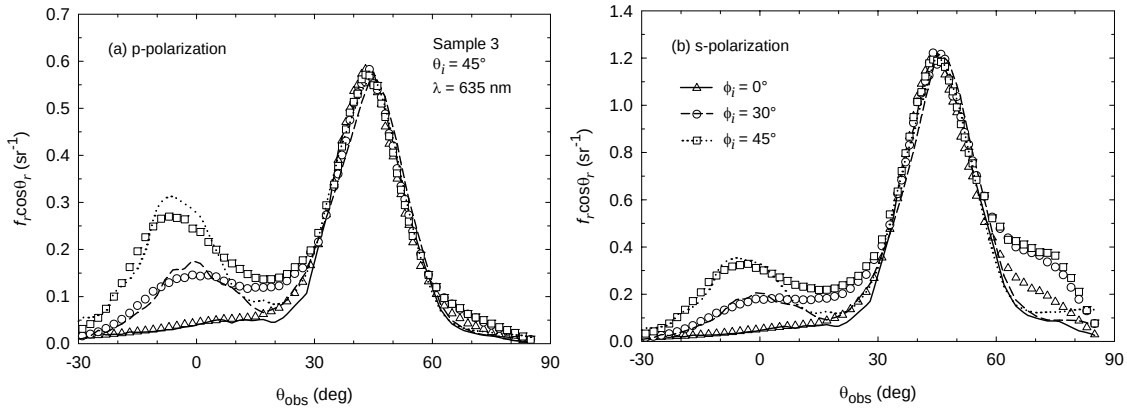

Figure 5.16 Predicted BRDFs using data within an area of 40 × 40 μm^2:
(a) *p*-polarization; (b) *s*-polarization.

The surface topography of Sample 3 has been reexamined using an AFM of the same model (Dimension 3100) at George Institute of Technology. Two scan areas have been imaged, 40 × 40 μm^2 and 100 × 100 μm^2. The cross-sections of the 2-D slope distributions are represented by the dashed line and the dotted line in Figure 5.17. The result from the measurement performed two years ago is represented by the solid line. Among the cross-sections linked to the in-plane scattering at ϕ_i = 0°, the deviation is insignificant, except that the difference around the central peak is obvious. The peak from the 100 μm measurement (dotted line) is slightly higher than that from the 40 μm

measurement (dashed line) even though the surface topographies are measured using the same instrument. This may be due to the dependence of the slope evaluation on the sampling interval.

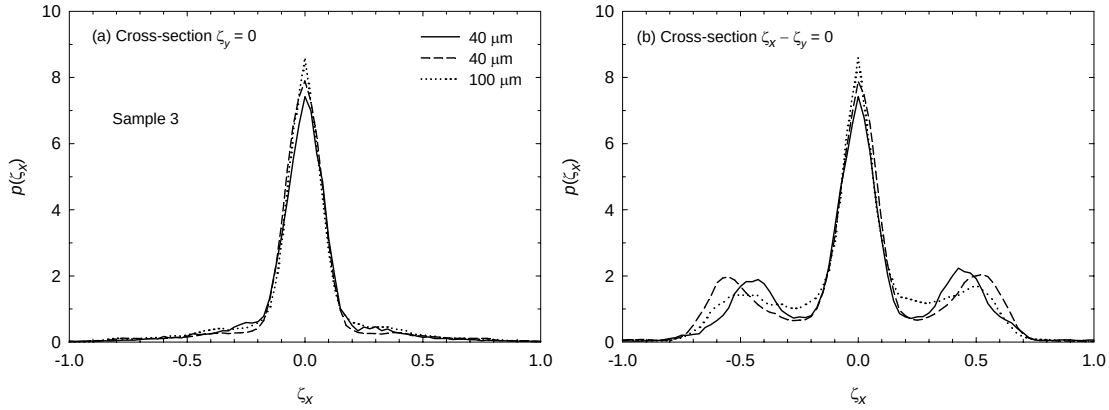

Figure 5.17 Effect of scan area and instrument on the cross-sections: (a) cross-section $\zeta_y = 0$; (b) cross-section $\zeta_x = \zeta_y$.

Figure 5.17b shows the comparison of cross-sections of $\zeta_x - \zeta_y = 0$. Excluding the difference at the central peak, a good agreement can be observed when $|\zeta_x| < 0.15$. However, the deviation among the cross-sections is obvious when $|\zeta_x| > 0.15$, especially in the region around the side peaks. The position and magnitude of the side peaks in the cross-sections are different. The valley around $|\zeta_x| = 0.25$ is lower in the 40 μm measurement than in the 100 μm measurement. This may be also due to the dependence of the slope evaluation on the sampling interval. One reason for the difference between two 40 μm measurements may be the non-uniformity of the surface. It could also be caused by the instrument effect as well because the shape of the AFM probe tips in the two instruments might be not identical. A systematic study may be needed to investigate the optimal scan area and the instrument effect.

Figures 5.1 - 5.17 demonstrate that the agreement between the predicted BRDF and the measured BRDF is reasonable; it is natural to calculate the cross-sections of the 2-D slope distribution from the measured BRDFs through a reverse procedure, and to compare them with those obtained from the AFM surface topography measurement. The cross-sections of the 2D slope distribution is calculated from the measured in-plane BRDFs at corresponding azimuthal angles by

$$p(\zeta_{x'}) = \frac{4\cos\theta_i \cos\theta_r \cos^4\alpha}{\rho(n,\kappa,\psi)S(\theta_i)S(\theta_r)} f_r(\theta_i,\theta_r) \tag{5.14}$$

For the in-place scattering, α and ψ can be easily calculated from θ_i and θ_r. Since Shadowing is significant when the reflection angle is large, Smith's shadowing function should remain in the model. The rms slope is an input of Smith shadowing function; however, its value is unknown until the slope distribution is fully calculated. Some iteration is required in the reverse procedure. In this thesis, the value is simply set to that from the slope distribution obtained from the AFM measurement.

Figure 5.18 displays the comparisons of the cross-sections of 2-D slope distributions for Samples 4 and 5. The central peak is narrower and higher for Sample 4 than for Sample 5. As shown in Figure 5.18a, the difference between the cross-sections is very small when $|\zeta_x| < 0.1$. The agreement between the cross-sections linked to the in-plane BRDF at $\phi_i = 0°$ is satisfactory. The cross-section calculated from the BRDF at $\phi_i = 45°$ shows reasonable agreement with the cross-section of the 2-D slope distribution cut by the plane of $\zeta_x - \zeta_y = 0$. Some deviations are noticeable around the side peaks. Figure 5.18b plots only one cross-section since Sample 5 is nearly isotropic. The agreement is good in the region $|\zeta_x| > 0.26$. The deviation within the region $|\zeta_x| < 0.25$ may be due to

the limitation of the geometrical optics model and the difficulty in obtaining an accurate slope distribution from the topographic data.

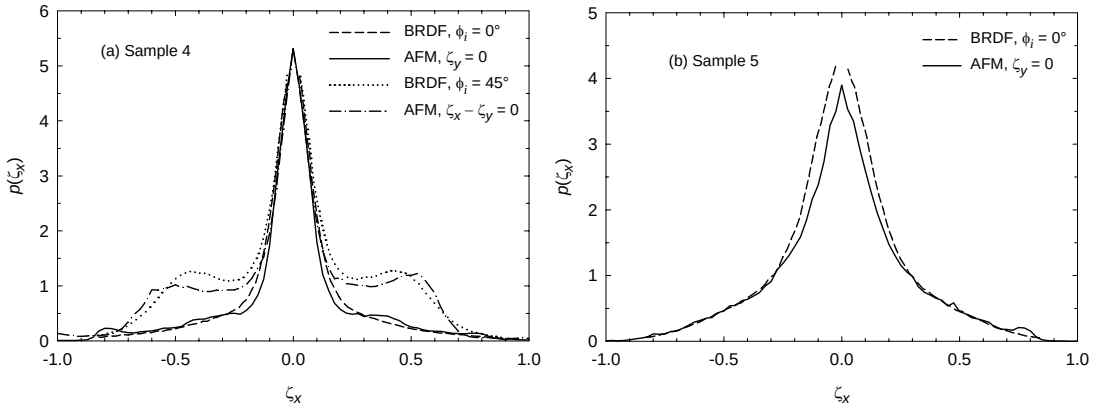

Figure 5.18 Comparison of the cross-sections of the 2-D slope distribution: (a) Sample 4; (b) Sample 5.

5.6 Out-of-plane BRDF and Normal Emissivity

At normal incidence, the out-of-plane BRDF can be written as (Kong, 1990; Caron et al., 2003)

. $$f_{r,a} = \frac{1}{\cos\theta_i \cos\theta_r}\left(\left|r_s(\mathbf{a}\cdot\mathbf{s})\right|^2 + \left|r_p(\mathbf{a}\cdot\mathbf{p})\right|^2\right)\frac{(\mathbf{k}_d\cdot\mathbf{k}_r)^2}{k_{dz}^4}\, p(\zeta_x,\zeta_y) \qquad (5.15)$$

where

$$\mathbf{k}_i = k[\sin\theta_i, 0, -\cos\theta_i]$$

$$\mathbf{k}_r = k[\sin\theta_r\cos\phi_r, \sin\theta_r\sin\phi_r, \cos\theta_r] \qquad (5.16)$$

$$\mathbf{k}_d = \mathbf{k}_i - \mathbf{k}_r = k[\sin\theta_i - \sin\theta_r\cos\phi_r, -\sin\theta_r\sin\phi_r, -\cos\theta_i - \cos\theta_r]$$

$\mathbf{k}_i$ and $\mathbf{k}_r$ are the wave vectors of the incident bam and the reflected beam, respectively, and **a** is the polarization vector for the incidence radiation. **p** and **s** represent the vectors of *p*- and *s*-polarizations with respect to the plane defined by the surface normal and the

wave vector for the reflected wave. The magnitude of the component of the electric field in the direction of **s** is $|r_s(\mathbf{a}\cdot\mathbf{s})|$, and that in the direction of **p** is $|r_p(\mathbf{a}\cdot\mathbf{p})|$. The intensity of the reflected wave should be equal to the summation of the squares of two magnitudes.

The expression in Eq. (5.15) can be simplified at the normal incidence,

$$\frac{(\mathbf{k}_d\cdot\mathbf{k}_r)^2}{k_{dz}^4}=\frac{\left[-k^2(1+\cos\theta_r)\right]^2}{k^4(1+\cos\theta_r)^4}=\frac{1}{(1+\cos\theta_r)^2}=\frac{1}{4\cos^4 a} \tag{5.17}$$

Furthermore, if the vector **a** stands for *p*-polarization with regard to the *x*-*z* plane, then

$$|r_s(\mathbf{a}\cdot\mathbf{s})|^2+|r_p(\mathbf{a}\cdot\mathbf{p})|^2=r_s^2\sin^2\phi_r+r_p^2\cos^2\phi_r \tag{5.18}$$

Therefore, the out-of-plane BRDF at normal incidence for *p*-polarization is

$$f_{r,p}=\frac{1}{4\cos\theta_r\cos^4 a}\left(r_s^2\sin^2\phi_r+r_p^2\cos^2\phi_r\right)p(\zeta_x,\zeta_y) \tag{5.19}$$

Similarly, the out-of-plane BRDF at normal incidence for *s*-polarization is

$$f_{r,s}=\frac{1}{4\cos\theta_r\cos^4 a}\left(r_s^2\cos^2\phi_r+r_p^2\sin^2\phi_r\right)p(\zeta_x,\zeta_y) \tag{5.20}$$

The measured 2-D slope distribution can be substituted into Eqs. (5.19) and (5.20) to predict the out-of-plane BRDF at normal incidence. Furthermore, the predicted BRDFs can be used to calculate the normal-hemispherical reflectance,

$$\rho_{d-h}(0,0)=\int_0^{2\pi}d\phi_r\int_0^{\pi/2}f_r(0,0,\theta_r,\phi_r)\sin\theta_r\cos\theta_r d\theta_r \tag{5.21}$$

As discussed in Sections 5.2 and 5.3, some deviation exists between the predicted and the measured in-plane BRDFs. However, the difference in the BRDFs around the specular peak, due to the interference effect and the inaccurate slope distribution, may be not a problem because of the factor of $\sin\theta_r d\theta_r$. In addition, at normal incidence the effects of masking and multiple scattering on the BRDF are insignificant. For Sample 3, the

normal-hemispherical reflectance is 0.323 at λ = 635 nm for unpolarized incidence while the measured value using an integrating sphere at θ_i = 6° is 0.321. The difference between these two values is very small. Consequently, it may be expected that the spectral normal emissivity can be predicted from the measured slope distribution function. Further studies are needed to investigate the out-of-plane BRDF and the spectral emissivity at different angles and difference wavelengths.

CHAPTER 6

VALIDITY OF HYBRID METHOD FOR COATED ROUGH SURFACES

The hybrid method is computationally effective since its formulation is very similar to that for a rough surface without thin-film coatings. Some agreement has been demonstrated between the modeling results and the experimental measurement (Tang et al., 1999a). It indicates that the hybrid method may be applicable for some rough surfaces. However, there is little knowledge of the validity of the hybrid method in the literature. In this chapter, a rigorous electromagnetic wave solution is used to investigate validity of the hybrid method.

6.1 Hybrid Method

The three-layer system studied in this thesis is illustrated in Figure 6.1. The surface is assumed to be of one-dimensional roughness, and the roughness is invariant in the y-direction. The air-film interface Σ_1 is $z = \xi_1(x)$ whereas the film-substrate interface Σ_2 is $z = -h + \xi_2(x)$. h is the distance between the mean planes of two interfaces, i.e., thickness of the film. Region I, $z > \xi_1(x)$, is the air with a refractive index $n = 1$. Region II, $-h + \xi_2(x) < z < \xi_1(x)$, represents the thin-film coating with a refractive index n_f. Region III, $z < -h + \xi_2(x)$, represents the substrate with a refractive index n_s. One assumption states that the profile of the air-film interface is identical to the film-substrate interface, i.e., $\xi_1(x) = \xi_2(x)$. Although the profiles of two interfaces may have some extent of deviation from the identical profiles, the effect of interface correlation is not the focus of this thesis.

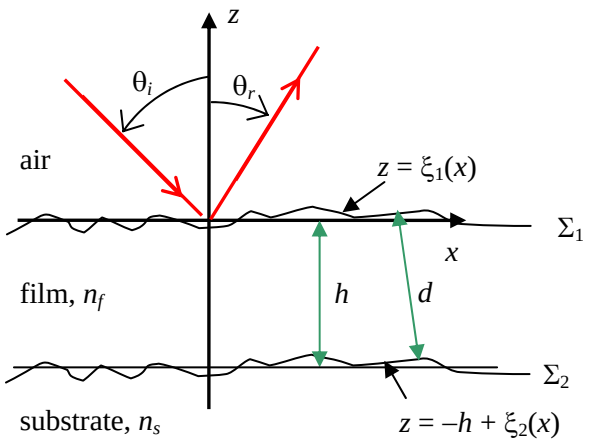

Figure 6.1 Schematic drawing of light scattering on a three-layer system.

Monte Carlo simulation is a powerful method to handle the ray tracing effectively. This method has been successfully applied to simulate the scattering of radiation on opaque surfaces and semi-transparent surfaces (Tang et al., 1997; Tang and Buckius, 1998; Zhou and Zhang, 2003; Lee et al, 2004). Basically, a large number of bundles of rays are illuminated on the rough surface, and each ray is traced until it leaves the rough surface or absorbed by the thin film and the substrate. These bundles can be reflected to different directions by the microfacets on the rough surface. The ratio of the reflected power within a small angular region $\Delta\theta_r$ to the incident power can be determined from the ratio of the number of rays reflected to the small angular region $\Delta N(\theta_r)$ to the number of total bundles illuminated on the rough surface $N(\theta_i)$. The bidirectional reflectance distribution function (BRDF) can be calculated by

$$f_r(\theta_i, \theta_r) = \frac{1}{N(\theta_i)} \frac{\Delta N(\theta_r)}{\cos\theta_r \Delta\theta_r} \tag{6.1}$$

The simulation of scattering by thin-film coated rough surfaces is similar to the procedure for rough surfaces without coatings. The only difference is the way to

determine the reflectivity of the microfacet. For an uncoated rough surface, the reflectivity of the microfacet is calculated from the Fresnel reflection coefficient. However, the interference effect has to be considered for thin-film coated rough surface. The reflectivity of the coated microfacet is (Brewster, 1992; Siegel and Howell, 2002)

$$\rho_f = \left| \frac{r_{0,f} + r_{f,s} \exp(-j2\beta)}{1 + r_{0,f} r_{f,s} \exp(-j2\beta)} \right|^2 \tag{6.2}$$

where $r_{0,f}$ and $r_{f,s}$ are the Fresnel reflection coefficients between the air and the film and between the film and the substrate. The phase shift of wave traveling through the film is

$$\beta = 2\pi n_f d \cos\theta / \lambda \tag{6.3}$$

where θ is the angle between the refracted light and the microfacet normal, and λ is the wavelength in vacuum. Since the microfacet is tilted by an inclination angle of α, a local thickness d should be used, $d = h\cos\alpha$.

In this thesis, two ray-tracing methods, the surface generation method (SGM) (Tang et al., 1997; Tang and Buckius, 1998) and the microfacet slope method (MSM) (Prokhorov and Hanssen, 2003; Zhou and Zhang, 2003; Lee et al, 2004) are used to model the scattering on rough surfaces with coatings. In the SGM, a lot of random rough surfaces with the same statistics are generated using the spectral method (Thorsos, 1988). These rough surfaces have a Gaussian height distribution and a Gaussian autocorrelation function. Although statistics of real surfaces may deviate from the Gaussian, Gaussian statistics are used since the goal of this thesis is to investigate the validity of the hybrid method. For each realization of random rough surface, a large number of bundles of rays are illuminated on the selected nodes on the surface, and each ray is traced. The dimension and orientation of the microfacet related to the surface nodes can be easily

calculated from the surface profile. The BRDFs for each generated surface are calculated, and then the simulation results are averaged to ensure statistically reliable results. On the other hand, in the MSM the rough surface does not have any physical dimension and the surface is represented by a randomly orientated microfacet. The bundles always hit on the same position as if the surface is shrunk to one point. One randomly oriented microfacet is generated for each incoming bundle. The slope distribution of the microfacet is assumed to be a Gaussian distribution whose standard deviation is determined by the root-mean-square roughness σ and the autocorrelation length τ. However, because there is no determined surface, a weight function should be included in the generation of microfacets to consider the ratio of two projected areas of the microfacet (Lee et al., 2004).

The most remarkable difference between the SGM and the MSM lies in the way how the shadowing and the masking are handled. In the SGM, the shadowing and the masking can be fully determined from the known geometry of the generated surface. However, since there is no physical surface in the MSM, the lateral distance between two microfacets is unknown. Therefore, Smith shadowing function is applied in the MSM to handle both the shadowing and the masking (Smith, 1967). The inputs of the Smith shadowing function are the incidence direction (or the reflection direction) and the root-mean-square slope of the rough surface. For given roughness statistics, the shadowing function produces an equal probability of shadowing regardless of the orientation of the generated microfacet due to a fixed incidence angle whereas the probability of masking indeed depends on the orientation of the generated microfacet. Consequently, the shadowing is not accurately addressed in the MSM.

6.2 Rigorous EM-Wave Solution

As shown in Figure 6.1, the surface roughness is invariant in the *y*-direction. Therefore, the electromagnetic field is only a function of *x* and *z*. If the incidence is of *p*-polarization, the magnetic field vector has only *y* component $H(\mathbf{r})$, where $\mathbf{r}$ is defined as (x, z). Only some of the equations governing the light scattering are shown in the following, and more detailed derivation can be found in Gu et al. (1993) and Lu et al. (1998).

The following four equations are derived from Green's theorem and the extinction theorem, depending on the regions where $\mathbf{r}$ and $\mathbf{r}'$ are located. The subscripts 0, *f*, and *s* represent the air, film, and substrate, respectively. If $\mathbf{r} \in$ region I and $\mathbf{r}' \in$ region I,

$$H_0(\mathbf{r}) = H_i(\mathbf{r}) + \frac{1}{4\pi}\int_{\Sigma_1}\left[H_0(\mathbf{r}')\frac{\partial G_0(\mathbf{r},\mathbf{r}')}{\partial n} - G_0(\mathbf{r},\mathbf{r}')\frac{\partial H_0(\mathbf{r}')}{\partial n}\right]d\mathbf{r}' \quad (6.4)$$

If $\mathbf{r} \in$ region I and $\mathbf{r}' \in$ region II,

$$\begin{aligned} 0 = &\frac{1}{4\pi}\int_{\Sigma_1}\left[G_f(\mathbf{r},\mathbf{r}')\frac{\partial H_f(\mathbf{r}')}{\partial n} - H_f(\mathbf{r}')\frac{\partial G_f(\mathbf{r},\mathbf{r}')}{\partial n}\right]d\mathbf{r}' \\ &-\frac{1}{4\pi}\int_{\Sigma_2}\left[G_f(\mathbf{r},\mathbf{r}')\frac{\partial H_f(\mathbf{r}')}{\partial n} - H_f(\mathbf{r}')\frac{\partial G_f(\mathbf{r},\mathbf{r}')}{\partial n}\right]d\mathbf{r}' \end{aligned} \quad (6.5)$$

If $\mathbf{r} \in$ region II and $\mathbf{r}' \in$ region II,

$$\begin{aligned} H_f(\mathbf{r}) = &\frac{1}{4\pi}\int_{\Sigma_1}\left[G_f(\mathbf{r},\mathbf{r}')\frac{\partial H_f(\mathbf{r}')}{\partial n} - H_f(\mathbf{r}')\frac{\partial G_f(\mathbf{r},\mathbf{r}')}{\partial n}\right]d\mathbf{r}' \\ &-\frac{1}{4\pi}\int_{\Sigma_2}\left[G_f(\mathbf{r},\mathbf{r}')\frac{\partial H_f(\mathbf{r}')}{\partial n} - H_f(\mathbf{r}')\frac{\partial G_f(\mathbf{r},\mathbf{r}')}{\partial n}\right]d\mathbf{r}' \end{aligned} \quad (6.6)$$

If $\mathbf{r} \in$ region II and $\mathbf{r}' \in$ region III,

$$0 = \frac{1}{4\pi}\int_{\Sigma_2}\left[G_s(\mathbf{r},\mathbf{r}')\frac{\partial H_s(\mathbf{r}')}{\partial n} - H_s(\mathbf{r}')\frac{\partial G_s(\mathbf{r},\mathbf{r}')}{\partial n}\right]d\mathbf{r}' \tag{6.7}$$

where $H_i(\mathbf{r})$ stands for the incident magnetic field, and $\partial/\partial n$ stands for the normal directive at the boundary. The Green function G is defined as

$$G(\mathbf{r},\mathbf{r}') = j\pi H_0^{(1)}\left(\sqrt{\varepsilon}k_0|\mathbf{r}-\mathbf{r}'|\right) \tag{6.8}$$

where $H_0^{(1)}(\nu)$ is the zeroth-order Hankel function of the first kind with dummy variable ν (Kreyszig, 1993), ε is the relative permittivity of the corresponding medium, and $k_0 = 2\pi/\lambda$ is the magnitude of the wave vector in vacuum.

The boundary conditions at the air-film interface Σ_1 are

$$H_0(\mathbf{r}) = H_f(\mathbf{r}) \tag{6.9a}$$

$$\frac{\partial H_0(\mathbf{r})}{\partial n} = \frac{1}{\varepsilon_f}\frac{\partial H_f(\mathbf{r})}{\partial n} \tag{6.9b}$$

and the boundary conditions at the film-substrate interface Σ_2 are

$$H_f(\mathbf{r}) = H_s(\mathbf{r}) \tag{6.10a}$$

$$\frac{1}{\varepsilon_f}\frac{\partial H_f(\mathbf{r})}{\partial n} = \frac{1}{\varepsilon_s}\frac{\partial H_s(\mathbf{r})}{\partial n} \tag{6.10b}$$

Equations (6.4)-(6.7) are coupled by the boundary conditions. Necessary transformation is required so that the boundary conditions can be substituted. For example, one can set $\mathbf{r} = [x, \xi_1(x)+\delta]$ in Eqs. (6.4) and (6.5), and $\mathbf{r} = [x, -h+\xi_1(x)+\delta]$ in Eqs. (6.6) and (6.7), where δ is a positive infinitesimal. Therefore, only the magnetic fields at the boundaries and their derivatives are involved in the equations. In the numerical simulation, a finite length l has to be truncated from the infinite integral length

and divided into N sections with equal interval $\Delta x = l/N$. The unknowns are the magnetic fields at two boundaries, $H^{(1)}(x_n)$ and $H^{(2)}(x_n)$, and their normal derivatives at the boundaries, $L^{(1)}(x_n)$ and $L^{(2)}(x_n)$, where $x_n = (n - N/2)\Delta x$, $n = 1, \ldots, N$. Accordingly, the integral equations are converted into a matrix equation,

$$\begin{bmatrix} \mathbf{H}_{mn}^{(0)} - \mathbf{I} & \mathbf{L}_{mn}^{(0)} & 0 & 0 \\ \mathbf{H}_{mn}^{(11)} & -\varepsilon_f \mathbf{H}_{mn}^{(11)} & -\mathbf{H}_{mn}^{(12)} & \mathbf{L}_{mn}^{(12)} \\ \mathbf{H}_{mn}^{(21)} & -\varepsilon_f \mathbf{L}_{mn}^{(21)} & \mathbf{I} - \mathbf{H}_{mn}^{(22)} & \mathbf{L}_{mn}^{(22)} \\ 0 & 0 & \mathbf{H}_{mn}^{(s)} & -\left(\varepsilon_s/\varepsilon_f\right)\mathbf{L}_{mn}^{(s)} \end{bmatrix} \begin{bmatrix} \mathbf{H}^{(1)} \\ \mathbf{L}^{(1)} \\ \mathbf{H}^{(2)} \\ \mathbf{L}^{(2)} \end{bmatrix} = \begin{bmatrix} -\mathbf{H}_i^{(1)} \\ 0 \\ 0 \\ 0 \end{bmatrix} \quad (6.11)$$

where $\mathbf{I}$ is the identity matrix with a dimension of N. The expressions for the matrix elements can be found in Gu et al. (1993). Although the Green function becomes singular as $x_m - x_n$ approaches to zero, $\mathbf{H}_{mn}$ and $\mathbf{L}_{mn}$ can be obtained by neglecting the high-order terms in the Green function and its derivative (Maradudin et al, 1990; Tsang et al., 2001). These elements are dependent on the interface profiles, relative permittivities of three media, and the magnitude of the wave vector. Each sub-matrix, $\mathbf{H}_{mn}$ and $\mathbf{L}_{mn}$, has a dimension of $N \times N$. The dimension of the matrix is $4N \times 4N$, and the matrix is not a sparse matrix. The memory requirement and the computation time for solving the matrix equation are formidable if the number of nodes on the rough surface is very large. After the matrix equation has been solved, the reflection amplitude $r(\theta_r)$ can be calculated from the magnetic field and its normal derivative at the boundary Σ_1, $H^{(1)}(x_n)$ and $L^{(1)}(x_n)$ (Maradudin et al, 1990; Sánchez-Gil and Nieto-Vesperinas, 1991),

$$\begin{aligned} r(\theta_r) = \Delta x \sum_{n=1}^{N} & \exp(-ik_0[x_n \sin\theta_r + \xi_1(x_n)\cos\theta_r] \\ & \times \left\{ ik_0\left[\xi_1'(x_n)\sin\theta_r - \cos\theta_r\right] H^{(1)}(x_n) - L^{(1)}(x_n) \right\} \end{aligned} \quad (6.12)$$

The derivation of equations for *s*-polarization is similar to that for *p*-polarization. For *s*-polarization, the magnetic field *H* and its normal derivative *L* in Eqs. (6.11) and (6.12) are replaced by the electric field *E* and its normal derivative *F*, respectively. The matrix elements are independent of polarizations except that factors related to the relative permittivity do not exist in the case of *s*-polarization because the boundary conditions have different forms.

The BRDF for one-dimensional rough surfaces at a plane-wave incidence is (Sánchez-Gil and Nieto-Vesperinas, 1991; Tang and Buckius, 1998)

$$f_r(\theta_i, \theta_r) = \frac{|r(\theta_r)|^2}{8\pi k_0 l \cos\theta_i \cos\theta_r} \tag{6.13}$$

At the edge of the beam, the intensity of the field changes abrupt to zero for the plane-wave incidence. This can introduce so-called edge effect into the simulation results. In order to decrease the edge effect, it is common to use a taped-intensity incidence (Thorsos; 1988; Maradudin et al, 1990; Tsang et al., 2001). The expression of the corresponding BRDF can be found in Maradudin et al. (1990) and Tsang et al. (2001).

6.3 Numerical Implementation and Validity Criteria

A program has been developed to simulate the scattering from rough surfaces, based on the EM-wave approach. The taped-intensity incidence is applied in the program. Figure 6.2 shows the comparisons of the simulation results from the in-house developed computer program with the experimental results or theoretical values. In Figure 6.2a, the simulation result for scattering on a perfect conducting surface is compared to the experimentally measured value from Kim et al (1990). The roughness parameters are σ =

1.2 μm and τ = 2.9 μm. The specular peak around 30° due to the coherent reflection is not shown. The agreement between the simulation results and the measured values are reasonable. The relative difference is around 10% within $-54° < \theta_r < -24°$, and 20% within $36° < \theta_r < 56°$. In order to validate the program for thin-film coated rough surface, the reflectance of a thin silicon dioxide layer on a smooth silicon substrate is obtained from the program. Figure 6.2b compares the result with that calculated from Eq. (6.2). The incidence wavelength is 632 nm, and the refractive indexes for silicon dioxide and silicon are 1.457 and 3.872, respectively (Edwards, 1985). The theoretical solution, which is the solid line in the Figure 6.2b, is the same for *p*- and *s*-polarizations at the normal incidence. For the numerical simulation, $l = 40\lambda$, $N = 800$. It can be observed that the simulation results show excellent agreement with the theoretical solution. The average relative error for *p*-polarization is less than 3%, and that for *s*-polarization is about 1%. Therefore, the numerical error introduced by the finite integral length and finite number of surface nodes is assumed to be around 3%.

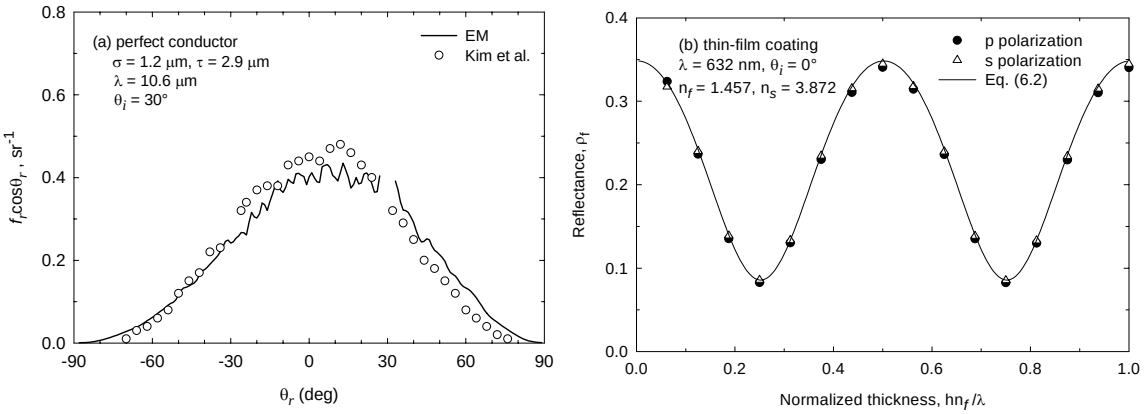

Figure 6.2 Validation of the EM-wave solution for (a) a perfect conductor and (b) a thin-film coating.

In the numerical implementation for both ray-tracing methods, the angular resolution $\Delta\theta_r$ is set to 1°. To ensure a relative standard deviation of 5% for any averaged BRDF value greater than 0.01, the MSM uses ten million rays ($N = 10^7$). Meanwhile, in the SGM, the length of the truncated surface ranges from 200λ to 250λ, depending on the rms surface roughness. The surface is divided into 2,048 surface nodes. Among these nodes, only the central part of the surface (around 1,000 nodes) is illuminated to minimize the edge effect. Two hundred surfaces are needed to achieve the same relative standard deviation as the MSM. In the EM-wave solution, usually the length of the surface is 40λ, and this surface is divided into 800 nodes. The relative standard deviation is 10% from the simulation results of 200 surfaces. The simulation uses a computer with a 3.2 GHz Pentium 4 processor and 2 GB memory. For a perfectly conducting surface, it takes the computer about one minute for the MSM, six minutes for the SGM, and 30 minutes for the EM-wave solution. However, for a dielectric surface with a thin film, it takes one minute for the MSM, four minutes for the SGM, and nine hours for the EM-wave solution. Because a complicated iterative algorithm is used in the SGM to treat the shadowing and the masking, the SGM requires more computation time. Since a matrix equation needs to be solved, the EM-wave solution takes much longer time than the hybrid methods. In the SGM, the energy of each reflected ray is the same for a perfectly conducting surface while it is reduced on each reflection for a dielectric surface or a thin-film coated surface. Therefore, the simulation for a thin-film coated surface converges faster than that for a perfectly conduction surface. In the EM-wave approach, the size of the matrix is $N \times N$ for a perfectly conducting surface while it is $4N \times 4N$ for a thin-film coated surface. Consequently, the EM-wave solution takes much longer time for the latter.

Two criteria are defined for the comparison of results from different methods:

$$\eta_h = \frac{\int_{-\pi/2}^{\pi/2} \left| f_{r,\mathrm{EM}} - f_{r,\mathrm{HB}} \right| \cos\theta_r d\theta_r}{\int_{-\pi/2}^{\pi/2} f_{r,\mathrm{EM}} \cos\theta_r d\theta_r} \tag{6.14a}$$

and

$$\eta_s = \frac{\left| \int_{\theta_i-\theta_{\mathrm{hc}}}^{\theta_i+\theta_{\mathrm{hc}}} \left(f_{r,\mathrm{EM}} - f_{r,\mathrm{HB}} \right) \cos\theta_r d\theta_r \right|}{\int_{\theta_i-\theta_{\mathrm{hc}}}^{\theta_i+\theta_{\mathrm{hc}}} f_{r,\mathrm{EM}} \cos\theta_r d\theta_r} \tag{6.14b}$$

where the subscripts *h* and *s* represent "hemispherical" and "specular", respectively, and θ_{hc} is the half-cone angle. Subscripts EM and HB in f_r stand for the result from the rigorous EM-wave approach and that from the hybrid methods (either SG or MS), respectively. In the definition of η_h, the numerator is the summation of the absolute value of the difference over the angular region from $-\pi/2$ to $\pi/2$. The difference between simulation results on each reflection angle is emphasized. Hence, η_h is not equal to the relative difference of the directional hemispherical reflectance. On the other hand, η_s is the relative difference of the total scattered radiation in an angular region around the specular direction. Therefore, it can be considered as a criterion based on the difference in the directional-conical reflectance. In this thesis, the critical value of η is 20% for both η_h and η_s, and a half-cone angle of $\theta_{\mathrm{hc}} = 5°$ is used in the specular criterion.

6.4 Scattering on Perfectly Conducting Surfaces

The scattering on a perfectly conducting surface without coating is investigated to examine the difference between the SGM and the MSM. The wavelength has little effect on the modeling using the geometric optics approximation (GOA) as long as the

refractive index is invariant. The ratio of σ/τ, related to the average inclination angle of microfacets, is an important parameter in the modeling. The simulation results for two surfaces having the same value of σ/τ will be the same in the MSM because the generation of the microfacets is only dependent on the ratio of σ/τ. In the SGM, the influence of different roughness parameters with the same ratio of σ/τ is insignificant. Usually the difference is smaller than the relative standard deviation of the simulation results.

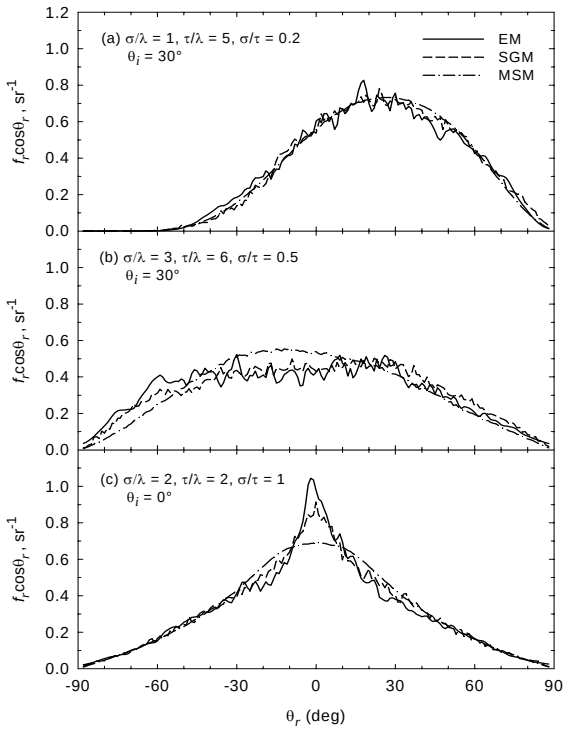

Figure 6.3 Comparison of simulation results for scattering on a perfectly surface: (a) $\sigma = \lambda$, $\tau = 5\lambda$; (b) $\sigma = 3\lambda$, $\tau = 6\lambda$; (c) $\sigma = 2\lambda$, $\tau = 2\lambda$.

Figure 6.3 shows the comparisons of the simulation results from different methods (Zhu et al., 2004). The results from the SGM display a good agreement with

those from the EM-wave solution. As shown in Figure 6.3c, the SGM can predict the retro-reflection peak for a surface with the ratio of σ/τ equal to one although the predicted value from the SGM is 10% lower than the EM-wave solution. Both the numerical simulation (Maradudin et al., 1990) and the experimental measurement (O'Donnell and Mendez, 1987) found that multiple scattering with the coherent interference contributes to the enhanced retro-reflection peak. Figure 6.3 confirms that the ray-tracing approach by the SGM can be an appropriate alternative to the EM-wave solution. A validity region of the SGM has been proposed by Tang et al. (1997) for perfectly conducting surfaces, and the validity region for dielectric surfaces may be broader. The validity of the MSM will be discussed in details.

The surface shown in Figure 6.3a has a value of $\sigma/\tau = 0.2$, corresponding to an average inclination angle of 16°. The microfacets on this rough surface are not so steep that both the shadowing and the masking are insignificant. Therefore, the result from the MSM agrees well with that from the SGM and the EM-wave solution. However, Figure 6.3b shows that the result from the MSM deviates obviously from that from the EM-wave solution for a surface with σ/τ equal to 0.5, corresponding to an average inclination angle of 35°. It can be imagined that the microfacets on this surface are much steeper than those on the surface in Figure 6.3a. Hence, both the shadowing and the masking will have significant influence because the microfacets are steeper and the incidence angle is oblique. For the MSM, η_h is 19 %, indicating that the MSM cannot accurately deal with the shadowing and the masking effect.

In Figure 6.3c, the incidence is intentionally set to the normal direction in order to remove the shadowing effect. The MSM can result in a reasonable agreement with the

EM-wave solution, except that the value from the MSM is much lower in the angular spanning from −10° to 10°. When σ/τ is equal to 1, the average inclination angle is 55°. Therefore, the microfacets on this surface are very steep. Both the SGM and MSM can separate the first order and the second order contributions from the total scattering. The second-order contribution refers to those rays reflected by two microfacets before they leave the rough surface. The second-order contribution is lower in the MSM than in the SGM although the first-order contributions are very close. For the MSM, η_s is 26 %, larger than the critical value. It can be concluded that the MSM cannot be used for a surface with a large value of σ/τ because of its limited ability to model the multiple scattering, which is a consequence of the masking effect. One reason for the limitation may come from the shadowing function since the correlation between height and slope is ignored in the Smith shadowing function (Smith, 1967). Another reason may be attributed to the algorithm of the MSM. The generation of the second microfacet, which may intercept the reflected bundle by the first microfacet, is independent of the orientation of the first microfacet. This may affect the prediction of the second order or higher order scattering.

A large number of roughness parameters have been investigated in the present work. From the comparison of the results from the MSM and the EM-wave solution, it can be concluded that the MSM can result in a reasonable agreement with the EM-wave solution when σ/τ is less than one if the incidence is at the normal direction. However, the validity regime will be smaller when the incidence comes to the surface at the oblique angle.

6.5 Simulation on Thin-film Coated Surfaces

In Figure 6.4-Figure 6.6 (Zhu et al., 2004), the thin-film coated surface is a layer of silicon dioxide on a rough silicon substrate, and the incidence wavelength λ is 632 nm. This kind of surface can be approximated by the three-layer system in Figure 6.1 since silicon is opaque at room temperature when the incidence wavelength is less than 1.1 μm. In addition, the thin film is non-absorbing at λ = 632 nm. The BRDF is the averaged value from *p*-and *s*-polarizations. Figure 6.4 shows the effect of film thickness on the comparison of simulation results from the EM-wave solution and the hybrid methods. As shown in Figure 6.4a, the two hybrid methods basically give the same results because the value of σ/τ is 0.1. Furthermore, the results from the EM-wave approach and the hybrid methods agree well when the film thickness is up to one wavelength. Both η_h and η_s are less than 8% for the SGM. However, large deviation can be observed when $h = 2\lambda$. For this case, η_h is 22% and η_s is 19% for the SGM. Both are close to the critical value of 20%. The reason for the large deviation will be explained later. It can be observed from Figure 6.4a that the profile of the BRDF changes as the film thickness increases. The peak in the BRDF is nearly in the specular direction when $h = 0.1\lambda$. When $h = 0.2\lambda$ and $h = \lambda$, these peaks are shifted by a few degrees toward smaller reflection angles. For these three cases, the BRDF curve still has a Gaussian shape. However, the BRDF curve for the case of $h = 2\lambda$ is far away from the Gaussian shape. The maximum BRDF value occurs at $\theta_r = 46°$ instead of $\theta_r = 30°$; furthermore, a shoulder shows up around $\theta_r = 15°$. The change of the shape of the BRDF curve is attributed to the variation of the reflectivity with respect to the local film thickness and local incidence angle.

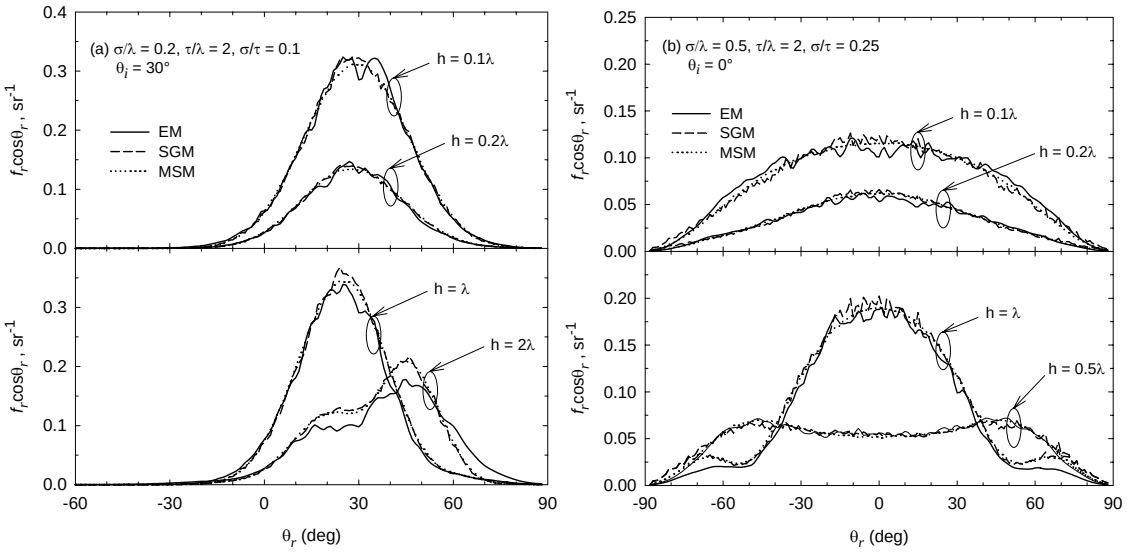

Figure 6.4 Effects of film thickness on the validity of the hybrid method: (a) $\sigma = 0.2\lambda$, $\tau = 2\lambda$; (b) $\sigma = 0.5\lambda$, $\tau = 2\lambda$.

In Figure 6.4b, the rms roughness is increased to half of the wavelength while the autocorrelation length is the same as that in Figure 6.4a. Since the value of σ/τ is equal to 0.25, there is no obvious deviation between the results from the hybrid methods. The agreement between the results from the EM-wave solution and the hybrid methods is good, except that a small deviation can be observed at $60° < |\theta_r| < 80°$ in the BRDF curve with $h = \lambda$. The shapes of the BRDF curves are very different as the film thickness increases. The BRDF curves for $h = 0.1\lambda$ and $h = 0.2\lambda$ look similar. The highest BRDF value occurs around the specular direction (normal direction), and then the BRDF value gradually goes down as the reflection angle departs from the specular direction. However, two satellite peaks can be observed around $|\theta_r| = 50°$ in the BRDF curve for $h = 0.5\lambda$. The BRDF at the satellite peak is higher than that at the specular direction. For this surface, the major contribution to the BRDF is from the first-order scattering. Therefore, the

occurrence of the satellite peaks should be explained by the variation of the reflectivity with the local incidence angle. At the specular direction, the local film thickness is half of the wavelength in vacuum, not half of the wavelength in the film; therefore, the reflectivity of the coated microfacet is not the maximum. As the local film thickness and the refraction angle change with the local incidence angle, the reflectivity of the microfacet at some angular positions can be higher than that at the specular reflection. Therefore, satellite peaks can appear in the BRDF curve. In addition, a Gaussian-shaped peak around the specular direction and two small satellite peaks can be seen in the BRDF curve with $h = \lambda$. According to the hybrid methods the side peaks are located at $|\theta_r| = 70°$. However, this feature is not obvious in the BRDF curve from the EM-wave solution, although two shoulders can be observed at $|\theta_r| = 65°$. Based on the comparisons presented in Figure 6.4, it can be concluded that the hybrid method is valid when $h \leq \lambda$ for the studied surfaces.

As mentioned earlier, the hemispherical criterion is 22% for the coated surface shown in Figure 6.4a with $h = 2\lambda$. Similarly, the hemispherical criterion is 25% for a coated surface with $\sigma = 0.5\lambda$, $\tau = 2\lambda$ and $h = 2\lambda$. Therefore, it can be inferred that the hybrid methods are invalid when the film thickness is larger then the incidence wavelength. The failure of the hybrid methods may be attributed to the corner effect. In the ray-tracing algorithm using the GOA, the reflection on each microfacet is independent. In other words, the reflection on one microfacet has no influence on the reflection on nearby microfacets. It is a reasonable approximation for uncoated rough surface. However, for thin-film coated rough surfaces, the reflection on one microfacet can interact with the reflection on nearby microfacets. Therefore, scattering on the coated

rough surface cannot be simply treated as a summation of reflections from individual microfacets; the coated surface has to be considered as one object if the corner effect is significant. It can be imaged that the corner effect will be more significant if the film thickness is larger and the average inclination angle of the microfacets is larger, i.e., the ratio of σ/τ is larger. Consequently, care must be taken when the hybrid methods are used for surfaces with a large value of σ/τ and a large film thickness.

To investigate how the validity region of the GOA for a perfectly conducting surface changes when a coated rough surface is studied, two surfaces whose roughness parameters are close to the boundary of the validity region proposed by Tang et al. (1997) are chosen to be the substrate surface. Figure 6.5 presents the comparison of the simulation results for these two surfaces with a film thickness of 0.1λ. The roughness parameters in Figure 6.5a are $\sigma = \lambda$ and $\tau = \lambda$. As shown in the upper plot in Figure 6.5a, the simulation results for the normal incidence are in reasonable agreement. However, some deviations are noticeable between the results from the hybrid methods. Although the SGM can nearly resolve the specular peak, the value predicted from the MSM is slightly lower than that from the EM-wave solution. The hemispherical criteria η_s are 8% for the SGM and 12% for MSM, respectively. Therefore, this surface can be positioned within the validity regime for the hybrid method. However, when the incidence is at 30°, significant deviations can be observed among the results from different methods. The agreement between the EM-wave solution and SGM is reasonable at most angular regions, except for the region around the retro-reflection angle. On the contrary, the MSM fails to predict the BRDF for this surface. The BRDF curve from the MSM at θ_i = 30° look similar to that at θ_i = 0°. The failure of the MSM is attributed to its incapability

to model the shadowing and multiple scattering when $\sigma/\tau = 1$ and $\theta_i = 30°$. In the low plot of Figure 6.5a, the MSM overestimates the BRDF in the region $-20° < \theta_r < 20°$ while it underestimates the BRDF in the region $-80° < \theta_r < -20°$. The hemisphere criteria are 13% for the SGM and 24% for the MSM. As a consequence, this surface is in the validity region for the SGM, but it is out of the validity region for the MSM.

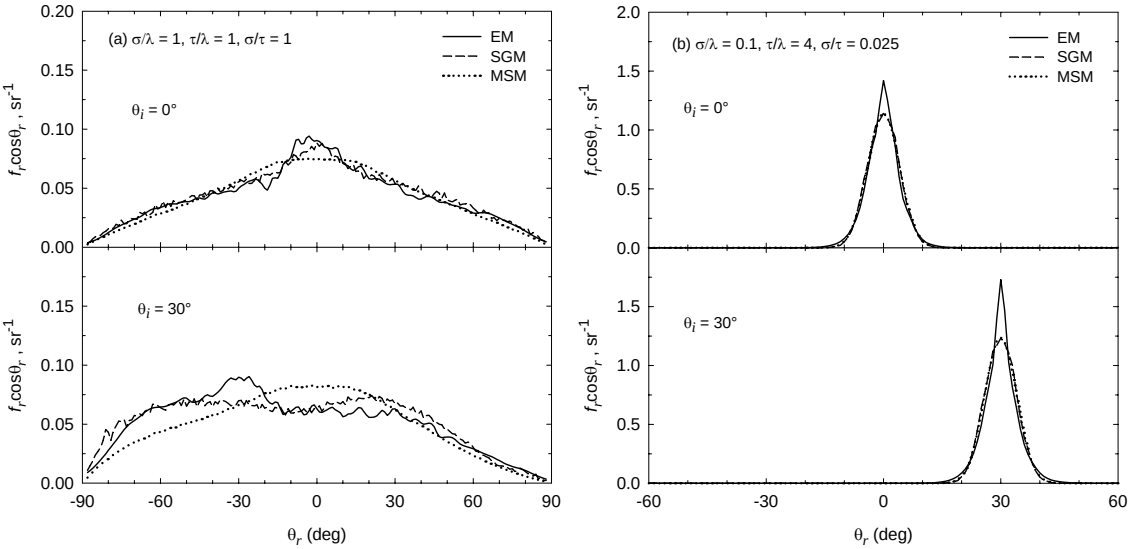

Figure 6.5 Comparisons of simulation results for surfaces with $h = 0.1\lambda$:
(a) $\sigma = \lambda$, $\tau = \lambda$; (b) $\sigma = 0.1\lambda$, $\tau = 4\lambda$.

Figure 6.5b displays the comparison for a surface with $\sigma = 0.1\lambda$ and $\tau = 4\lambda$. Although τ is a few times larger than λ, σ is much smaller than λ. Therefore, it is difficult to ascertain whether or not the hybrid method is valid. The MSM and the SGM basically give the same results due to the small value of σ/τ. When the incidence is at the normal direction, the results from the EM-wave solution and the hybrid method do not show large deviation. However, the peak value from the hybrid method is lower than that from the EM-wave solution. The hemispherical criterion is 8% for the SGM; therefore,

this surface is in the valid region of the hybrid method. According to Tang et al. (1997), the GOA would be invalid for a perfectly conducting surface with the same roughness. The disagreement may be explained by that the validity region can be different for dielectric surfaces and thin-film coated surfaces since their reflectivity is lower than unity. On the other hand, when the incidence is at 30°, the peak value from the hybrid method is much lower than that from the EM-wave solution as shown in the low plot in Figure 6.5b. The hemispherical criterion increases to 19%, close to the critical value. The reason for the large difference is that the surface may appear smoother to the oblique incidence since $\sigma\cos\theta_i$ becomes smaller; therefore, the diffraction effect may become important.

Since there are too many variables, such as rms roughness and autocorrelation length, refractive indices of substrates and coatings, film thickness, and so on, constructing a complete regime map for scattering on coated rough surfaces is not feasible. In this thesis, a regime map for the validity of the hybrid method has been constructed for a layer of silicon dioxide coating on a silicon substrate in the visible wavelength with a fixed film thickness. The hemispherical criterion with a critical value of 20% is used to construct the validity regime. A wide range of roughness parameters has been examined. The autocorrelation lengths are λ, 2λ, and 4λ, respectively. The rms roughnesses are 0.1λ, 0.2λ, 0.5λ, and λ, respectively. These roughness parameters are chosen since they are reasonable for real surfaces in the microelectronics industry. For each combination of the autocorrelation length and the rms roughness, both the normal incidence ($\theta_i = 0°$) and the oblique incidence ($\theta_i = 30°$) have been tested.

Figure 6.6a illustrates the validity region for rough surfaces with a coating thickness of 0.1λ. Generally speaking, the validity region of the MSM is similar to that of

the SGM. Both methods are valid when $2\lambda \le \tau \le 4\lambda$ and $0.2\lambda \le \sigma \le \lambda$. One exception is at $\sigma = \lambda$, $\tau = \lambda$, and $\theta_i = 30°$, which was explained in Figure 6.5a. It can be seen that the hybrid method fails for a rough surface with $\sigma = 0.1\lambda$ and $\tau = \lambda$ or 2λ; however, it becomes valid for a surface with $\sigma = 0.2\lambda$ and the same value of τ. This infers that in the hybrid method the rms roughness σ cannot be too small, compared to the incidence wavelength. In addition, if the rms roughness σ is fixed at 0.1λ while the autocorrelation length τ increases from 2λ to 4λ, the hybrid method becomes valid. It might be expected that the hybrid method remains invalid because σ is much smaller than λ. Nevertheless, the results indicate that a large value of the autocorrelation length may be essential to the validity of the GOA, and hence, to the validity of the hybrid method.

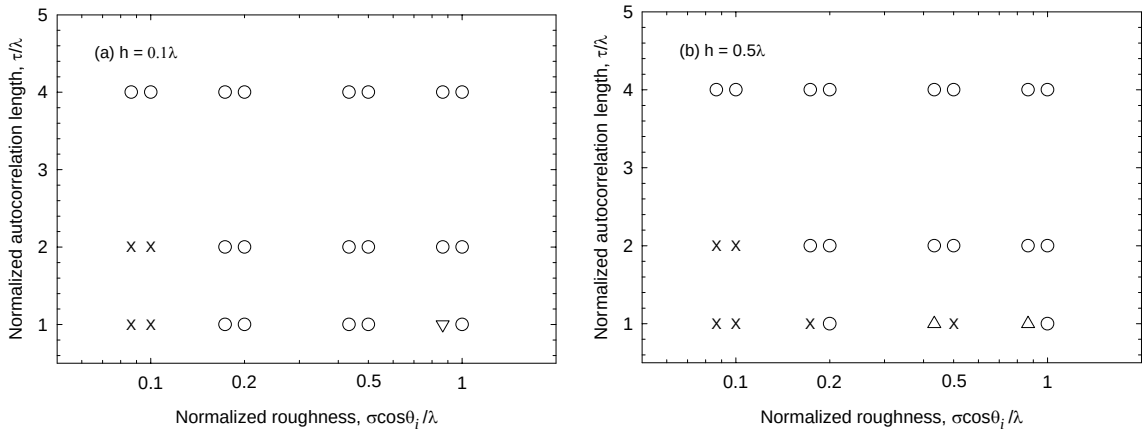

Figure 6.6 Validity region of the hybrid method: (a) $h = 0.1\lambda$; (b) $h = 0.5\lambda$.
o: SGM and MSM valid; x: SGM and MSM invalid; Δ: SGM invalid; ∇: MSM invalid.

The validity of the hybrid method for rough surfaces with a coating thickness of 0.5λ is shown in Figure 6.6b. Similar to the comparison shown in Figure 6.6a, both methods are valid when $2\lambda \le \tau \le 4\lambda$ and $0.2\lambda \le \sigma \le \lambda$. However, the agreement between

the hybrid methods and the EM-wave solution becomes worse when $\tau = \lambda$. The poor agreement is caused by the deviation around the satellite peak at the normal incidence and around the off-specular peak at the oblique incidence. No general conclusion can be made on which hybrid method is better. In some cases, the MSM can result in better agreement with the EM-wave solution than the SGM. For example, For a surface with $\sigma = 0.5\lambda$, $\tau = \lambda$, and $\theta_i = 30°$, η_h is 29% for the SGM and 14% for the MSM. As expected, the validity region of the hybrid method become smaller since the corner effect is more significant when the film thickness increases. The corner effect strongly affects the validity for surfaces with $\tau = \lambda$ because the average inclination angle is large and the mean lateral dimension of asperities is small. Nevertheless, the influence is not strong enough to obviously change the validity region when $\tau = 2\lambda$ or 4λ.

Figure 6.6 demonstrates the hybrid method is valid for rough surfaces with $0.2\lambda \leq \sigma \leq \lambda$ and $2\lambda \leq \tau \leq 4\lambda$ when $h < 0.5\lambda$. Generally speaking, the GOA can be applicable for a rough surface with a large rms roughness and a long autocorrelation length, compared to the incidence wavelength. Therefore, the hybrid method may be valid for this kind of surface if the corner effect is not significant. Since a large number of surface nodes are needed in the simulation, the EM-wave solution for this kind of surface is not performed. From the comparisons presented in Figure 6.4, the hybrid method may still work for a surface with a large value of τ. Other constraints include that the ratio of σ/τ is small and the film thickness is less than one wavelength.

CHAPTER 7

CONCLUSIONS AND RECOMMENDATIONS

A comprehensive investigation has been carried out on the surface statistics and the BRDF of the rough side of several silicon wafers. The surface statistics are determined from the topographic data obtained with an AFM. The scatterometer used in the BRDF measurement has been fully characterized and further improved. The correlation between the surface roughness statistics and the BRDF has been established. The major findings of this thesis are as follows.

- Prominent differences have been shown in the 2-D slope distribution functions for the studied samples. Strong anisotropic features with angular-correlated side peaks have been observed for some samples while nearly isotropic features have been observed for the others. The striking features in the slope distribution of the anisotropic samples are possibly related to the formation of {311} planes during the chemical etching. It has been demonstrated that the 2-D slope distribution can successfully represent the orientation of the microfacets on a random rough surface. Therefore, close collaboration with semiconductor wafer manufacturers is suggested so that the proposed method for the determination of the 2-D slope distribution may be used in industry to monitor the evolution of the surface morphology.

- Both the 1-D slope distribution and the cross-sections of the 2-D slope distribution have been incorporated into the unified geometric optics model to predict the in-plane BRDF. Although partial agreement exists between the predicted BRDFs using the 1-D slope distribution for one of the anisotropic samples, the predicted BRDFs using

the cross-sections of the 2-D slope distribution agree with the measured values at most observation angles for all the studied samples. Therefore, it is suggested that the 2-D slope distribution should be used in the prediction of the BRDF.

- The subsidiary peaks in the BRDFs for the anisotropic samples can be quantitatively correlated to the side peaks in the 2-D slope distribution. Furthermore, the variation of the BRDF with the azimuthal angle for the anisotropic samples can be explained well by the variation of the cross-sections of the 2-D slope distribution. The discrepancy in the specular direction may be attributed to the limitation of the geometric optics approximation. The deviations at large positive observation angles for *s*-polarization may be attributed to multiple scattering and the breakdown of the shadowing function at large reflection angles for the anisotropic samples. Future studies are needed to include the interference and multiple scattering in the BRDF modeling. In addition, the agreement between the cross-sections of the 2-D slope distribution obtained from the measured BRDFs through a reverse procedure and those obtained from the topographic data suggests that the angle-resolved light scattering can also be used to characterize the orientation of the microfacets on the rough surface.

- The comparison of the simulation results from the EM-wave solution and the hybrid method has been made for a silicon dioxide layer on a rough silicon substrate in the visible wavelength region. The film thickness can significantly influence the validity of the hybrid method. It has been established that the hybrid method can be applied in a wide roughness range. The validity regime is $0.2\lambda \le \sigma \le \lambda$ and $2\lambda \le \tau \le 4\lambda$ when $h = 0.1\lambda$ or $h = 0.5\lambda$. The proposed validity regime will benefit future research

related to simulations for thin-film coated rough surfaces. Further studies are needed to develop a complete regime map and to assess its generality.

REFERENCES

American Society for Testing and Materials (ASTM), *Standard Practice for Angle Resolved Optical Scatter Measurements on Specular or Diffuse Surfaces*, Publication E1392-96, 1997.

Anderson, S., Pompea, S.M., Shepard, D.F., and Castonguay, R.. "Performance of a Fully Automated Scatterometer for BRDF and BTDF Measurements at Visible and Infrared Wavelengths," SPIE Proc., Vol. 967, pp. 159-170, 1988.

Barnes, P.Y., Early, E.A., and Parr, A.C., *Spectral Reflectance*, NIST Special Publication 250-48, U.S. Government Printing Office, Washington, DC, 1998.

Bawolek, E. J., Mohr, J. B., Hirleman, E. D., and Majumda, A., "Light Scattering from Polysilicon and Aluminum Surfaces and Comparison with Surface-Roughness Statistics by Atomic Force Microscopy," Appl. Opt., Vol. 32, pp. 3377-3400, 1993.

Beckmann, P., and Spizzichino, A., *The Scattering of Electromagnetic Waves from Rough Surfaces*, Artech House, Norwood, MA, 1987.

Bennett., J.M., and Mattsson, L., *Introduction to Surface Roughness and Scattering*, 2nd ed., Optical Society of American, Washington, D.C., 1999.

Bhushan, L.S., Chen, W., Abedrabbo, S., and Ravindra, N.M., "Modeling Emissivity of Rough and Textured Silicon Wafers," J. Electro. Mate., pp. 1341-1346, 1998.

Binnig, G., Quate, C.F., and Gerber, Ch., "Atomic Force Microscope," Phys. Rev. Lett., Vol. 56, pp. 930-933, 1996.

Brewster, M.Q., *Thermal Radiative Transfer and Properties*, John Wiley & Sons, New York, 1992.

Bruce, N.C., and Dainty, J.C., "Multiple Scattering from Random Rough Surfaces using the Kirchhoff approximation," J. Mod. Opt., Vol. 38, pp. 579-590, 1991.

Bruno, W.M., Roth, J.A., Burke, P.E., Hewitt, W.B., Holmbeck, R.E., and Neal, D.G., "Prediction of the Bidirectional Reflectance-Distribution Function from Atomic-Force and Scanning-Tunneling Microscope Measurements of Interfacial Roughness," Appl. Opt., Vol. 34, pp. 1229-1238, 1995.

Cao, L.X., Vorburger, T.V., Lieberman, A.G., and Lettieri, T.R., "Light-Scattering Measurement of the RMS Slopes of Rough Surfaces," Appl. Opt., Vol. 30, pp. 3221-3226, 1991.

Caron, J., Lafait, J., and Andraud, C., "Catastrophe Theory Interpretation of Multiple Peaks Produced by Light Scattering from Very Rough Dielectric Surfaces," Physica B, Vol. 325, pp. 76-85, 2003.

Chen, M.F., and Fung, A.K., "A Numerical Study of the Regions of Validity of the Kirchhoff and Small-Pertubation Rough Surface Scattering Models," Radio Sci., Vol. 23, pp. 163-170, 1988.

Chen, Y.B., Zhu, Q.Z., Wright, T.L., King, W.P., and Zhang, Z.M., "Bidirectional Reflection Measurements of Periodically Microstructured Silicon Surfaces," Int. J. Thermophys., Vol. 25, pp. 1235-1252, 2004.

Demont, P., Huetz-Aubert, M., and N'Guyen, H.T. "Experimental and Theoretical Studies of the Influence of Surface Conditions on Radiative Properties of Opaque Materials," Int. J. Thermophys., Vol. 3, pp. 335-364, 1982.

DeWitt, D.P., Sorrell, F.Y., and Elliott, J.K., "Temperature Measurement Issues in Rapid Thermal Processing," Symposium on Rapid Thermal and Integrated Processing VI, San Francisco, March 31-April 4, 1997.

Drolen, B.L., "Bidirectional Reflectance and Specularity of Twelve Control Materials," J. Thermo. Heat Transfer, Vol. 6, pp. 672-679, 1992.

Dumas, PH., Bouffakhreddine, B., Amra, C., Vatel, O., Andre, E., Galindo, R., and Salvan, F., "Quantitative Microroughness Analysis Down to the Nanometer Scale," Europhys. Lett., Vol. 22, pp. 717-722, 1993.

Edwards, D.F., "Silicon(Si)," *Handbook of Optical Constants of Solids* (Edited by Palik, E.D.), Academic Press, Orlando, FL, pp. 547-569, 1985.

Elson, J.M., "Infrared Light Scattering from Surfaces Covered with Multiple Dielectric Overlayers", Appl. Opt., Vol. 16, pp. 2872-2881, 1977.

Fan, Y.-H, and Qiu, T., "Transiet Heat Transfer in Batch Thermal Reactors for Silicon Wafer Processing," Int. J. Heat Mass Transfer, Vol. 41, pp. 1549-1557, 1998.

Feng, X., Schott, J.R., and Gallagher, T., "Comparison of Methods for Generation of Absolute Reflectance-Factor Values for Bidirectional Reflectance-Distribution Function Studies," Appl. Opt., Vol. 32, pp. 1234-1242, 1993.

Filinski, I., "The Effects of Sample Imperfections on Optical Spectra," Phys. Status Solidi B, Vol. 49, pp. 577-588, 1972.

Flury, B, *A First Course in Multivariate Statistics*, Springer, New York, 1997.

Ford, J.N., Tang, K., and Buckius, R.O., "Fourier Transform Infrared System Measurement of the Bidirectional Reflectivity of Diffuse and Grooved Surfaces," J. Heat Transfer, Vol. 117, pp. 955-962, 1995.

Germer, T.A. and Asmail, C.C., "Goniometric Optical Scatter Instrument for Out-of-plane Ellipsometry Measurements," Rev. Sci. Instrum., Vol. 70, pp. 3688-3695, 1999.

Gu, Z.-H, Lu, J.Q., and Maradudin, A.A., "Enhanced Backscattering from a Rough Dielectric Film on a Glass Substrate," J. Opt. Soc. Am. A, Vol. 10, pp. 1753-1764, 1993.

Guérin, C.-A., "Scattering on Rough Surfaces with Alpha-stable Non-Gaussian Height Distributions," Waves Random Media, Vol. 12, pp. 293-306, 2002.

He, X.D., Torrance, K.E., Sillion, F.X., and Greenberg, D.P., "A Comprehensive Physical Model for Light Reflection," Comput. Graph., Vol. 25, pp. 175-186, 1991.

Hegeman, J.B.J.W., Kooi, B.J., Groen, H.B., and de Hosson, J.Th.M., "Analyses of Small Facets Imaged with Scanning-Probe Microscopy," J. Appl. Phys., Vol. 86, pp. 3661-3669, 1999.

Icart, I., and Arques, D., "Simulation of the Optical Behavior of Rough Identical Multilayer," SPIE Proc., Vol. 4100, pp. 84-95, 2000.

Inoue, T., Yamamoto, Y., Satoh, M., Ide, A., and Katsumata, S., "Surface Structure of Single-crystal CeO_2 Layers Grown on Si," Thin Solid Films, Vol. 281-282, pp. 24-27, 1996.

Jahanmir J., and Wyant J.C., "Comparison of Surface Roughness Measured With an Optical Profiler and a Scanning Probe Microscope," SPIE Proc., Vol. 1720, pp. 111-118, 1992.

Johnson, J.T., Tsang, L., Shin, R.T., Pak, K., Chan, C.H., Ishimaru, A., and Kuga, Y., "Backscattering Enhancement of Electromagnetic Waves from Two-dimensional Perfectly Conducting Random Rough Surfaces: a Comparison of Monte Carlo Simulations with Experimental Data," IEEE Trans. Antennas Propag., Vol. 44, pp. 748-756, 1996.

Kim, M.-J., Dainty, J.C., Friberg, A.T., and Sant, A.J., "Experimental Study of Enhanced Backscattering from One- and Two-Dimensional Random Rough Surfaces," J. Opt. Soc. Am. A, Vol. 7, pp. 569-577, 1990.

Kong, J.A., *Electromagnetic Wave Theory*, 2nd ed., Wiley, New York, 1990.

Kreyszig, E., *Advanced Engineering Mathematics*, 7th Ed., John Wiley & Sons, New York, 1993.

Lee, H.J., Lee, B.J., and Zhang, Z.M., "Modeling the Radiative Properties of Semitransparent Wafers with Rough Surfaces and Thin-Film Coatings," 4th Int. Symposium on Radiative Transfer, Istanbul, Turkey, No. RAD-IV-50, June 20-25, 2004.

Lettieri, T.R., Marx, E., Song, J.-F., and Vorburge, T.V., "Light Scattering from Glossy Coatings on Paper," Appl. Opt., Vol. 30, pp. 4439-4447, 1991.

Lu, J.Q., Sánchez-Gil, J.A., Méndez, E.R., Gu, Z.-H., and Maradudin, A.A., "Scattering of Light from a Rough Dielectric Film on a Reflecting Substrate: Diffuse Fringes," J. Opt. Soc. Am. A, Vol. 15, pp. 185-195, 1998.

Maradudin, A.A., Michel, T., McGurn, A.R., and Méndez, E.R., "Enhanced Backscattering of Light from a Random Grating," Anna. Phys., Vol. 203, pp. 255-307, 1990.

Marx, E., Malik, I.J., Strausser, Y.E., Bristow, T., Poduje, N., and Stover, J., "Round Robin Determination of Power Spectral Densities of Different Si Wafer Surfaces," SPIE Proc., Vol. 3275, pp. 26-36, 1998.

McKnight, M.E., Vorburge, T.V., Mara, E., Nadal, M.E., Barnes, P.Y., and Galler, M., "Measurement and Prediction of Light Scattering by Clear Coatings," Appl. Opt., Vol. 40, pp. 2159-2168, 2001.

Mitsas, C.L., and Siapkas, D.I., "Generalized Matrix Method for Analysis of Coherent and Incoherent Reflectance and Transmittance of Multilayer Structures with Rough Surfaces, Interfaces, and Finite Substrate," Appl. Opt., Vol. 34, pp. 1678-1683, 1995.

Modest, M.F., *Radiative Heat Transfer*, McGraw-Hill, New York, 1993.

Muller, T., Kumpe, R., Gerber, H.A., Schmolke, R., Passek, F., and Wagner, P., "Techniques for Analyzing Nano-topography on Polished Silicon Wafers," Microelectron. Eng., Vol. 56, pp.123-127, 2001.

Nee, S.-M. F., Dewees, R.V., Nee, T.-W., Johnson, L.F., and Moran, M.B., "Slope Distribution of a Rough Surface Measured by Transmission Scattering and Polarization," Appl. Opt., Vol. 39, pp. 1561-1569, 2000.

Nicodemus, F. E., "Reflectance Nomenclature and Directional Reflectance and Emissivity," Appl. Opt. Vol. 9, pp. 1474-1475, 1970.

O'Donnell, K.A., and Mendez, E.R., "Experimental study of scattering from characterized random surfaces," J. Opt. Soc. Am. A, Vol. 4, pp. 1194-1205, 1987.

Pak, K., Tsang, L., Chan, C.H., and Johnson, J., "Backscattering Enhancement of Electromagnetic Waves from Two-dimensional Perfectly Conducting Random Rough Surfaces based on Monte Carlo Simulations," J. Opt. Soc. Am. A, Vol. 12, pp. 2491-2499, 1995.

Phong, B.T., "Illumination for Computer Generated Images," Commun. ACM, Vol. 18, pp. 311-317, 1975.

Priest, R.G., and Germer, T.A., "Polarimetric BRDF in the Microfacet Model: Theory and Measurements," Proceedings of the 2000 Meeting of the Military Sensing Symposia Specialty Group on Passive Sensors, Vol. 1, pp. 169-181, 2000.

Proctor, J.E. and Barnes, P.Y., "NIST High Accuracy Reference Reflectometer-Spectrophotometer," J. Res. Natl. Inst. Stand. Technol., Vol. 101, pp. 619-627, 1996.

Prokhorov, A.V., and Hanssen, L.M., "Algorithmic Model of Microfacet BRDF for Monte Carlo Calculation of Optical Radiation Transfer," SPIE Proc., Vol. 5192, pp. 141-157, 2003.

Resnik, D., Vrtacnik, D., and Amon, S., "Morphological Study of {311} Crystal Planes Anisotropically Etched in (100) Silicon: Role of Etchants and Etching Parameters," J. Micromech. Microeng., Vol. 10, pp. 430-439, 2000.

Roy. S, Bang, S.Y., Modest, M.F., and Stubican, V.S., "Measurement of Spectral, Directional Reflectivities of Solids at High Temperatures between 9 and 11 μm," Appl. Opt., Vol. 32, pp. 3550-3558, 1993.

Saillard, M., and Sentenac, A., "Rigorous Solutions for Electromagnetic Scattering from Rough Surfaces," Waves Random Media, Vol. 11, pp. R103-R137, 2001.

Sánchez-Gil, J.A., and Nieto-Vesperinas M., "Light Scattering from Random Rough Dielectric surfaces," J. Opt. Soc. Am. A, Vol. 8, pp. 1270-1283, 1991.

Schleef, D., Schaefer, D.M., Andres, R.P., and Reifenberger, R., "Radial-Histogram Transform of Scanning-Probe-Microscope Images," Phys. Rev. B, Vol. 55, pp. 2535-2542, 1997.

Siegel, R., and Howell, J., *Thermal Radiation Heat Transfer*, 4th ed., Taylor & Francis, New York, 2002.

Shen, Y.J., *Investigation of Bidirectional Reflectance and Transmittance of Rough Silicon Wafers*, Ph.D. Thesis, University of Florida, 2002.

Shen, Y.J., Zhang, Z.M., Tsai, B.K., and DeWitt, D.P., "Bidirectional Reflectance Distribution Function of Rough Silicon Wafers," Int. J. Thermophys., Vol. 22, pp. 1311-1326, 2001.

Shen, Y.J., Zhu, Q.Z., and Zhang, Z.M., "A Scatterometer for Measuring the Bidirectional Reflectance and Transmittance of Semiconductor Wafers with Rough Surfaces," Rev. Sci. Instrum., Vol. 74, pp. 4885-4892, 2003.

Smith, B., "Geometrical Shadowing of a Random Rough Surface," IEEE Trans. Antennas Propag., Vol. 15, pp. 668-671, 1967.

Sorrell, F.Y., and Gyurcsik, R.S., "Model-Based Emissiivty Correction in Pyrometer Temperature Control of Rapid Thermal Processing Systems," IEEE Trans. Semi. Manu., Vol. 6, pp. 273-276, 1993.

Stover, J., *Optical Scattering: Measurement and Analysis*, SPIE Press, Bellingham, WA, 1995.

Stover, J.C., Ivakhnenko, V.I., and Scheer, C.A., "Comparison of Surface PSD's Calculated from both AFM Profiles and Scatter Data," SPIE Proc., Vol. 3275, pp. 37-46, 1998.

Tang, K., and Buckius, R.O., "The Geometric Optics Approximation for Reflection from Two-dimensional Random Rough Surfaces," Int. J. Heat Mass Transfer, Vol. 41, pp. 2037-2047, 1998.

Tang, K., and Buckius, R.O., "A Statistical Model of Wave Scattering from Random Rough Surfaces," Int. J. Heat Mass Transfer, Vol. 44, pp. 4059-4073, 2001.

Tang, K., Dimenna, R.A., and Buckius, R.O., "Regions of Validity of the Geometric Optics Approximation for Angular Scattering from Very Rough Surfaces," *Int. J. Heat Mass Transfer*, Vol. 40, pp. 49-59, 1997.

Tang, K., Kawka, P.A., and Buckius, R.O., "Geometric Optics Applied to Rough Surfaces Coated with an Absorbing Thin Film," J. Thermophys. Heat Transfer, Vol. 13, pp. 169-176, 1999a.

Tang, K., Yang, Y., and Buckius, R.O., "Theory and Experiments on Scattering from Rough Interfaces," *Annual Review of Heat Transfer* (Edited by Tien, C.L.), Vol. 10, pp. 100-140, Begell House, New York, 1999b.

Taylor, B.N. and Kuyatt, C.E., *Guidelines for Evaluation and Expressing the Uncertainty of NIST Measurement Results*, NIST Technical Note No. 1297, 1994.

Taylor, J.R., *An Introduction to Error Analysis*, 2nd ed., University Science Books, Sausalito, CA, 1997.

Thomas, T.R., *Rough Surface*, 2nd ed., Imperial College Press, London, 1999.

Thorsos, E, "The Validity of the Kirchhoff Approximation for Rough Surface Scattering Using a Gaussian Roughness Spectrum," J. Acoust. Soc. Am., Vol. 83, pp. 78-92, 1988.

Timans, P.J., Sharangpani, R., and Thakur, R.P.S., "Rapid Thermal Processing," *Handbook of Semiconductor Manufacturing Technology* (Edited by Nishi, Y.), pp. 201-286, Marcel Dekker, New York, 2000.

Torrance, K., and Sparrow, E., "Theory for Off-specular Reflection from Roughed Surfaces," J. Opt. Soc. Am., Vol. 57, pp. 1105-1114, 1967.

Tsang, L., and Kong, J.A., "Energy Conservation for Reflectivity and Transmissivity at a Very Rough Surface," J. Appl. Phys., Vol. 51, pp. 673-380, 1980.

Tsang, L., Kong, J.A. Ding, K.-H., and Ao, O.A., *Scattering of Electromagnetic Waves: Numerical Simulations*, Joh Wiley & Sons, New York, 2001.

Tsunoda, K., Ohashi, E., and Adachi, S., "Spectroscopic Characterization of Naturally and Chemically Oxidized Silicon Surfaces," J. Appl. Phys., Vol. 94, pp. 5613-5616, 2003.

Vandenabeele, P., and Maex, K., "Influence of Temperature and Backside Roughness on the Emissivity of Si Wafers During Rapid Thermal Processing," J. Appl. Phys., Vol. 72, pp. 5867-5875, 1992.

Vatel, O., Dumas, P., Chollet, F., Salvan, F., Andre, E., "Roughness Assessment of Polysilicon Using Power Spectral Density," Jap. J. Appl. Phys., Vol. 32, pp. 5671-5674, 1993.

Vorburger, T.V., Marx, E., and Lettieri, T.R., "Regimes of Surface Roughness Measurable with Light Scattering," Appl. Opt., Vol. 32, 3401-3408, 1993.

Ward, G.J., "Measuring and Modeling Anisotropic Reflection," Computer Graphics, Vol. 26, pp. 265-272, 1992.

Warnick, K., and Chew, W.C., "Numerical Simulation Methods for Rough Surface Scattering," Waves Random Media, Vol. 11, pp. R1-R30, 2001.

Wiesendanger, R., *Scanning Probe Microscopy and Spectroscopy: Methods and Applications*, Cambridge University Press, Cambridge, UK, 1994.

White, D.R., Saunders, P., Bonsey, S. J., van de Ven, J., and Edgar, H., "Reflectometer for Measuring the Bidirectional Reflectance of Rough Surfaces," Appl. Opt., Vol. 37, pp. 3450-3454, 1998.

Whitehouse, D.J., "Surface Metrology," Meas. Sci. Technol., Vol. 8, pp. 955-972, 1997.

Wyant, J.C., Koliopoulos, C.L., Bhushan, B., and Basila, D., "Development of a Three-Dimensional Noncontact Digital Optical Profiler," J. Tribol., Vol. 108, pp. 1-8, 1986.

Wolf, E., "A Generalized Extinction Theorem and its role in Scattering Theory," *Coherence and Quantum Optics* (Edited by Mandel, L., and Wolf, E.), pp. 339-357, Plenum, New York, 1973.

Xu, H., and Sturm, J.C., "Emissivity of Rough Silicon Surface: Measurement and Calculation," Mat. Res. Soc. Symp. Proc., Vol. 387, pp. 29-34, 1995.

Yeh, P., *Optical Waves in Layered Media*, Wiley, New York, 1988.

Zaworski, J.R., Welty, J.R., and Drost, M.K., "Measurement and Use of Bi-directional Reflectance," Int. J. Heat Mass Transfer, Vol. 39, pp. 1149-1156, 1996a.

Zaworski, J.R., Welty, J.R., Palmer, B.J., and Drost, J.R., "Comparison of Experiment with Monte Carlo Simulations on a Reflective gap using a Detailed surface Properties Model," J. Heat Transfer, Vol. 118, pp. 388-393, 1996b.

Zhang, Z.M., "Surface Temperature Measurement Using Optical Techniques," *Annual Review of Heat Transfer* (Edited by Tien, C.L.), Vol. 11, pp. 351-411, 2000.

Zhang, Z.M., Fu, C.J., and Zhu, Q.Z., "Optical and Thermal Radiative Properties of Semiconductors Related to Micro/Nanotechnology," *Advances in Heat Transfer* (Edited by Hartnett, J.P., Cho. Y.I., Greene, G.A.), Vol. 37, pp. 179-296, Academic Press, New York, 2003.

Zhao, Y.-P., Wu, Y.-J., Yang, H.-N., Wang, G.-C., and Lu, T.-M., "In situ Real-Time Study of Chemical Etching Process of Si (100) Using Light Scattering," Appl. Phys. Lett., Vol. 69, pp. 221-223, 1996.

Zhou, Y.H., Shen, Y.J., Zhang, Z.M., Tsai, B.K., and DeWitt D.P., "A Monte Carlo Model for Predicting the Effective Emissivity of the Silicon Wafer in Rapid Thermal Processing Furnaces," Int. J. Heat Mass Transfer, Vol. 45, pp. 1945-1949, 2002.

Zhou, Y.H., and Zhang, Z.M., "Radiative Properties of Semitransparent Silicon Wafers with Rough Surfaces," J. Heat Transfer, Vol. 125, pp. 462-470, 2003.

Zhu, Q.Z., Sin, S., and Zhang, Z.M., 2002, "Surface Characterization of the Rough Side of Silicon Wafers," 21st Southeastern Conference on Theoretical and Applied Mechanics, Orlando, Florida, May, 2002.

Zhu, Q.Z., and Zhang, Z.M., "Anisotropic Slope Distribution and Bidirectional reflectance of a Rough Silicon Surface," Accepted for publication by J. Heat Transfer, 2004a.

Zhu, Q.Z., and Zhang, Z.M., "Characterization of the Microfacet Orientation and Angle-Resolved Scattering of Several Rough Silicon Surfaces," Submitted to Appl. Opt., 2004b.

Zhu, Q.Z, Lee, H.J., and Zhang Z.M., "The Validity of Using Thin-Film Optics in Modeling the Bidirectional Reflectance of Coated Rough Surfaces," 37th AIAA Thermophysics Conference, Portland, Oregon, June 28-July 1, 2004.

Zipin, R.B., "A Preliminary Investigation of the Bidirectional Spectral Reflectance of V-grooved Surfaces," Appl. Opt., Vol. 5, pp. 1954-1957, 1966.

VITA

Qunzhi Zhu was born and grew up in Xianju, Zhejiang, China. He attended Shanghai Jiao Tong University and received both Bachelor and Master degrees in Thermal Energy Engineering. After his graduation, he worked as a mechanical engineering and a software engineering for two years. In the year of 2000, he continued his graduate study in the Department of Mechanical Engineering at the University of Florida. He came to Georgia Institute of Technology as a Ph.D. candidate in Mechanical Engineering in August, 2002. His research focuses on the characterization of surface roughness and the modeling and measurements of the bidirectional reflectance of rough surfaces. He has contributed to several journal papers and one book chapter. His hobbies include badminton, music, and traveling.

Upon completion of his graduate studies, he wishes to purse a career in temperature measurement and heat transfer analysis in thermal engineering and application of the light scattering method and the atomic force microscopy in surface characterization in microelectronics industry.